FINAL REPORT

Morphology and Mechanism of Benign Inhibitors

SERDP Project WP-1619

JULY 2012

Dale W. Schaefer
University of Cincinnati

SERDP
DOD ▪ EPA ▪ DOE

REPORT DOCUMENTATION PAGE	Form Approved OMB No. 0704-0188

PLEASE DO NOT RETURN YOUR FORM TO THE ABOVE ORGANIZATION.

1. REPORT DATE *(DD-MM-YYYY)*	2. REPORT TYPE	3. DATES COVERED *(From - To)*
04-07-2012	Final	Mar 2008 -Mar 2012

4. TITLE AND SUBTITLE
Morphology and Mechanism of Benign Inhibitors

5a. CONTRACT NUMBER
W912HQ-11-P-0053

5b. GRANT NUMBER

5c. PROGRAM ELEMENT NUMBER

6. AUTHOR(S)
Schaefer, Dale W.
Hu, Naiping
Dong, Xuecheng
Wang, Peng

5d. PROJECT NUMBER
WP-1619

5e. TASK NUMBER

5f. WORK UNIT NUMBER

7. PERFORMING ORGANIZATION NAME(S) AND ADDRESS(ES)
University of Cincinnati
College of Engineering and Applied Science
Cincinnati, OH 45221-0012

8. PERFORMING ORGANIZATION REPORT NUMBER

9. SPONSORING/MONITORING AGENCY NAME(S) AND ADDRESS(ES)
Strategic Environmental Research and Development Program
4800 Mark Center Drive, Suite 17D08
Alexandria, VA 22350-3600

10. SPONSOR/MONITOR'S ACRONYM(S)
SERDP

11. SPONSOR/MONITOR'S REPORT NUMBER(S)

12. DISTRIBUTION/AVAILABILITY STATEMENT
Approved for public release; distribution is unlimited

13. SUPPLEMENTARY NOTES

14. ABSTRACT
This project demonstrates that most interfacial issues important to corrosion control can be elucidated by neutron and x-ray reflectivity. The evolution of a surface in a corrosive environment can now be measured in near real time. The data produced give corrosion scientists their first glimpse at active corrosion processes in water under potential control. The methodology was applied to Al protected by Trivalent Chromium Process (TCP) conversion coatings, vanadate conversion coatings and anodized aluminum. In all three cases, water penetrates the protective films. Corrosion protection is due to a thin interfacial layer as water penetrates all films studied. Failure on passive metals can be accelerated by application of an anodic potential. Failure of TCP-coated Al occurs by bulk water penetration of the film at the pitting potential. The compromised film remains on the metal creating an isolated environment conducive to pitting. A new anodic hardening method was developed by exposing TCP-coated Al to increasingly anodic potentials in the presence of a cerium chloride solution.

15. SUBJECT TERMS
Trivalent Chromium Process (TCP), Aluminum (Al), Cerium (Ce), Anodizing, Neutron reflectivity, X-ray reflectivity, Corrosion, Sealing, Small-angle scattering.

16. SECURITY CLASSIFICATION OF:			17. LIMITATION OF ABSTRACT	18. NUMBER OF PAGES	19a. NAME OF RESPONSIBLE PERSON
a. REPORT	b. ABSTRACT	c. THIS PAGE			Debi Galloway
U	U	U	U	115	19b. TELEPHONE NUMBER *(Include area code)* 513 556 5054

Reset

Standard Form 298 (Rev. 8/98)
Prescribed by ANSI Std. Z39.18

Table of Contents

List of Tables

List of Figures

List of Acronyms

AA: Aluminum alloy;

AAO: Anodic aluminum oxide;

AMCC: Advanced Materials Characterization Center, University of Cincinnati;

BET: Brunauer-Emmett-Teller gas adsorption method;

D_2O: Deuterated water;

DAB: Debye-Anderson-Brumber structure factor for porous materials;

DCP: Direct current polarization;

DOE: Department of Energy;

EA: Electro-assisted;

EIS: Electrochemical impedance spectroscopy;

ICP: Inductively coupled plasma;

LANL: Los Alamos National Laboratory;

LANSCE: Los Alamos Neutron Science Center;

NAVAIR: U. S. Naval Air Systems Command

NR: Neutron reflectivity;

OCP: Open circuit potential;

ORNL: Oak Ridge National Laboratory;

PVD: Physical vapor deposition;

RT: Room temperature;

SANS: Small-angle neutron scattering;

SAXS: Small-angle x-ray scattering;

SCE: Saturated calomel electrode;

SEM: scanning electron microscopy;

SHE: Standard hydrogen electrode

SLD: Scattering length density;

SNS: Spallation Neutron Source at ORNL;

SPEAR: The Surface Profile Analysis Reflectometer at LANL;

TCP: Trivalent Chromium Process;

ToF-SIMS; Time of flight secondary ion mass spectroscopy

USAXS: Ultra small-angle x-ray scattering;

VCC: Vanadium conversion coating;

XRR: X-ray reflectivity.

List of Keywords

Electro-assisted deposition;

Trivalent Chromium Process (TCP);

Aluminum (Al);

Aluminum alloys (AA 2024-T3, AA 1100);

Cerium (Ce);

Anodic hardening;

Aluminum anodizing;

Neutron Reflectivity;

X-ray Reflectivity;

Corrosion;

Sealing;

Small-angle scattering.

Acknowledgements

This research was funded by a contract from the Strategic Environmental Research and Development Program.

We thank Michael Jablin, Jarek Majewski, Jan Ilavsky, Rex Hjelm and James Browning for assistance in collecting and interpreting the data. The reflectivity data were collected at the SPEAR reflectometer at the Lujan Neutron Scattering Center at Los Alamos National Laboratory (LANL) and the Liquids Reflectometer at the Spallation Neutron Source (SNS), Oak Ridge National Laboratory (ORNL). Small-angle neutron scattering data were measured on the Low-Q Diffractometer at the Lujan Neutron Scattering Center at LANL. Small-angle x-ray scattering data were measured at beam lines 15 ID-D and 32 ID-B at the Advanced Photon Source, Argonne National Laboratory.

Lujan Neutron Scattering Center is supported by LANL under DOE contract W7405-ENG-36, and by Office of Basic Energy Sciences, U. S. Department of Energy. Research performed at SNS at ORNL was sponsored by the Scientific User Facilities Division, Office of Basic Energy Sciences, U. S. Department of Energy. Use of the Advanced Photon Source was supported by the U. S. Department of Energy, Office of Science, Office of Basic Energy Sciences, under Contract No. DE-AC02-06CH11357.

1. Abstract

Objective: The objective for this project was to demonstrate the utility of neutron reflectivity and x-ray reflectivity to elucidate the morphology and protection mechanisms of environmentally benign inhibitors for Al alloys.

The project was in response to SERDP Statement of Need WPSON 08-02 *Scientific Understanding of Non-Chromated Corrosion Inhibitors Function.* This project was submitted because the technique of neutron reflectivity had never been used to address corrosion or inhibition of aluminum. In fact the morphology evolution of a conversion coating in a corrosive environment had never been measured by any technique. Success was defined as measurement of the structure and evolution of an inhibitor film and/or inhibited surface in a corrosive environment by neutron reflectivity.

Approach: Twenty-seven specific tasks were successfully completed organized around the following six elements.

1. Identify the film optimal metal and coating deposition parameters for reflectivity.
2. Investigate vanadate, trivalent chromium, and cerium inhibition with reflectivity.
3. Correlate measured morphology with electrochemical observations.
4. Monitor the *in situ* evolution of passive films with and without soluble inhibitors.
5. Identify the mechanisms of inhibition and failure.
6. Elucidate formation and sealing of anodic films on aluminum.

Every aspect of the approach had to be perfected from deposition of suitable metal films to building of a combined reflectivity and electrochemical cell to observe the evolution of a passive film *in situ* in a corrosive environment with and without the addition of a soluble inhibitor.

Results: In addition to successful demonstration of required technology, every task produced new observations that could not be made by conventional corrosion methodology.

We successfully deposited smooth Al, Cu and mixed Cu/Al films on Si wafers and demonstrated that the alloy structure can be manipulated by subsequent annealing. This accomplishment opens up new possibilities to determine the impact of alloying elements on corrosion performance.

We observed the formation and stripping of the native oxide film on Al. We showed that the native oxide is thin, porous and partially hydrated. The oxide is easily stripped under anodic conditions, which facilities subsequent deposition of conversion coatings.

By measuring the evolution of bare Al under anodic conditions we demonstrated that Al dissolution measured by the corrosion current agrees with that measured by reflectivity. This correspondence means that side reactions do not compromise electrochemical analysis of corrosion processes.

We developed a new conversion-coating deposition protocol based on a simplified, cathodically deposited Trivalent Chromium Process (TCP) that eliminates the ferricyanide and fluoride compounds in commercial formulations.

We demonstrated that thin, smooth, uniform TCP films suitable for reflectivity measurements can be deposited on aluminum-covered Si wafers. Using a combination of neutron and x-ray methods we determined the composition of the resulting conversion coatings to be $Cr_2O_3 \cdot 2.1H_2O \cdot 0.85$ ($ZrO_2 \cdot 1.6H_2O$).

We demonstrated the failure mechanism of TCP films in a pitting scenario in the absence of a soluble inhibitor such as Ce(III). Below the pitting potential, water exchanges with the film crystal hydrate water but bulk solution does not penetrate the film. At the pitting potential, the protective film swells and bulk water penetrates. The compromised film remains on the metal, creating an isolated environment conducive to pitting.

Using a new step-by-step polarization test, we showed that addition of a soluble Ce(III) inhibitor leads to anodic healing of an otherwise compromised TCP film. By raising the potential over several hours, the pitting potential can be substantially increased, a process we call anodic hardening.

Using neutron reflectivity and chemical analysis we showed that during anodic hardening, Ce(III) penetrates the TCP film.

We achieved 3000-Å, smooth, uniform aluminum layers on Si suitable for anodizing experiments. We observed the kinetics of anodic oxide growth on these films using reflectivity.

We discovered a new anodizing protocol based on current control with a voltage limit that affords precise control over the oxide layer thickness.

We used small-angle x-ray scattering on anodized Al foils to measure the in-plane structure of the porous anodic aluminum oxide. The hexagonal pattern of pores develops within 20s. The pore size, and interpore distance do not changes after 20 s; the pore depth, however, increases linearly with time until the pores fully penetrate the foil.

Using small-angle x-ray scattering and small angle neutron scattering, we observed a slight alteration of the anodic aluminum oxide structure after cold nickel acetate sealing of anodic aluminum oxide. Hot nickel acetate sealing, however, fills in the pores and covers the air surface of the anodic aluminum oxide.

Neutron reflectivity further reveals the mechanism of cold nickel acetate sealing. At room temperature nickel acetate deposits at the bottom of the pores. Long-term exposure to the sealing bath leads to penetration of the pore wall and subsequent degradation of the surface on drying. We conclude that cold nickel acetate sealing cannot replace the hot sealing methods.

Benefits: The ability to measure evolving surfaces *in situ* means that the "structure" element of process-structure-performance research strategy is accessible for the first time. When an electrical potential is applied the method is essentially a powerful accelerated failure test. The data not only reveal failure, but the mechanism of failure.

The new anodizing protocol developed offers improved control over growth and thickness of the anodic aluminum oxide film. The anodizing strategy should be applicable to troublesome metals such as magnesium and iron. Using this approach, it should be possible to reduce the energy consumption required for anodizing.

The anodization study opens new possibilities for improved sealing. Using neutron reflectivity (NR), one can determine the deposit profile and correlate the profile with performance. The

observation of sealant penetration of the pore walls opens intriguing possibilities for dramatically improved corrosion performance of aluminum and other metals.

2. Objective

The objective for this project was to demonstrate the utility of neutron reflectivity (NR) and x-ray reflectivity (XRR) to elucidate the morphology and protection mechanisms of environmentally benign inhibitors for Al alloys. The specific goals were:

- Identify the passive film deposition parameters that are optimal for NR and XRR measurement;
- Investigate vanadate, trivalent chromium process (TCP), cerium and anodized aluminum systems with both electrochemical and neutron/x-ray reflectivity methods;
- Correlate measured morphology with electrochemical observations;
- Monitor the *in situ* evolution of TCP films under electrochemical potential control, with and without additional inhibitors;
- Identify the mechanism of Ce(III) inhibition on TCP films using *in situ* neutron reflectivity;
- Investigate the formation and sealing of anodized films on aluminum.

3. Background

Although protective films of some type must exist on corrosion-inhibited metals, film morphology and speciation has eluded characterization except in a few cases. The problem is that conventional techniques are not able to resolve both the chemical and physical characteristics of submicron films. Current understanding of corrosion performance, therefore, is largely based on indirect electrochemical methods. Morphological studies based on electron imaging and electron spectroscopies do exist, but these methods do not yield quantitative data that can be compared to models. Also, because of the limited penetration depth of electrons, there is little information on chemical speciation normal to the surface, even though such speciation is central to models of passivation.

The method of specular reflection of x-rays and neutrons from surfaces has existed for almost sixty years. These methods have been extensively used for solving soft matter problems like polymer mixing, but have not been applied to elucidate inhibitor mechanisms. The most important advantage of neutron and x-ray reflectivity is the ability to track the chemical and physical changes of passive films non-destructively, including under water and/or organic coatings.

Our work builds on that of two groups that have used neutron reflectivity to investigate oxide films on metals. Shoesmith et al. examined native and anodic oxides on Zr[1, 2] and Ti.[3, 4] Ti is particularly interesting since there is large contrast between the metal and the oxide, which makes it easy to sort out the structure of very thin native oxide films. Weisler et al. studied anodic oxides on Ta and Nb.[5]

In both x-ray and neutron reflectivity, a beam of photons is directed at a surface at an incident angle of less than 1°. Reflectivity, $R(q)$, defined as the intensity ratio between reflected and incident beams, is measured as a function of the normal component of the scattering vector, $q = (4\pi/\lambda)\sin\theta$, where θ is the angle-of-incidence on the wafer and λ is the wavelength. All measurements reported here were done in the specular mode, where the angle of incidence is equal to the angle of reflectance.

For a uniform film, the reflectivity curve, ($R - q$ curve), oscillates as a function of q. The so-called Kiessig fringes are caused by the interference of waves reflected from both interfaces of the film. When q is significantly far from the critical edge (the q at which the beam first penetrates the film), the layer thickness, d, can be estimated from the Δq spacing between the minima of two neighboring fringes, by $d = 2\pi/\Delta q$.

By fitting the $R - q$ curve it is possible to determine the chemical composition and density profile within the film. The inversion to obtain the real-space film composition profile is simple for a single layer of constant composition such as if often postulated for inhibitor films. As it turns out, however, few of the films we studied fall into this class. Nevertheless, we were able to work out the composition profiles in several systems prepared from H_2O and D_2O precursors, which we studied by both x-ray and neutron reflectivity. The remainder of the report describes in detail how we accomplished this analysis.

When the raw reflectivity data are inverted, the result is not a composition profile directly, but a scattering-length-density (SLD) profile. In the case of x-rays, the SLD is just the electron density, which is determined by the chemical composition and mass density. In the case of neutrons, the

neutron SLD is also simply related to composition and density, but the relationship cannot be described as the "neutron density." Therefore we use the more generic designation, scattering length density, to describe both neutron and x-ray data.

To harvest rich information from reflectivity data, it is necessary to achieve smooth films less than 3000-Å thick. The key unknown at the beginning of the project was whether we could actually make such films. In addition, we had to achieve smooth Al substrates. As will be shown, we achieved excellent vanadate, trivalent chromium process (TCP) and anodic aluminum oxide (AAO) films. We also tried Ce but Ce did not form a conversion-coating layer. We did use Ce as a soluble inhibitor.

Having established the ability of NR and XRR to probe passive films, we then designed a reflectivity cell suitable for measuring the evolution of both anodic and cathode surfaces under potential control in an active corrosion environment. New information regarding TCP degradation, passivity and inhibition was obtained. We also discovered an anodic-hardening process using soluble Ce(III) that leads to improved corrosion resistance of Al alloys.

Motivated by discussions with Craig Matzdorf of Naval Air Systems Command (NAVAIR), we also initiated the study of anodizing of aluminum. According to the literature anodic aluminum oxide (AAO) has a two-layer structure, a nonporous barrier oxide and a porous surface oxide. The thin barrier layer (10-100 nm) is found at the bottom of the pores at the metal interface. The two-layer morphology was confirmed using reflectivity techniques. However, we found that both layers are porous. To prepare films suitable for x-ray and neutron reflectivity (thin and smooth), we developed a simultaneous current-limited and voltage-controlled anodizing protocol to control the growth of the porous alumina film on Al-coated Si wafers.

Small-angle x-ray scattering (SAXS) experiments compliment the reflectivity data on AAO films. Although SAXS has been used by many researchers to study the morphology of porous materials we had to develop new analysis tools to complete this study. We used four approaches to data analysis (depending on known variables) to retrieve the surface area, pore volume, pore size, strut size and strut skeletal density. The methodology was validated on porous membranes and mesoporous cellular foams by comparison with manufacturer's ratings on pore size and Brunauer-Emmet-Teller (BET) measurement of the surface area. Argonne National Laboratory has incorporated our code in its SAXS data analysis package, which is freely available to the public.

Finally we investigated sealing of anodized aluminum. Sealing is necessary to improve corrosion resistance. Sealing strategies, based on various combinations of temperature and chemical composition of the bath, all improve corrosion resistance to some extent. The structural alteration induced by sealing and the impact of structure on corrosion resistance, however, had not been investigated previously.

4. Materials and Methods

Information regarding materials used is provided in this section. The experimental design and data analysis methods are also discussed in detail.

4.1 Silicon wafer cleaning

Both NR and XRR require smooth substrates, accounting for the choice of metal-coated Si wafer substrates. One-side-polished single crystal (111) wafers (2 or 3 inch diameter, and 5 mm thickness) were obtained from Wafer World, Inc. (West Palm Beach, FL. USA).

A standard Piranha cleaning process[6] followed by ethanol rinsing was applied on each wafer (both newly purchased and recycled). The Piranha etching solution contains H_2SO_4 (98%) from Pharmco-Aaper, Inc. (Brookfield, CT. USA) and H_2O_2 (30%) from Fisher Scientific, (Fair Lawn, NJ. USA). The two components were mixed in volume ratio of 3 : 1. Each wafer was etched at 90°C - 100°C for 3 to 5 minutes and rinsed with 200 proof absolute ethanol from Pharmco-Aaper, Inc. (Brookfield, CT. USA). Wafers were rinsed until ethanol did not bead up on the silica surface. Then the wafers were dried in N_2 and stored in sealed container prior the e-beam evaporation of the metal coating. Note that Piranha solution is highly corrosive and must be used with proper precaution and personal protective equipment.

4.2 e-beam evaporation

Electron beam evaporation is a physical vapor deposition (PVD) method. In a typical e-beam system, the deposition chamber is evacuated to a pressure less than 5×10^{-6} Torr. The material to be evaporated is in the form of an ingot. An electron beam generated by field emission is accelerated to a high kinetic energy and focused on the ingot. The kinetic energy of the electrons is converted into thermal energy as the beam bombards the surface. The surface temperature of the ingot increases resulting in the formation of a melt. The liquid ingot evaporates under vacuum. Some of incident electron energy is lost in the excitation of x-rays and secondary emission. The vapor of ingot material deposits on the wafer and forms a smooth thin coating. The thickness of film is controlled by deposition time. The e-beam depositions were performed at Advanced Materials Characterization Center at the University of Cincinnati. The instrument is Temescal FC1800 e-Beam Evaporator from AircoTemescal, USA.

4.3 Metal-wafer systems

4.3.1 Aluminum alloy (AA 2024) coated silicon wafers

AA2024 thin films were physically deposited on silicon wafers as metal substrate by e-beam evaporation. The aluminum alloy (AA) AA2024-T3 ingot was purchased from McMaster-Carr Supply Company (Aurora, OH. USA). The composition of AA2024 is 3.8 to 4.9 Cu, 1.2 to 1.8 Mg, 0.3 to 0.9 Mn, 0.5 Si and Fe, 0.15 Zn and Ti, and 0.1 Cr on a wt% basis.

4.3.2 Al-coated silicon wafers.

Later studies were done on pure Al-coated silicon wafers instead of the AA 2024. Alloy-coated wafer substrates have following disadvantages: 1) since the alloy coating is a uniform solid solution rendered by e-beam deposition, intermetallic structures present in AA2024-T3 do not exist on the alloy-coated wafer; 2) alloy annealing could not be applied, because heating disrupted surface smoothness. As a result, intermetallic inclusions, which are believed to be important in annealed alloys, could not be realized on alloy-coated wafers.

To mimic the microscopic galvanic couples that exist in the annealed alloy we developed a split metal-wafer couple that employs an Al-coated wafer coupled to a noble-metal-coated wafer. Specifically we used a pure Al coating to represent Al matrix anode in AA 2024-T3. The noble-metal wafer played the role of Cu-rich inclusions in the alloy.

4.3.3 Noble metal coated silicon substrates.

The metal-wafer couple for the liquid split cell requires a wafer-based cathode (counter electrode). We selected Cu and Au. The choice of Cu originated from AA2024 alloy composition, which is known to have Cu-rich inclusions. However the lifetime and degradation rate of Cu layer were not compatible with the requirements of the split liquid cell. We eventually settled on a Au layer with a Cr buffer layer added to enhance adhesion to the wafer substrate.

4.3.4 Optimization of the metal layer

To achieve the high quality inhibitor films and to simplify the reflectivity data analysis, the thickness and smoothness of the metal substrate had to be optimized. A thick metal film (> 4000 Å) simplifies the data analysis due to the elimination of interference signals from metal substrate. However, the roughness of metal layer also increases with thickness. A rough metal layer results in a rough inhibitor film, which complicates downstream data analysis. A thin metal film (< 250 Å) on the other hand can ensure smoothness but introduces the interference signals from metal layer itself and also complicates downstream data analysis.

A series of experiments was also completed to determine the optimum deposition conditions of the inhibitor films. A long reaction time with the inhibitor solution leads to thick but rough films. A shorter reaction time results in a smoother film. However, a thin film is possibly not representative of a functional inhibitor film.

Based on the above considerations, a series of samples was made by varying metal thickness and/or precursor treatment time. Optimized parameters were determined by measuring these samples by XRR.

4.4 Metal coupons

We also used AA2024-T3 coupons (from ACT, Hillsdale, MI. USA, T3 refers to the heat treatment protocol) to validate the discoveries on TCP-coated wafer samples used for NR. For the anodizing study AA1100 coupons (from ACT, Hillsdale, MI. USA) were used since the copper content in AA2024 could introduce complications during anodizing. Each coupon was cut into 2 × 2 inch panels, polished and rinsed in ethanol. These metal panels were used for electrochemical performance testing.

4.5 Characterization Methods

4.5.1 Neutron reflectivity (NR) and x-ray reflectivity (XRR)

Neutron (or x-ray) reflectivity has been extensively used to elucidate interfacial structure but is virtually unknown in corrosion science. The most important advantage of neutron reflectivity for the corrosion research is that NR enables a greater range of sample environments (e. g. vacuum and aqueous) and is superior for quantitative analysis. Access to NR facilities however is limited. X-ray reflectivity (XRR), by contrast, is readily available at the University of Cincinnati. We use XRR in concert with NR. For parts of the analysis presented below both methods are required.

In the NR and XRR experiments, a wafer sample is irradiated by the incident beam (neutron or x-ray) at a very small incident angle, θ. The ratio of the fluxes of the reflected beam to the incident beam is measured as a function of scattering vector, q. The relationship between θ and q is:

$$q = \frac{4\pi \sin\theta}{\lambda} \tag{1}$$

where λ is the wavelength of the incident beam. For Cu k_α x-rays, λ is 1.54 Å. For NR, θ is fixed and a broad spectrum of wavelengths impinges on the sample (1.5 Å < λ < 16 Å), in order to obtain a range of q values. The actual λ of any particular detected neutron is calculated by time-of-flight.

The normalized reflected intensity (R) is plotted against q. The R - q curve results from the superposition of waves scattered by the interface. The amplitude and attenuation of each wave are determined by the thickness, roughness and scattering length density (SLD) of each layer. Thickness and roughness represent structural information while the SLD reveals the chemical composition:

$$\mathrm{SLD} = \rho \frac{N_\mathrm{A}}{M} \sum\nolimits_{\mathrm{molecule}} b_\mathrm{i} \tag{2}$$

where ρ is the mass density, N_A is Avogadro number, M is the molecular weight, b_i is the atomic scattering length of atom i, and $\rho \frac{N_\mathrm{A}}{M}$ is molecular number density. $\sum_{\mathrm{molecule}} b_\mathrm{i}$ is the sum over scattering lengths of all atoms present in one molecule. The neutron and x-ray scattering lengths are known for all elements. The x-ray scattering length density is equivalent to electron density, which to first approximation is proportional to the mass density. The neutron scattering length, on the other hand, depends on the interaction with the nuclei of the atoms, which is depends on isotopic composition. This unique character gives neutron SLD substantial contrast on samples with similar mass densities but different composition.

The R -q data, analyzed using Irena Macros[7] 2.35 for Igor Pro 6.10, reveal the SLD profile (SLD as function of perpendicular distance from the substrate). Like all diffraction analyses, the inversion from reciprocal space to real space is not unique. Since more than one SLD profile may fit the data, physical insight and consistency between NR and XRR are required to assure accurate SLD profiles. Since most parameters in the SLD profile are known, such as the SLD of

silicon, the SLD of metal layer and the thickness and roughness of the metal layer, this information eliminates many unrealistic profiles, leaving little freedom in fitting. Furthermore the profiles that we accept evolve reasonably in different conditions ranging from a simple single-layer sample to complex multi-layer films. Further analysis of these SLD profiles reveals film composition, the mechanism of film passivation and inhibition and the impact of corrosion on film morphology.

4.5.2 X-ray diffraction

X-ray diffraction techniques are based on the elastic scattering of x-rays from structures that have long-range order. This technology was used to determine the composition and crystallinity of deposited inhibitor films.

4.5.3 Ultra small angle x-ray scattering and small-angle neutron scattering

Ultra small-angle x-ray scattering (USAXS) and small-angle neutron scattering were used to elucidate the porosity in anodic aluminum oxide. USAXS was performed at the 15 ID-D and 32 ID-B beam lines at the Advanced Photon Source (APS), Argonne National Laboratories (Argonne, Illinois, USA). SANS was performed at the Lujan Neutron Scattering Center, Los Alamos National Laboratory (Los Alamos, NM, USA).

Scattering data are collected as the scattered flux versus the modulus of the momentum transfer wave vector, q, as discussed above. Specifically we measured the differential scattering cross section per unit volume on an absolute scale, which is referred to as the intensity, $I(q)$. In the USAXS measurements, a beam of 1-Å x-rays strikes a sample and radiation is elastically scattered. A detector records the scattered flux while scattering angle θ is varied. The Bonse-Hart USAXS camera covers the q regime from 10^{-4} Å^{-1} to 1.0 Å^{-1}. The data were subject to an air background subtraction followed, in some cases, by desmearing using the APS routines.[7] All USAXS data fitting was done on the slit-smeared data using the appropriate resolution function to smear the calculated model.

Small-angle scattering data are often analyzed to find intensity regions where $I(q)$ follows Guinier scattering or Porod power-law scattering. Guinier first observed that the correlation range for dilute particles was simply the average particle radius of gyration.[8] The Guinier radius, R_G, is extracted from the initial curvature of the scattering profile. Hence, scattering in this low-q regime is called "Guinier scattering." For a porous body characterized by randomly distributed interfaces, the Debye-Anderson-Brumberger (DAB) equation[9] can be expressed in Guinier format as,

$$\frac{I(q)}{V} = \langle \Delta SLD^2 \rangle \varphi_{\mathrm{p}} \left(1 - \varphi_{\mathrm{p}}\right) \frac{4\pi}{3\sqrt{6}} R_{\mathrm{G}}^3 \left(1 - \frac{R_{\mathrm{G}}^3 q^2}{3} + \cdots\right) \tag{3}$$

where (ΔSLD) is the ensemble-averaged fluctuation of the scattering length density (contrast), ϕ_p is the volume fraction of pores (porosity), and R_G is the Guinier radius of the pores. The contrast, $(\Delta SLD)^2$, for a two-phase system is simply the scattering-length density difference of the two phases (phases 1 and 2), and has units of length^{-2}.

$$(\Delta SLD)^2 = (SLD_1 - SLD_2)^2 \quad (4)$$

where $SLD_{\mathrm{i}} = \rho \frac{N_{\mathrm{A}}}{M} \sum_{\mathrm{molecule}} b_{\mathrm{i}}$. SLD_{i} is the scattering length density of phase i, ρ_i is the mass density of phase i, N_A is the Avogadro's number, and b_j is the scattering length of atom j and M_j is its atomic weight. Subscripts p and s refer to "pore" and "strut." At low porosity levels (ϕ_p <<1), the Guinier radius is proportional to the mean pore size (pore chord), whereas it tracks the solid chord at high porosity.[10]

The intensities at large q often follow a power law,

$$I(q) \propto q^{-P} \quad (5)$$

where P is the power-law exponent. P is often interpreted using fractal geometry.[11, 12] Typically $3 \leq P \leq 4$ when q^{-1} is much smaller than R_G. When $P = 4$ (Porod's law[13]) scattering arises from a smooth, sharp interface. In the range $3 \leq P < 4$ interface is fractally rough.[14]

For an ideal two-phase system, Porod's law predicts that $I(q)$ decreases as $\sim q^{-4}$ for large q.

$$I_V(q) = \frac{I(q)}{V} \equiv \frac{B_V}{q^4} \qquad (qR_G \gg 1) \quad (6)$$

$$B_V = 2\pi(\Delta SLD)^2 S_V \quad (7)$$

where S_V is the surface area per unit volume. The subscript $_V$ denotes that the data are on an absolute scale (cross section per unit sample volume), in which case I_V has units of length^{-1}.

4.5.4 Time-of-flight secondary ion mass spectrometry

Time-of-flight secondary ion mass spectrometry (ToF-SIMS) data were obtained using the IonToF SIMS IV at the Advanced Materials Characterization Center, University of Cincinnati. ToF-SIMS reveals elements and simple compounds by plotting the secondary ion count rate vs. ion mass. The count rate is calibrated using standards of known density ($CrK(SO_4)_2 \cdot 12H_2O$ and K_2ZrF_6). The static SIMS analysis was done at energy of 25 keV with a liquid-metal primary Ga ion gun. Since the samples were moderately non-conductive, a tungsten-based electron flood gun was used to compensate for the charging.

4.5.5 Inductively coupled plasma (ICP) atomic emission spectroscopy

The atomic concentration of Ce, Cr, Zr released from TCP-passivated AA2024-T3 samples with and without anodic hardening were tracked for 20 days using inductively coupled plasma atomic emission spectroscopy, which is available at ICPMS service center, University of Cincinnati (http://plasmachem.weebly.com/icpms-service-center.html). A TCP-passivated AA2024-T3 sample and a TCP-passivated AA2024-T3 sample after Ce(III) anodic hardening were immersed in NaCl (1 wt%) water solution for 20 days. Solution samples were taken every 3 ~ 4 days for chemical trace element analysis.

4.5.6 Scanning electron microscopy

The scanning electron microscopy results were obtained using an FEI XL30 ESEM at 15 kV at the University of Cincinnati. Samples were mounted and coated with 2–3 nm of tungsten using a dual ion beam sputter coater (South Bay Technologies, Inc.) to minimize the artifacts caused by sample charging.

4.6 Vanadate inhibition system

4.6.1 Formulation

The vanadate inhibitor coating formulation proposed by H. Guan and R. G. Buchheit was chosen as target formulation due to its simplicity and proven anticorrosion performance.[15] Analogous to the chromium inhibitor system, the precursor solution contains a mixture of $NaVO_3$ (10 mM), potassium ferricyanide ($K_3Fe[CN]_6$, 3 mM), and sodium fluoride (NaF, 2 mM). The bath pH was adjusted to 2.0 using concentrated HNO_3. In order to achieve a film suitable for neutron and x-ray reflectivity, a diluted (10 times) precursor solution was used at room temperature.

4.6.2 Film growth procedure

Before application of the precursor solution, the metal-coated silicon wafers were rinsed repeatedly with acetone and de-ionized (DI) water to ensure a clean surface. After application of the inhibitor precursor solution on the metal surface for 30 s, the wafer is accelerated to 2000 rpm and held for 1 minute to spin off the excess solution. To get rid of the residual soluble components in the film, the samples were rinsed with DI water repeatedly and then dried in air at room temperature for 24 hours before further characterization. The coating procedure was carried out using a Laurell single-wafer spin processor (WS-400A-6NPP-Lite, North Wales, PA, USA).

4.7 The Trivalent Chromium Process (METALAST® TCP-HF) system

4.7.1 Formulation

We used a commercial TCP product to make Cr(III) conversion coating film. The process includes a H_2SO_4 substrate pretreatment for activation. This pretreatment proved to be a critical step, so we studied the pretreatment process in detail. The TCP solution was METALAST® TCP-HF from Chemetell-Oakite (2241 Park Place, Suite C Minden, NV). H_2SO_4 was 95%-98% from Fisher Scientific (Fair Lawn, New Jersey).

4.7.2 Film growth procedure

Al alloy-coated wafers were first activated in 40-vol% H_2SO_4 at room temperature. XRR analysis as a function of activation time revealed an optimum exposure time of 30 s.

After 30-s activation in 40-vol% H_2SO_4 substrates were immediately rinsed but not dried and then immersed in 25% METALAST® TCP-HF. This process did not exceed 5 s, in order to

minimize re-oxidation of fresh surface. The immersion time was 3 min. A TCP coating layer was noticeable after immersion. Samples were rinsed again and air-blown to dry.

4.8 Electro-assisted (EA) and simplified trivalent chromium processes

Because of the proprietary nature of the METALAST® recipe, we developed a simplified TCP solution based on the original NAVAIR patent and our analysis of the composition of the METALAST® coatings. An electro-assisted deposition scheme was also perfected to deposit the simplified coating.

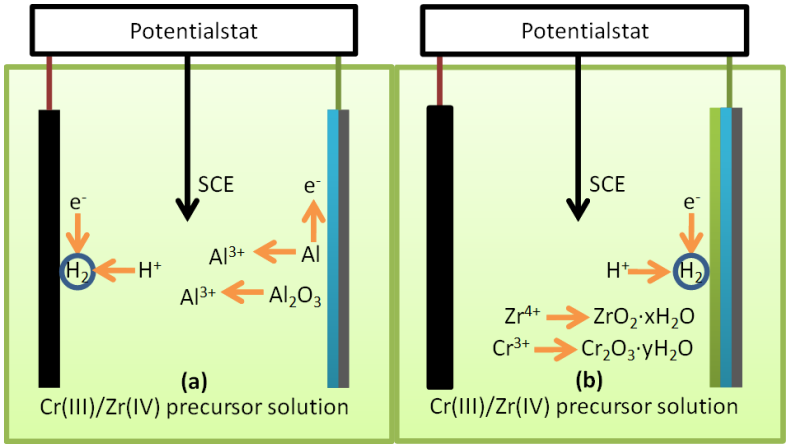

Figure 1. Schematic diagram of the EA-TCP deposition. (a) The substrate is anodically activated in 10-vol% simplified TCP bath. The native oxide and part of the Al alloy layer dissolves while a proton reduction reaction proceeds on the graphite cathode. (b) The alloy substrate is then cathodically polarized. Proton reduction occurs on the alloy surface. The pH rise triggers TCP deposition.

4.8.1 Formulation

The simplified TCP system was chosen based on the film composition reported in our previous work.[3] In electro-assisted deposition the metal surface is the cathode where the TCP coating is formed. Negative ions, including most of the additives in commercial TCP formulations, are repelled from the cathode and excluded from the coatings. Therefore we simplified the formulation to a Cr(III) / Zr(IV) system with an atomic ratio of Cr : Zr = 3 : 5. To make solutions of this ratio, 6 g $KCr(SO_4)_2$ and 8 g K_2ZrF_6 were first dissolved in 1 L of distilled water, then diluted to 10 vol% (pH = 3.5 ± 0.2) and aged for 24 hours before EA deposition.

4.8.2 Film growth procedure

The electro-assisted (EA) deposition method was inspired by the generally accepted mechanism of TCP immersion deposition. Deposition results from a pH increase due to proton reduction at cathodic sites. In order to optimize the current and potential profiles during the EA process, we used a potentiostat (Gamry PCI4 300) to control the potential. The two-step EA deposition process was optimized as a brief anodic polarization (+0.50 V vs. SCE, 30 s) to clean the alloy surface (Figure 1(a)), followed by cathodic deposition (-1.50 V vs. SCE) for 3 minutes (Figure 1(b)).

4.9 Step-by-step anodic hardening for TCP-passivated AA2024-T3 substrates

We demonstrated a straightforward step-by-step approach to improve the pitting resistance of EA-TCP films on AA2024-T3 alloys in the presence of Ce^{3+}. Although this process is not a technology at this point, it does illustrate that there is opportunity for dramatic improvement in corrosion protection compared to what is achievable with native passive films and conversion coatings.

4.9.1 Substrate cleaning

AA2024-T3 alloy panels from ACT Test Panels LLC (273 Industrial Dr, Hillsdale, MI 49242) were cut into 2 × 2 inch specimens. One side of each specimen was sealed by electrical tape. The un-taped side was polished (grit 320, 800, and 1200) and sonicated in ethanol for 15 ~ 30 minutes before EA deposition.

4.9.2 TCP formulation and EA deposition

For EA deposition of TCP films the simplified TCP system (10.5 g $KCr(SO_4)_2$ and 8 g $KZrF_6$) was first dissolved in 1 L distilled water, diluted to 10 vol% (pH = 3.5 ± 0.2) and aged for 24 hours before EA deposition. The EA deposition consists of two steps: slight anodic polarization (+0.50 V, 30 s) to clean the alloy surface, followed by cathodic deposition at one of two different potentials for 180 s. The coated samples were rinsed and dried at room temperature for 24 hours.

4.9.3 Step-by-step anodic hardening by Ce(III)

The electrolyte for step-by-step Ce(III) anodic hardening was a de-aerated aqueous solution with 1 wt% (0.17 M) of NaCl and 0.1 wt% (0.0040 M) of $CeCl_3$. A flat electrochemical cell with an exposed area of 8.03 cm^2 was used to load the 24-hour-dried EA-TCP passivated AA 2024-T3. The sample was stabilized in the test solution for 30 minutes before step-by-step polarization. The polarization process started from the original open circuit potential (OCP) of the EA-TCP coated AA2024-T3 sample. The potential was increased until the anodic current jumped to the mA scale. The potential step was +20 mV until the potential exceeded -650 mV, after which the step was reduced to +10 mV. The step time was initially 30 min and extended to 2 hours as the potential increased. Just below the breakdown potential, where the measured current drastically increases (permanent, stable pits are formed), a normal dynamic DC polarization scan was carried out. The step-by-step polarization test was repeated at pH = 4, 6, and 8.

4.10 *In situ* liquid NR split cell

Based on the step-by-step anodic hardening results and research work done by other groups, Ce(III) has both anodic[16-19] and cathodic inhibition character.[20] Conventional electrochemical methods on Al alloys may be compromised by the intermingled intermetallic structure on alloy surface, resulting in contradictory data depending on electrochemical history. Understanding the evolution of the TCP film under Ce(III) anodic and cathodic inhibition requires two separated wafers to split the anode and cathode surfaces so each can be interrogated by NR.

We utilize a NR split cell to hold two wafer electrodes (a working electrode and a counter electrode) as well as a saturated calomel reference electrode (SCE) for performing electrochemical experiment during NR. Figure 2(a) depicts the design the *in situ* cell for observation of the anode surface under step-by-step Ce(III) inhibition. The TCP-passivated, Al-coated silicon wafer on the top is the working electrode (anode), while the Au-coated wafer at the bottom is a counter electrode. The Ce(III) NaCl-D_2O electrolyte (0.1 g $CeCl_3$ and 1 g NaCl per 100 ml D_2O) in the cell reservoir chamber was de-aerated prior to the experiment.

To observe the evolution of the anode in the step-by-step method, a sequence of constant potentials was imposed ranging from the open circuit potential (OCP) of the TCP-passivated aluminum to the point of failure (E_{pit}), which is similar to the anodic hardening process performed on TCP-passivated AA2024-T3 alloys in the previous section. Meanwhile a neutron beam impinged on the TCP-coated Al anode from above (penetrating the Si wafer, which is nearly transparent to neutrons) and was reflected at the interface between coating surface and electrolyte. NR measurements were conducted as function of imposed anodic potential. A series of scattering length density (SLD) profiles was generated by inversion of the *R-q* data, revealing the evolution of the TCP film and underlying Al in response to the increasing potential.

The split cell re-configured for cathode NR interrogation is shown in Figure 2(b). Both the anodic and cathodic wafers have an Al layer covered by a TCP film. Because Ce(III) is reported to have both anodic and cathodic inhibition character, we sought to minimize Ce(III) inhibition on anode surface by controlling the TCP-passivated Al anode at the transition stage (polarized at -730 mV), which is beyond the effective Ce(III) anodic inhibition range, but still below stable pitting failure. This transition is discussed in Section 5.7. As it turned out, however, the anode may have passivated after 24 h. The corresponding reduction reaction occurs uniformly on the cathode counter electrode, which is interrogated by the neutron beam. The Ce(III) NaCl-D_2O electrolyte (0.1 g $CeCl_3$ and 1 g NaCl per 100 ml D_2O) in the cell reservoir chamber was de-aerated prior to the experiment. A sequence of SLD profiles of the cathode reveals the structure and chemical composition of the TCP layer as a function of time. Cathodic inhibition was verified in a separate conventional electrochemical experiment at University of Cincinnati using the Gamry PCI4 300 potentiostat.

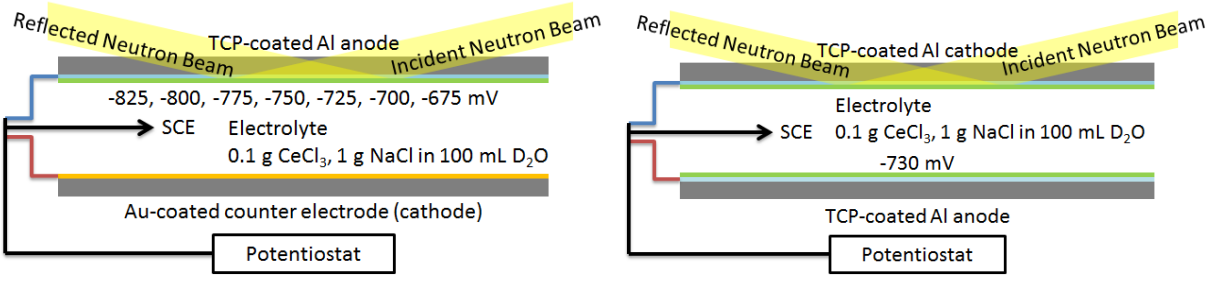

Figure 2. (a) Schematic of the split liquid cell set up for observing Ce(III) anodic inhibition. Liquid space is separated into three cavities, a bulk reservoir in middle and two thin reaction layers on both sides. The angle of the incidence is greatly exaggerated for demonstration, Details are found elsewhere. [21] (b) Schematic of the cell setup for investigating Ce(III) cathodic inhibition. The cell is flipped compared to (a), presenting the TCP-coated Al counter electrode (cathode) on top for NR interrogation.

4.11 Aluminum Anodizing

4.11.1 Voltage-controlled anodizing

In preparation for anodizing experiments AA2024 or pure Al-coated wafers were diced into rectangular pieces (35 mm × 15 mm) and dipped in a 20-wt% sulfuric acid at a constant voltage (2, 5, 10, and 20 V) controlled by a DC power supply (Instek, Corp.). A graphite counter electrode was used. The distance between the cathode and anode was fixed at 10 cm. At each voltage, samples were anodized for up to 120 s. The final samples were air-dried for 24 hours after cleaning in de-ionized water.

4.11.2 Simultaneous current-limited and voltage-controlled anodizing

To control the film growth and thickness a new current limited, voltage controlled protocol was perfected. The current density limit was set on the DC power supply, but the constant voltage mode was chosen (15 or 20 V). If the measured current density during anodizing is lower than the current limit, the voltage will be maintained at the fixed value. Otherwise, the current density will be controlled at the current density limit.

4.11.3 Sealing of Anodic Aluminum Oxide

The AAO was sealed by four methods: hot water, hot 5 g/L nickel acetate, cold 5 g/L nickel acetate, and saturated nickel acetate. The hot sealing methods were used on Al foils and Al coupons only (thin coatings delaminate at high temperatures). Cold sealing methods were applied on all samples. For hot sealing, the samples were immersed in boiling water (100 °C) or hot nickel acetate (90 °C) for 30 minutes. For *ex situ* cold sealing, the samples were immersed in nickel acetate solutions (both 5g/L and saturated) for 30 minutes. *In situ* NR sealing experiments were performed on thin AAO coatings on Si wafers for up to 12 hours. In this case the bath was 50g/L nickel acetate, which is close to saturation.

5. Results and Discussion

5.1 Wafer-based metal substrates

Typical corrosion coupons are not suitable for reflectivity measurements. A key requirement to adapt reflectivity to corrosion research is to achieve metal substrates of sufficient smoothness to ensure high quality reflectivity data from inhibitor films deposited on the substrates. To this end a series of metals were physically deposited on silicon wafers by e-beam evaporation as described in Section 4.2. The neutron and x-ray reflectivity characterizations were carried out following the strategies described in Section 4.5.1.

As aerospace Al alloys are the primary substrates of concern, the morphology of aluminum alloy AA2024 films on Si wafer was studied in detail. In addition, annealing of layered Al-Cu was investigated as a possible route to Al-Cu alloys with tailored microstructure.

5.1.1 Morphology of AA2024 substrate

After considerable experimentation with Al-Cu deposition methods we found that AA2024 films could be deposited by e-beam evaporation of an AA2024-T3 ingot. Both the NR and XRR results (below) show that the deposited film has the same composition and density as the alloy ingot used as the e-beam target. NR was performed on the Surface Profile Analysis Reflectometer (SPEAR) at the Los Alamos National Laboratory and the Spallation Neutron Source (SNS) at Oak Ridge National Laboratory.

The neutron reflectivity (NR) data on e-beam deposited AA2024 are shown in Figure 3**.** The thickness of alloy is (400 ± 5) Å with a (30 ± 5) Å porous Al_2O_3 layer on top. The scattering length density (SLD) of bulk metal is (2.13 ± 0.05) × 10^{-6} $Å^{-2}$, which is consistent with the calculated SLD based on the alloy's known density and atomic composition. The SLD of the porous oxide layer is (2.8 ± 0.3) × 10^{-6} $Å^{-2}$, which is 66% as dense as crystalline Al_2O_3.

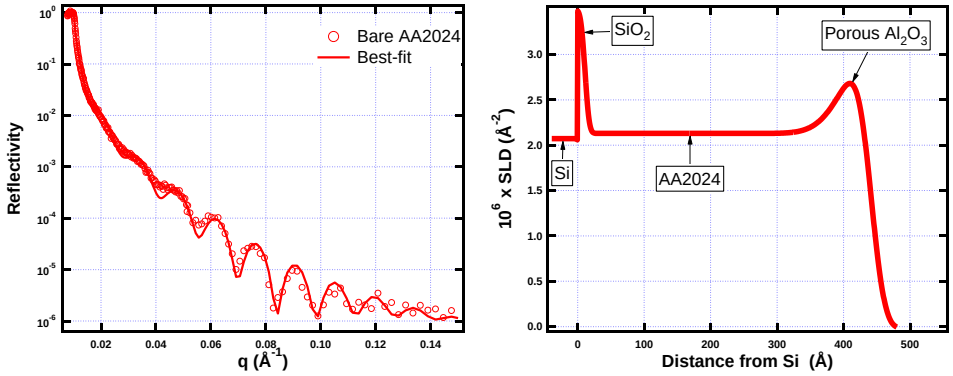

(a) (b)

Figure 3. (a) SPEAR NR data from e-beam deposited AA 2024. (b) Best-fit SLD profile corresponding to the solid line through the data points in (a).

The corresponding XRR data for AA2024 substrate are shown in Figure 4**.** The x-ray SLD profile indicates the same structure as found by NR (Figure 3). The x-ray SLDs of bulk AA2024 layer and top oxide layer are (23.5 ± 0.5) × 10^{-6} $Å^{-2}$ and (26.0 ± 0.5) × 10^{-6} $Å^{-2}$ respectively.

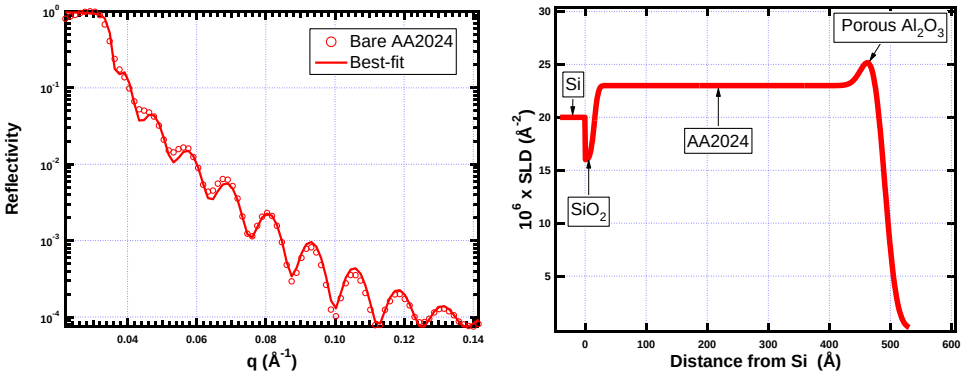

(a) (b)

Figure 4. (a) XRR data from as-prepared bare AA 2024. (b) Best-fit SLD profile corresponding to the solid line through the data points in (a).

5.1.2 Morphology of pure copper substrate

Deposition of pure Cu proved to be more difficult than Al since Cu does not wet the Si wafer. To deposit Cu, a titanium buffer layer (63 ± 5 Å) was first deposited on the wafer to aid adhesion of Cu.

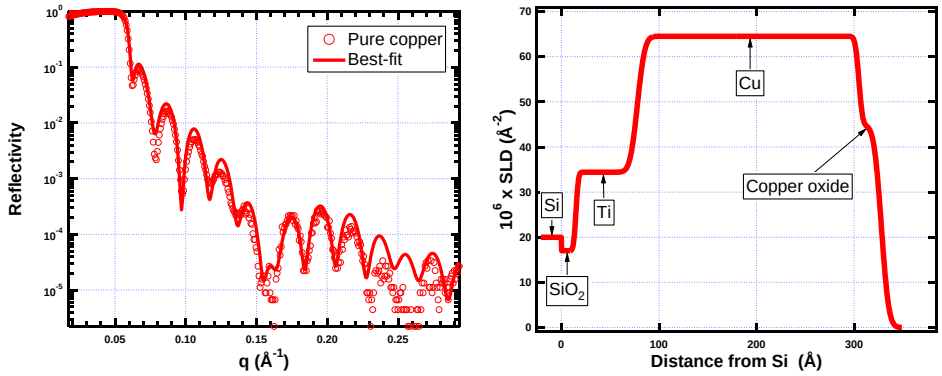

(a) (b)

Figure 5. (a) XRR data from as-prepared Cu-coated wafer with a Ti buffer layer. (b) Best-fit SLD profile corresponding to the solid line through the data points in (a).

Cu deposits nicely on the Ti buffer layer. The XRR of pure copper on Ti is shown in Figure 5**.** The thickness of copper is (227 ± 5) Å with a (23 ± 5) Å thick copper oxide layer on top. The x-ray SLDs of bulk copper layer and top oxide layer are (64.5 ± 0.5) × 10^{-6} Å^{-2} and (44.8 ± 0.5) × 10^{-6} Å^{-2} respectively. The SLDs of the two layers are consistent with the theoretical values.

5.1.3 Annealing of layered Al-Cu alloy films

In an attempt to create an e-beam deposited alloy film with tunable microstructure, the annealing of a layered Cu-Al system was observed by XRR. A thin layer of Cu (100 Å) was deposited on top of a 200-Å pure Al layer. The vacuum annealing protocol followed (300 ˚C for 15 hours followed by 450 ˚C for 5 min) was proposed by Nancy A. Missert (Sandia National Laboratories), a leading expert on the physics of metals.

The XRR data before and after annealing are compared in Figure 6(a), which gives the SLD profile of the annealed sample. A SLD gradient normal to the surface was observed in the alloy

film, which indicates the Cu and Al ingredients are not uniformly distributed. Nevertheless, Cu penetrates the entire Al layer. The SLD of Al-enriched region just above silicon wafer is (33.0 ± 0.5) × 10^{-6} Å^{-2}, which indicates the volume ratio of Al/Cu is 75/25. On the top surface, the SLD is (40.0 ± 0.5) × 10^{-6} Å^{-2}, which indicates the volume ratio of Al/Cu is 58/42.

Considering the Cu content in AA2024 is 3.8-4.9 wt%, the above annealing procedure is adequate to transform the layered pure Al and pure Cu in proper thickness ratio into uniform Al-Cu alloy. This experiment shows that it will be possible to investigate the impact of Cu content on inhibitor film structure, although such experiments have yet to be attempted.

Interestingly, a simple two-layer model cannot fit the un-annealed film. We have yet to find a structure that can reproduce the measured XRR data.

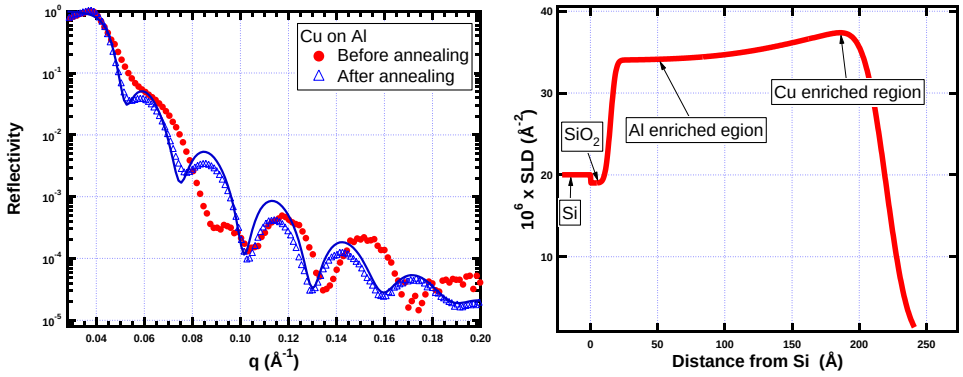

(a) (b)

Figure 6. (a) XRR data from a layered Al-Cu sample before (red dots) and after (blue triangles) annealing. (b) Best-fit SLD profile of annealed sample corresponding to the solid blue line through the data points in (a).

5.1.4 Metal substrate thickness optimization

A thick AA2024 (around 2 μm) substrate was also prepared and characterized by XRR. As shown in Figure 7(a), the featureless curve without fringes indicates the film is too rough to be characterized by reflectivity. Data in Figure 7 demonstrate that the rough surface of thick metal substrates results in a rough inhibitor film. The roughness is sufficient to wash out the fringes of the reflectivity curves. Therefore, a thick metal substrate does not provide the advantage hoped for in the downstream data analysis. We therefore used thin alloy films for subsequent inhibitor studies. Later we did successfully prepare thicker films suitable for anodization studies (Section 5.8).

5.2 Vanadate inhibitor films (V films)

5.2.1 Precursor exposure optimization

Vanadate films prepared by 30-s and 60-s exposure to the vanadate precursor were measured by XRR in the as-prepared dry state. As shown in Figure 8(a), the XRR data from the 30-s film has sharp fringes (red circles), which indicate a smooth film. According to the SLD profile shown in Figure 8(b), the total thickness of the inhibitor film is 960 ± 5 Å, which is in the desirable range for NR and XRR. After 60 s of growth, however, the inhibitor film becomes thick and rough.

The resulting reflectivity curve (blue triangles, Figure 8(a)) primarily exhibits fringes that arise from the alloy substrate. The signal from the inhibitor layer shows up as small fringes as marked in black circles on Figure 8(a). The thickness estimated from the width of these fringes is 1890 ± 10 Å, which is close to the upper resolution limit of NR. By comparing the two data sets, the 30-s exposure results in higher quality film than 60-s treatment, so 30-s exposure was used for subsequent experiments.

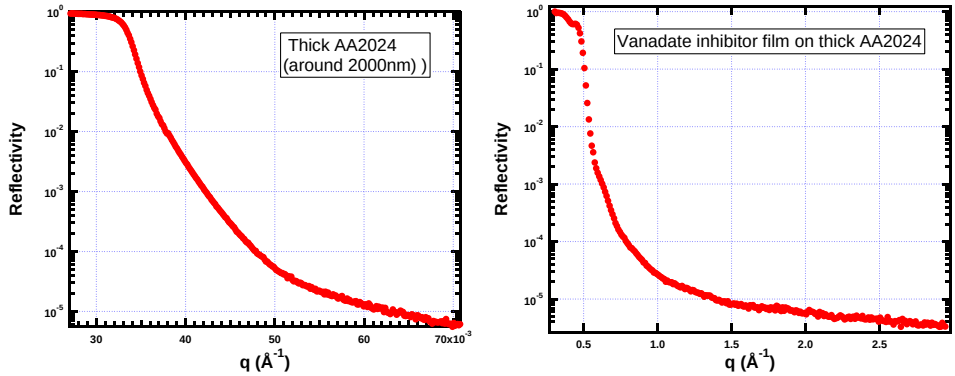

(a) (b)

Figure 7. (a) XRR data from as-prepared thick AA2024 (around 2 µm). No fringes were observed indicating a rough surface. (b) XRR data from as-prepared vanadate inhibitor film grown on thick AA 2024. The absence of fringes limits the amount of information that can be extracted from the XRR profiles.

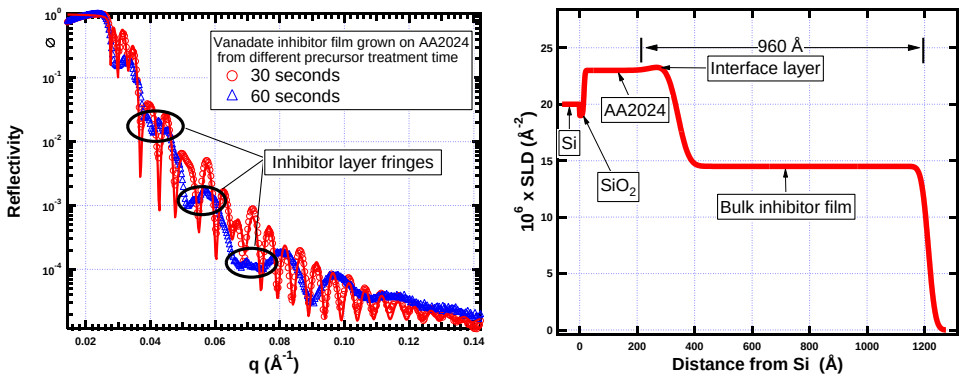

(a) (b)

Figure 8. (a) XRR data from vanadate films after 30-s (red circles) and 60-s (blue triangles) precursor solution treatment in the as-prepared dry state. (b) Best-fit SLD profile of inhibitor film after 30-s precursor solution treatment corresponding to the solid red line through the data points in (a).

5.2.2 Structure of as-prepared vanadate conversion coatings (VCC)

The virgin structure of vanadate films made from H_2O and D_2O precursor solutions were examined by NR.

As shown in Figure 9 and Figure 10, a simple one-layer uniform film model does not fit the experimental data well. Layered models are required to get credible fit to the reflectivity curves as shown in Figure 11 and Figure 12 for the samples made from H_2O and D_2O precursor solutions respectively. Based on the best-fit SLD profile the as-prepared vanadate conversion coating (VCC) film has a layered structure.

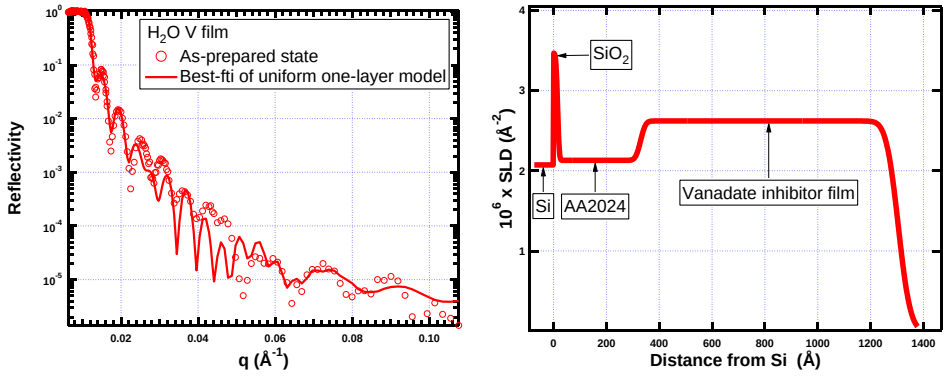

(a) (b)

Figure 9. (a) SPEAR NR data from vanadate films made from H_2O precursor solution. (b) Best-fit assuming a one-layer, uniform-SLD profile corresponding to the solid line through the data points in (a). The films were exposed to the inhibitor solution for 30 s. A two-layer model (Figure 11) fits considerably better.

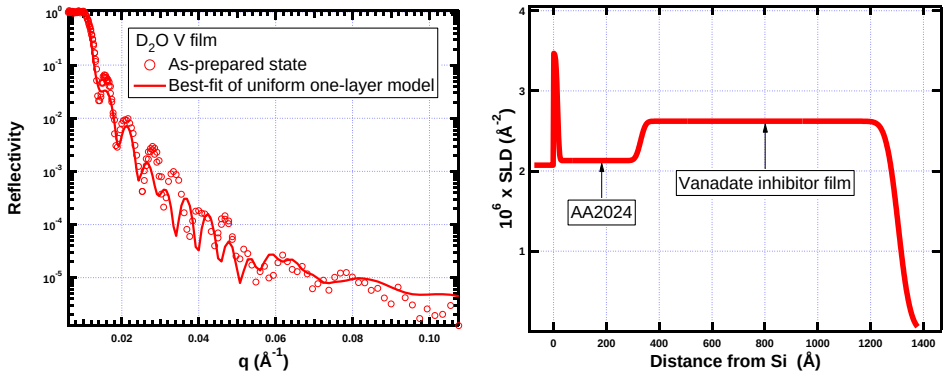

(a) (b)

Figure 10. (a) NR data from vanadate films made from D_2O precursor solution. (b) Best-fit to a one-layer, uniform-SLD profile corresponding to the solid line through the data points in (a). The films were exposed to the inhibitor solution for 30 s. A two-layer model fits considerably better (Figure 12).

VCC films prepared from H_2O precursor solution: Figure 11 reveals a (95 ± 5)-Å bottom layer at the metal-coating interface and a (990 ± 5)-Å top layer accounting for the rest of the coating thickness. The neutron SLD of bottom interface layer is (1.45 ± 0.05) $\times 10^{-6}$ Å^{-2}, while the top layer is (2.60 ± 0.05) $\times 10^{-6}$ Å^{-2}. The thickness of metal substrate (315 ± 5 Å) is less than the original metal film (400 ± 5 Å). No aluminum oxide layer is observed, which indicates the top part of the aluminum alloy layer is stripped by the precursor solution. The reduced SLD of bottom layer implies a higher concentration of vanadium, which has a negative neutron SLD. The characteristics of the as-prepared vanadate conversion coating (VCC) are summarized in Table 1.

Table 1. Structural parameters of as-prepared VCC film

	Thickness (Å)	SLD ($\times 10^{-6}$ Å^{-2})
Bottom layer	95 ± 5	1.45 ± 0.05
Top layer	990 ± 5	2.60 ± 0.05

VCC films prepared from D_2O precursor solution: As shown in Figure 12, the D_2O-solution-prepared sample has the same structure as the H_2O-solution-prepared case. The thickness of

bottom and top layers are (95 ± 5) Å and (880 ± 5) Å, respectively. The roughness of top surface is also around 40 Å. The SLDs of the layers are the same as H_2O-solution-prepared sample. The fact that the D_2O-solution-prepared and the H_2O-solution-prepared samples have the same neutron SLD for both bottom and top layers implies that the speciation of VCC film does not contain H and therefore, is not a hydrate. For both samples, the thickness of AA2024 substrate is less than the virgin metal film and no aluminum oxide layer is observed, which indicates the top part of AA2024 layer is stripped by the precursor solution.

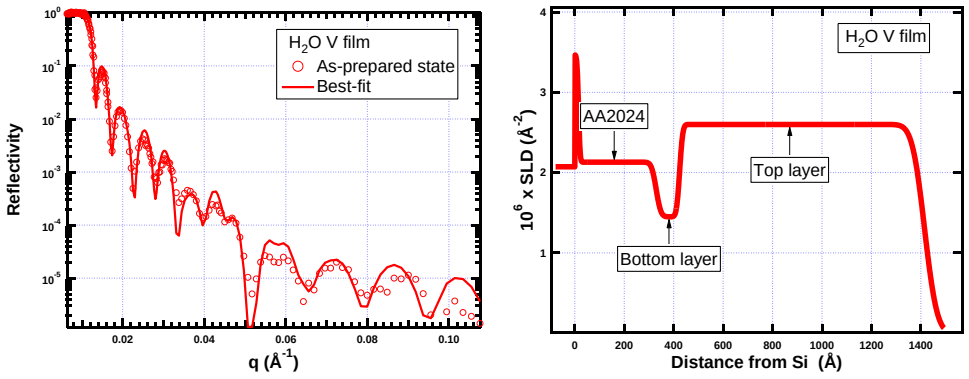

(a) (b)

Figure 11. (a) NR data from vanadate films made from H_2O precursor solution. (b) Best-fit two-layer, uniform-SLD profile corresponding to the solid line through the data points in (a). The low-SLD interface layer is required to fit the data adequately.

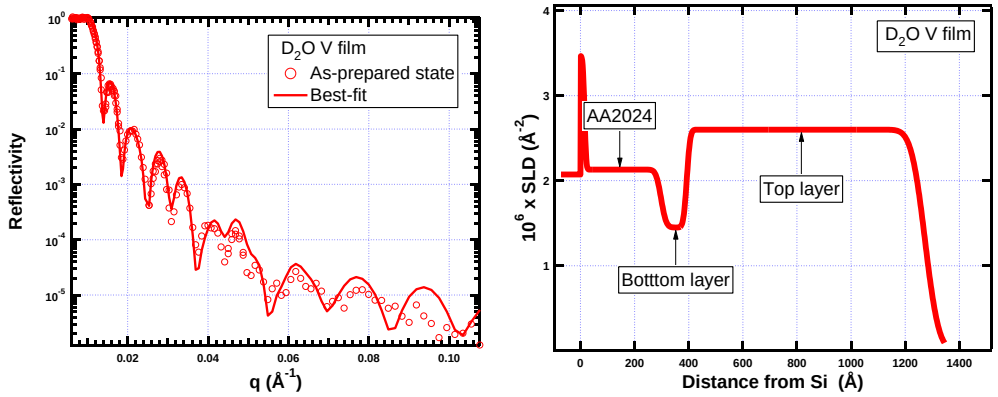

(a) (b)

Figure 12. (a) NR data from vanadate films made from D_2O precursor solution. (b) Best-fit two-layer, uniform-SLD profile corresponding to the solid line through the data points in (a). The low-SLD interface layer is required to fit the data adequately.

Based on above results, we propose a 4-stage process for the formation of VCC films on AA 2024.

First stage: Dissolution of metal surface. The acidic precursor dissolves the aluminum oxide and part of the aluminum, causing an increase of the pH near the metal surface.

Second stage: Fast precipitation. At elevated pH, vanadate precipitates from the solution and forms a thin hydrate layer and/or hydroxide gel. This layer forms in seconds and is relatively dense because of the high availability of vanadate ions and relatively high-pH environment compared with the next stage of film formation.

Third stage: Retarded growth. Because of the gel covering the metal surface dissolution of metal slows. The gel continues to polymerize leading to densification within the initial stage-2 gel layer, and further growth of a porous layer at the film-solution interface. The film growth ceases as densification impedes dissolution of metal. The layer formed at this stage is less dense and contains less vanadium than the bottom layer.

Fourth stage: Condensation. When the film dries the gel fully dehydrates, leading to an insoluble film containing complex compounds consisting mainly of aluminum, vanadium and oxygen.

5.2.3 Hydrophobicity and porosity of VCC film

Hydrophobicity is an important factor for anticorrosion performance. The hydrophobicity of vanadate inhibitor films was examined by NR on films exposed to saturated D_2O vapor. D_2O rather than H_2O is used to increase neutron contrast. The sample was sealed in an Al can (Figure 13) with saturated D_2O atmosphere at room temperature for 12 hours to ensure the system reaches equilibrium. The thin wall of aluminum can is transparent to neutrons. By comparing the SLD profiles of the as-prepared dry state and water-vapor-conditioned state, the water response of vanadate inhibitor films can be determined.

Because the absorbed water usually resides in molecular-level free space inside the film,[22, 23] the D_2O-equivalent volume fraction, Φ_{D2O} , can be calculated with Equation 8 assuming no film swelling:

$$\Phi_{\mathrm{D2O}} = \frac{\mathrm{SLD}_{\mathrm{saturated}} - \mathrm{SLD}_{\mathrm{as-prepared}}}{\mathrm{SLD}_{\mathrm{D2O}}} \tag{8}$$

where the subscripts "saturated" and "as-prepared" mean the state of equilibrium with D_2O vapor and the virgin dry state, respectively.

In the presence of swelling or shrinking, Equation 8 is modified to Equation 9:

$$\Phi_{\mathrm{D2O}} = \frac{\mathrm{SLD}_{\mathrm{saturated}} \times t_{\mathrm{saturated}} - \mathrm{SLD}_{\mathrm{as-prepared}} \times t_{\mathrm{as-prepared}}}{\mathrm{SLD}_{\mathrm{D2O}} \times t_{\mathrm{saturated}}} \tag{9}$$

where *t* is the thickness of the film.

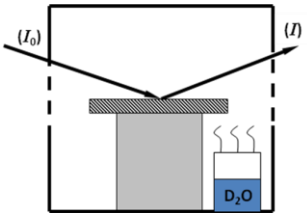

Figure 13. Experimental set up for "vapor conditioning" experiments.

The reflectivity curves from the as-prepared film and the same film exposed to saturated D_2O vapor at room temperature for 12 hours are shown in Figure 14**(a)**. D_2O rather than H_2O is used for these experiments since it shows better contrast than H_2O and much less incoherent scattering.

Under D_2O-vapor conditioning, the reflectivity increases compared to the as-prepared state due to the absorption of D_2O. As shown in Figure 14**(b)**, at equilibrium, a D_2O wetting layer is observed at the air-side surface with a thickness of (920 ± 10) Å, which causes the critical edge shift to higher q. D_2O penetrates the entire top bulk film with a 9% swelling effect. The SLD of the saturated bulk top layer increases from $(2.60 \pm 0.05)\times10^{-6}$ Å^{-2} to $(2.70 \pm 0.1)\times10^{-6}$ Å^{-2}, implying the D_2O volume fraction is 5 vol% according to Equation 9. Interestingly, for the bottom interface layer, the SLD and thickness retain their original values. There is neither significant swelling nor moisture absorption, which indicates that the interface region is hydrophobic. The water barrier behavior is summarized in Table 2.

Table 2. Water absorption behavior of VCC films

	Thickness (Å)		$10^6\times$SLD (Å^{-2})		D_2O vol%	
Layer	Bottom	Top	Bottom	Top	Bottom	Top
As-prepared	95 ± 5	780 ± 5	1.45 ± 0.05	2.60 ± 0.05	N/A	N/A
D_2O-vapor conditioning	95 ± 5	850 ± 10	1.45 ± 0.05	2.70 ± 0.1	0	5

Because the SLD of VCC film at the metal interface is unchanged on exposure to water vapor, the interfacial film is hydrophobic, which is preferred for anti-corrosion applications.

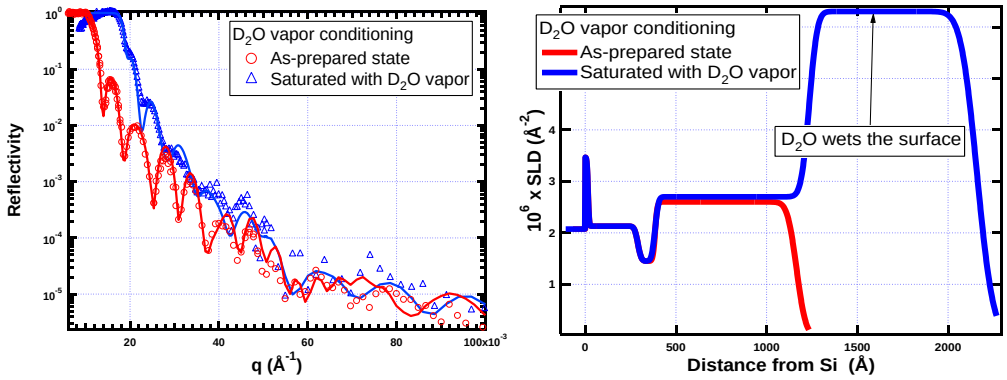

(a) (b)

Figure 14. (a) SPEAR NR data from vanadate film when in as-prepared dry state (red circles) and at equilibrium with D_2O vapor (blue triangles). The solid lines through the data points are the best fits corresponding to the SLD profile in (b).

5.2.4 Speciation of VCC film

According to Equation 2, the SLD of a material depends only on its atomic composition and mass density. The ratio of x-ray and neutron SLD, Φ, is a function of atomic composition only:

$$\Phi = \frac{\mathrm{SLD_{x-ray}}}{\mathrm{SLD_{neutron}}} = \frac{\sum_{\mathrm{molecule}} Z_i r_e}{\sum_{\mathrm{molecule}} b_i} \quad (10)$$

where, Z_i, is the atomic number and r_e is the bound, coherent scattering length of an electron. Since i is determined by the atomic composition, the film composition can be calculated by combining XRR and NR results on the same sample.

As discussed in Section 5.2.2, the VCC film is not hydrated. Assuming the inhibitor film only contains vanadium and oxygen, the chemical formula of VCC film can be written as V_2O_x. Therefore, the Equation 10 becomes:

$$\Phi = \frac{SLD_{x\text{-}ray}}{SLD_{neutron}} = \frac{(2Z_V + xZ_O) \times r_0}{2b_V + xb_O} = \frac{12.88 + 2.24x}{0.58x - 0.076} \quad (11)$$

Substituting Φ values for interface and bulk layer into Equation 11, the only unknown, x, can be calculated. Once the speciation, x is determined from the XRR/NR SLD ratio, the density, ρ, of each layer can also be calculated according to Equation 2.

Based on above strategy, the atomic formulas for bottom and bulk top layers are V_2O_5 and V_2O_{12}, respectively. The corresponding densities of bottom and bulk top layers are (1.55 ± 0.02) g/cm^3 and (1.84 ± 0.02) g/cm^3 respectively. The formula of top bulk layer is not stoichiometric, which is caused by the over simplified assumption that only vanadium and oxygen are present in the system. According to literature, VCC film contains other elements (O, Fe, Al and C) besides vanadium.[15] Regardless, this analysis indicates that the vanadium is enriched at the metal-coating interface.

5.2.5 Response to water immersion and high temperature baking

The stability of inhibitor films was determined by challenging the VCCs by immersion in liquid H_2O at room temperature and baking in vacuum at 200 °C for 24 hours. These data have not been successfully inverted yet, but some general conclusions can be drawn.

After immersion in H_2O at room temperature for 24 hours, the VCC film was measured by NR in re-dried state. The corresponding NR spectra are shown in Figure 15 and Figure 16 for water immersion and baking respectively. Changes in the VCC film are revealed by comparing the NR data before and after exposure. As indicated by the arrows, the first dip shifts to the right implying the increased film SLD. According to the fringe-width increase, the film thickness decreased from 700 ± 20Å to 630 ± 20 Å. Similar shifts are observed for the vacuum dried case in Figure 16. These observations warrant further investigation.

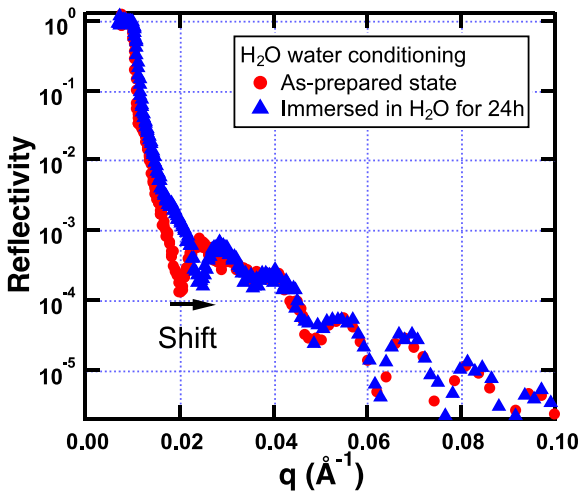

Figure 15. SPEAR NR data from vanadate film before (red dots) and after immersion in H_2O at room temperature for 24 hours (blue triangles). We have not identified a SLD model that adequately reproduces these data.

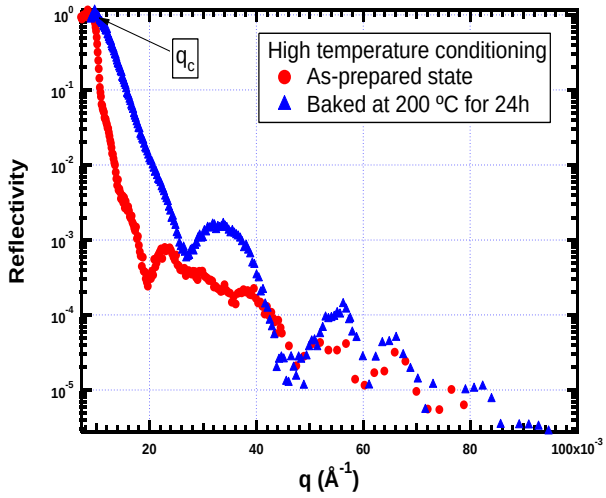

Figure 16. SPEAR NR data from VCC film before (red dots) and after 200 ˚C conditioning in vacuum for 24 hours (blue triangles).We have not identified a SLD model that adequately reproduces these data.

5.2.6 Vanadate films under an epoxy top coating

To demonstrate the ability of NR to probe buried films, VCC films under an epoxy top coating were measured by NR in the as-prepared dry state. The film structure of vanadate inhibitor films was successfully determined without damaging the epoxy layer on top.

Figure 17 gives the NR reflectivity curve and the corresponding SLD profile of a VCC film under an epoxy top coating. The layered film structure is shown in Figure 17(b). The epoxy layer is 680 ± 10 Å thick and has a SLD of 1.4 ± 0.05 × 10^{-6} $Å^{-2}$. This experiment demonstrated the capability of reflectivity technology as a non-destructive probe to determine the composition and structure of buried coating layers, which not possible by any other technique.

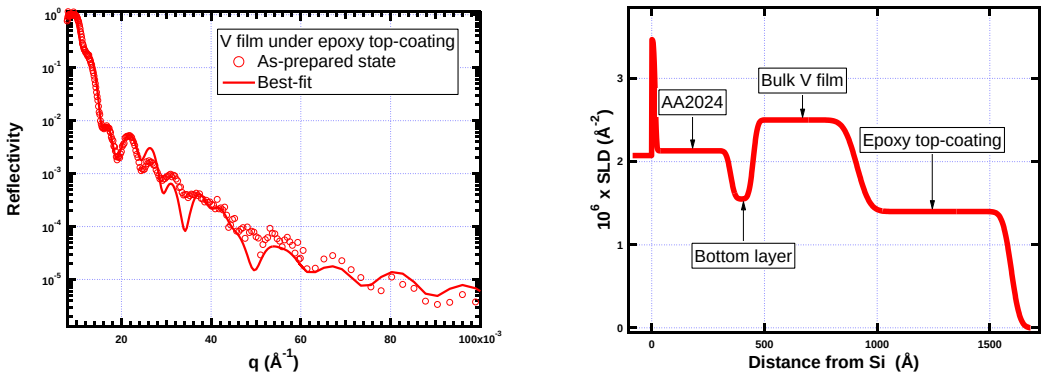

(a) (b)

Figure 17. (a) SPEAR NR data from epoxy coated VCC film in as-prepared dry state. The solid line through the data points is the best fit corresponding to the SLD profile in (b).

5.2.7 Effect of $K_3Fe[CN]_6$

Potassium ferricyanide, $K_3Fe(CN)_6$, is used as an accelerator for the Cr^{6+}/Cr^{3+}-Al^0/Al^{3+} redox couple in chromate conversion coating system.[24] To determine the impact of $K_3Fe[CN]_6$ on the vanadate system a formulation without $K_3Fe[CN]_6$ was characterized by NR. As shown in Figure 18(b), only a (40 ± 10) Å film formed on the AA2024 substrate. The average SLD of the film is (1.0 ± 0.4) × 10^{-6} Å^{-2}, which is substantially lower than the film made from full recipe as described in Section 4.6.1. The roughness of the vanadate film is comparable to its thickness. Although the fit in Figure 18 is not perfect, the analysis is sufficient to verify that $K_3Fe[CN]_6$ plays an important role to achieve thick, dense films.

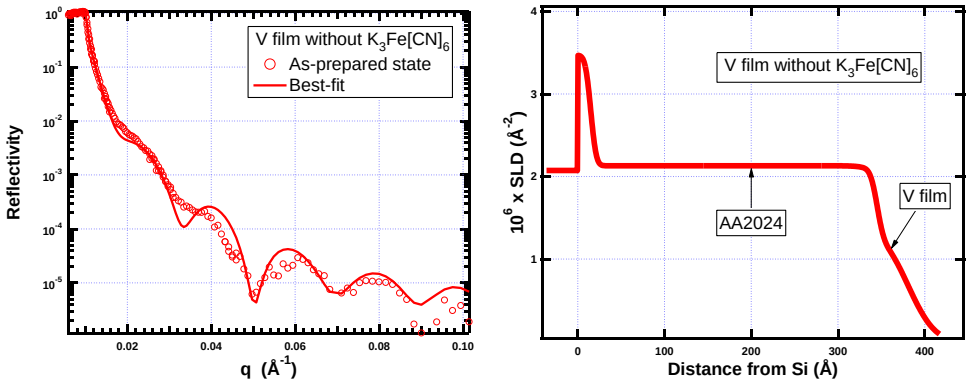

(a) (b)

Figure 18. (a) SPEAR NR data from VCC film made from a formulation without $K_3Fe[CN]_6$ in the as-prepared dry state. The solid lines through the data points are the best fits corresponding to the SLD profile in (b).

5.2.8 Summary regarding VCC films

To our knowledge this study of vanadate conversion coatings is the first analysis of the composition profile of a conversion coating. The important conclusion is that corrosion protection depends on a very thin barrier layer right at the metal interface. Water not only wets the VCC film, but also penetrates most of the film at a level of 5 vol%. Only the thin barrier layer protects the metal from water

5.3 Trivalent chromium process (METALAST® TCP-HF) system

5.3.1 H_2SO_4 activation

H_2SO_4 activation of the metal surface is necessary before deposition of Trivalent Chromium Process (TCP) passivation films. Our Al alloy-coated wafers have a mere 400 Å-thick Al coating, so the activation process had to be carefully controlled to avoid stripping the entire film. Therefore we measured the evolution of the metal substrate on exposure to 40 vol% H_2SO_4. By comparing the XRR data after immersion for 5 s, 15 s, 30 s, and 60 s, we observed the stripping of the native oxide followed by dissolution of the metal itself. Based on the XRR SLD profile (Figure 19), the oxide layer can still be identified after 5-s immersion. This alumina layer protects the underlying metal for about 15 s. The thickness of Al alloy layer changes little in this period. Once alumina is completely consumed, the vulnerable Al alloy is exposed and dissolves quickly (Figure 19 (d)).

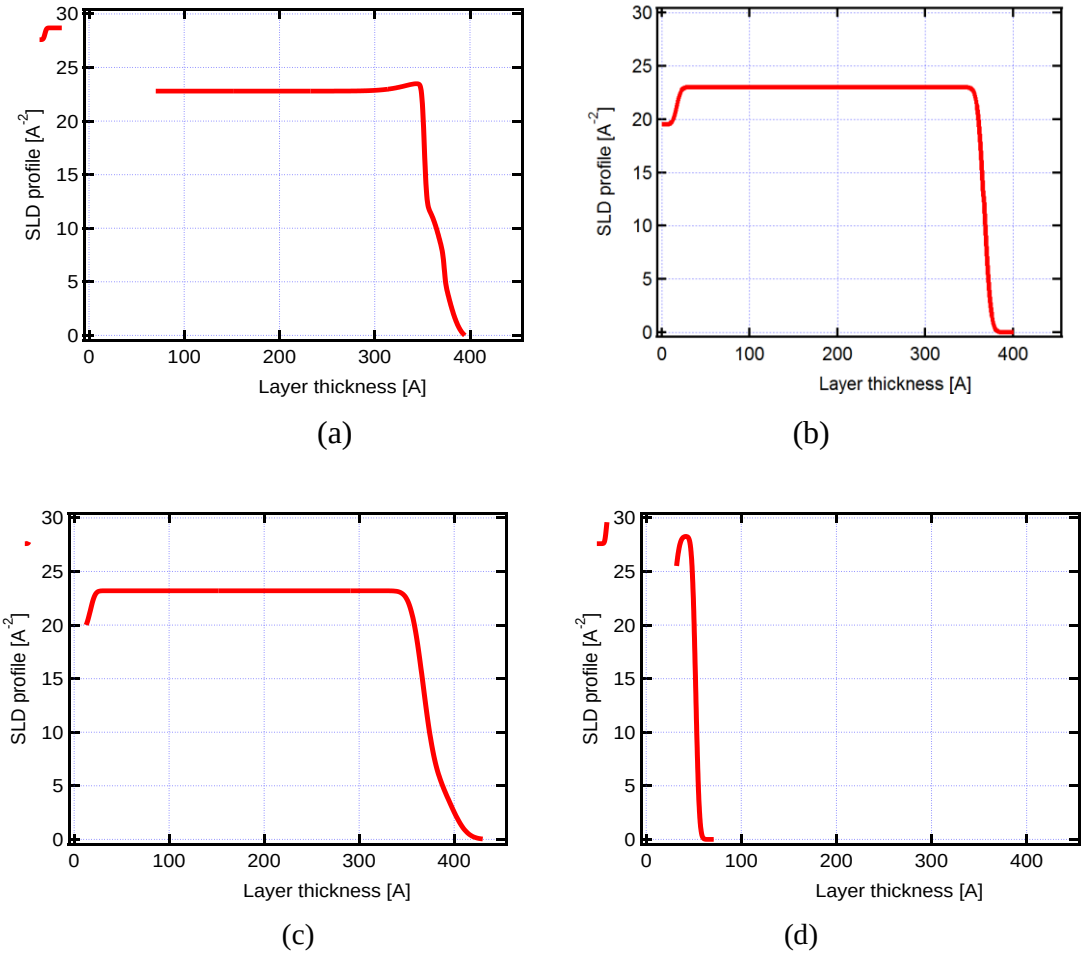

Figure 19. XRR data from Al-alloy-coated wafers exposed to 40 vol% H_2SO_4: (a) SLD after 5 s immersion (b) SLD after 15 s, (c) SLD after 30 s, (d) SLD after 60 s immersion.

By comparing these four SLD profiles, passivation behavior of alumina layer is confirmed. In order to prepare a good conversion coating, this passivation layer must be removed before the subsequent immersion step. Due to the Lewis-base nature of the Al alloy, acid etching is so fast

that its final thickness is hard to predict. Activation must cease before the alumina layer is completely removed. Balancing these requirements, 30 s was chosen as the optimized time for acid activation.

5.3.2 Film structure of TCP immersion films

We successfully prepared TCP films on Al-alloy-coated wafers by two methods, immersion and EA-deposition. In the immersion method, the alloy-coated Si wafers were first activated by immersion in 40 vol% H_2SO_4 for 30 s. After activation, the rinsed wafer was immersed in 25 vol% TCP solution (diluted METALAST® TCP-HF) for 3 minutes, rinsed and dried in air.

XRR data for all samples prepared by immersion show a three-layer structure (Figure 20). The three layers are a) an Al-alloy layer, which is thinner than the native alloy layer, b) a middle film layer I, which is about 300-Å thick, and c) a top layer II, which has the lowest SLD, and is only 100-Å thick.

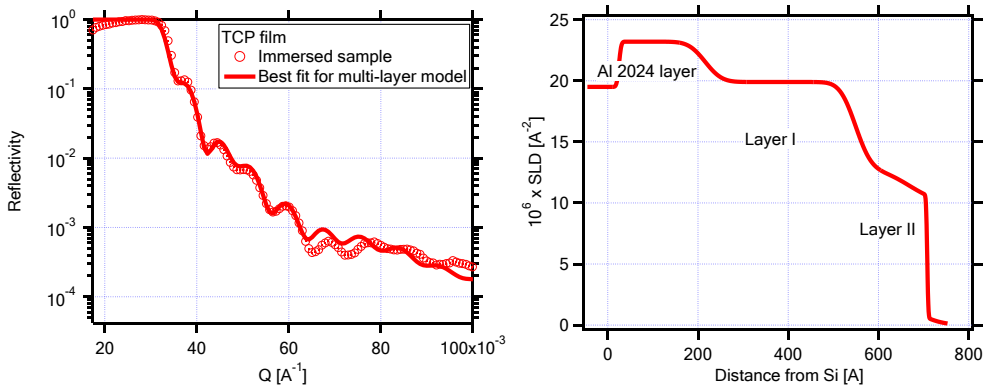

(a) (b)

Figure 20. (a) XRR data for METALAST®TCP film prepared by immersion. The line is the best fit to a 3-layer model. (b) SLD profile based on data in (a). Two TCP layers are observed on top of a thinned Al-alloy layer.

The density of layer II is only half that of layer I, indicating the existence of pores or channels. The porous nature of layer II is less desirable from a corrosion-protection perspective. These results show that a uniform, thick film is difficult to achieve by immersion.

The observed structure of the immersed samples (Figure 20(b)) is consistent with the film-formation mechanism postulated by Wen et al. for trivalent chromium conversion coatings.[25] The driving force for Cr(III) deposition comes from the rise in pH near the metal surface[26-29] caused by redox reactions on the heterogeneous, heat-treated alloy. [30] The oxidation reaction occurs on Al-rich matrix (similar to our alloy substrates) accompanied by proton reduction on Cu-rich inclusions, which are absent in our films. Cu inclusions are absent because the films are deliberately not heat-treated.

Oxidation and dissolution of the alloy surface were confirmed by the XRR SLD profiles (Figure 20(b)), which show reduction of the Al layer thickness from 350 ± 5 Å to 180 ± 5 Å in 3 minutes, which is equivalent to a corrosion current of 270 µA/cm^2. This rapid rate is promoted by the presence of F^- ions in the TCP solution (based on the METALAST® composition, TCP solution contains BF_4, Zr^{4+}, F^-, besides Cr^{3+}. Fluoride ions increase the solubility of Al^{3+} and impede the

formation of Al_2O_3.[31] The proton reduction reaction, on the other hand, increases the solution pH, triggering the precipitation of Cr(III) and Zr(IV) hydroxides at the alloy surface.

The two-layer structure can be accounted for within the Wen mechanism. Layer 1 forms during the initial rapid pH rise. The high availability of Cr(III) and Zr(IV) leads to $Cr(OH)_x^{(3-x)+}$ and $Zr(OH)_x^{(4-x)+}$ cations. These ions migrate to cathodic regions on the metal surface where they are completely hydrolyzed, forming a dense layer composed of $Cr(OH)_3$ and $Zr(OH)_4$. Once formed, however, layer 1 retards both oxidation of the alloy and the reduction of protons. Proton reduction is favored at certain transient cathodic sites causing an increase in the local pH.

Since Zr hydroxide precipitates at lower pH than Cr hydroxide, precipitation of Zr occurs before precipitation of Cr, leading to Zr enrichment on transient cathodic spots. Once a fresh passivation layer covers these spots, however, proton reduction transfers to other places, thus activating new precipitation sites. This fluctuating localized precipitation leads to a rough, defective surface, which we observe in Figure 20(b) as a broadened interfacial region ("layer 2") of lower SLD.

Immersion-TCP films are not particularly desirable for further NR and XRR study. Desirable films are simple, uniform and thick enough to be measured precisely. Immersion films are not simple because dissolution of Al and deposition of TCP occur simultaneously. $Al^{(III)}$ compounds inevitably remain in the deposited film, compromising determination of film speciation. Also immersion film has a rough and defective surface. The interpretation of this non-uniform structure is more difficult than for a single-layer structure. Moreover, the thicknesses of layer 1, and the AA2024 layer are comparable, which makes it more difficult to sort out the true profile. Finally, film growth quickly ceases, leading to rather thin films whose thickness cannot be measured with sufficient accuracy to assess the effect of drying and baking. These considerations motivated us to restrict further analysis to EA films.

5.4 Electro-assisted (EA) and the simplified trivalent chromium process system

5.4.1 Structure of as-prepared EA- TCP film

The electro assisted method of TCP film deposition is described in Section 4.8. Here we show that this method, in conjunction with a simplified TCP formulation, leads to controllable films whose thickness and roughness are compatible with XXR and NR.

In contrast to the immersion samples, NR data for the as-prepared samples with different EA deposition times (1 min, 2 min, 4 min) all show a single-layer structure with a thin, high-SLD interfacial layer (Figure 21) at the alloy surface. The thickness of the bulk deposition layer increases in proportion to the polarization time with minimal change in SLD (Figure 22).

The 4-min EA samples were dried at room temperature. To check the consistency of the protocol, three identically prepared samples were examined. After exposure to the ambient environment for more than 4 days, NR data (Figure 23) show a significant change in SLD profile compared to Figure 21. The average thickness of bulk film decreases to 730 ± 20 Å and the average SLD increases to $1.98 \pm 0.06 \times 10^{-6}$ Å^{-2}. These results indicate a factor-of-two densification. This change could be due to dehydration and/or structural re-organization of the film. Regardless, these results highlight the importance of curing on film density and composition.

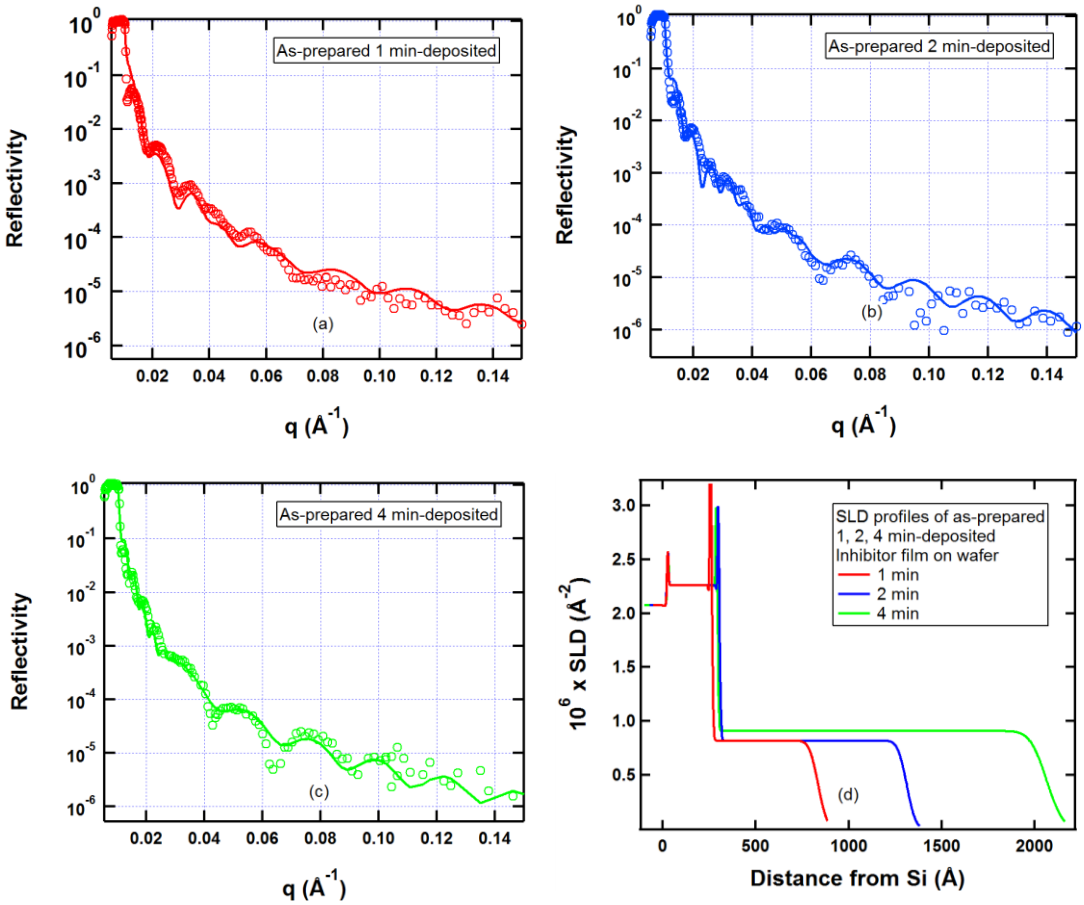

Figure 21. (a), (b), (c) SNS NR data of as-prepared EA-TCP film after 1, 2, and 4-min EA deposition in 25-vol% simplified TCP solution. (d) Resulting SLD profiles. A dense interfacial layer is observed at the alloy surface. The bulk layer thickness increases with deposition time. The peak at 0 Å is the SiO_2-covered Si surface. The peak at about 270 Å is a dense interface layer. The data could not be adequately fit without this interfacial layer. The EA deposition method is describe in Section 4.8.

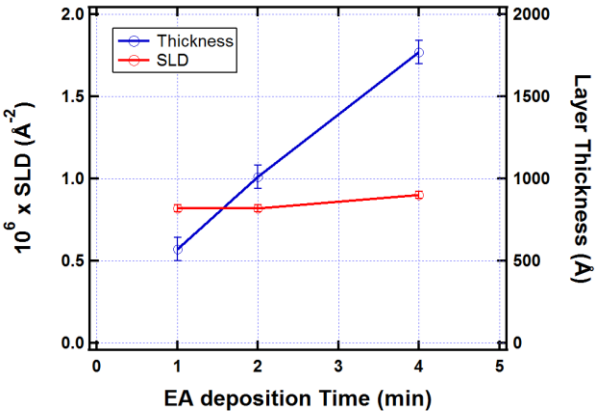

Figure 22. As-prepared EA-TCP film thickness and SLD as a function of EA deposition time. A constant film growth rate with minimal change in SLD is observed.

Samples A and B in Figure 23 were further baked at 150 ˚C at 3×10^{-3} Torr for 6 hours to dehydrate the film fully. The dehydrated films showed further decrease in layer thickness with corresponding SLD increase (Figure 24). The thickness changes from 730 ± 20 Å to 620 ± 20 Å. The SLD increases from $1.98 \pm 0.06 \times 10^{-6}$ Å^{-2} to $2.72 \pm 0.06 \times 10^{-6}$ Å^{-2}.

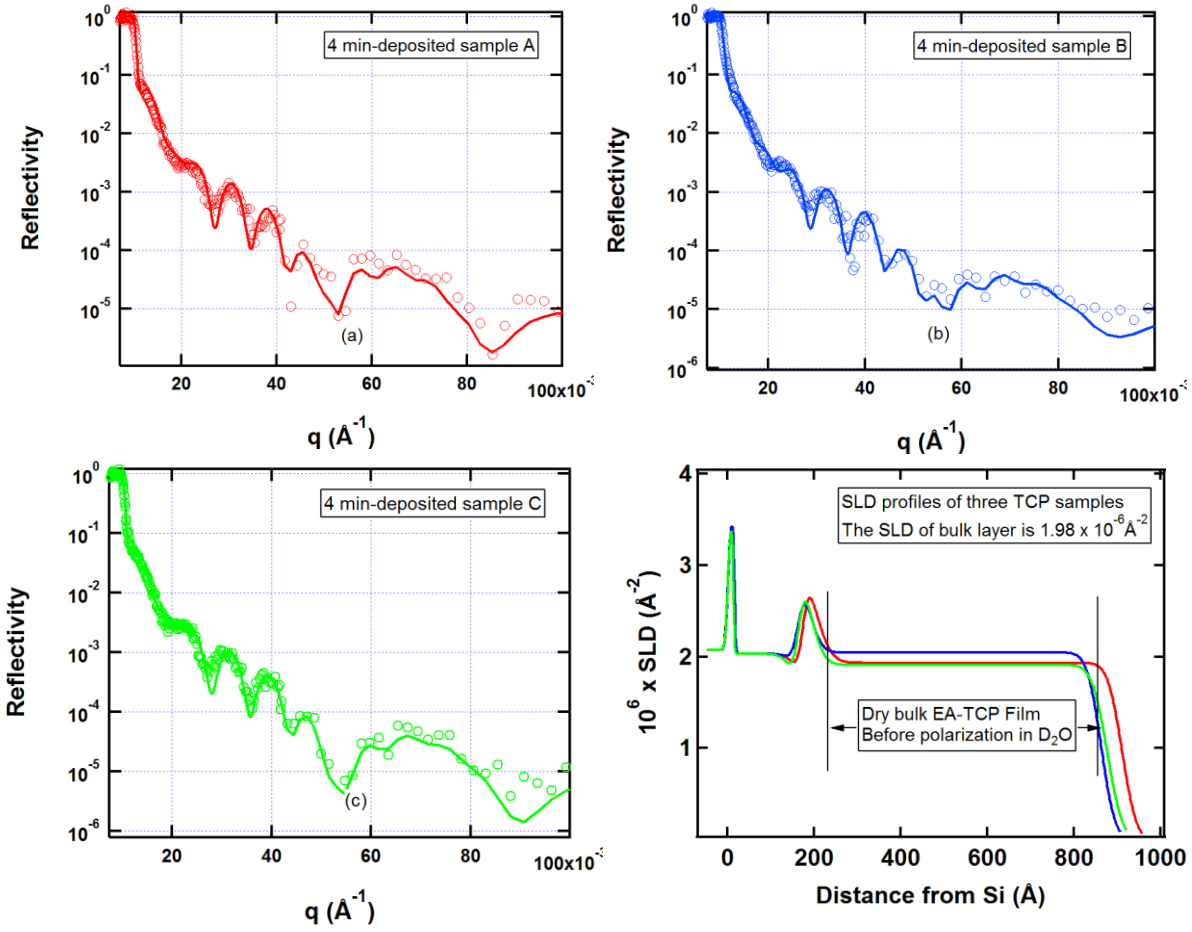

Figure 23. SPEAR NR data for three identical EA-TCP samples, A, B, C, after 4-days drying at ambient conditions. (d) SLD profiles.

5.4.2 RT drying and vacuum baking

5.4.3 Speciation of EA-TCP film by XRR and NR

XRR data for 4-min film (sample C) were also collected (Figure 25). The SLDs of the layers are different due to differences in scattering lengths for x-rays and neutrons but the layer structure and thicknesses are the same. This consistency justifies layered-structure model.

The neutron SLD profiles of EA-TCP film before and after vacuum baking (Figure 24(b) & (d)) show not only film compression but also dehydration (loss of crystal hydrate water). Comparing the bulk EA-TCP film before baking (730 ± 20 Å, SLD = $1.98 \pm 0.06 \times 10^{-6}$ Å^{-2}) and after baking (620 ± 20 Å, SLD = $2.72 \pm 0.06 \times 10^{-6}$ Å^{-2}), the scattering lengths per unit area are 1450

$\pm$ 80 $\times$ 10^{-6} Å^{-1}, and 1690 $\pm$ 90 $\times$ 10^{-6} Å^{-1} respectively. The increase is due to the loss of water during baking, as water has a negative scattering length.

The film hydration fraction can be determined assuming a film composition of $Cr_2O_3 \cdot xZrO_2 \cdot nH_2O$. The ratio x will be discussed later. Another assumption is that the EA-TCP film is totally dehydrated after 6 h baking at 150 ˚C, 3×10^{-3} Torr, leaving anhydrous oxide, $Cr_2O_3 \cdot xZrO_2$. The hydrate number of crystalline hydrous oxide (n in $Cr_2O_3 \cdot xZrO_2 \cdot nH_2O$) before baking is calculated as follows.

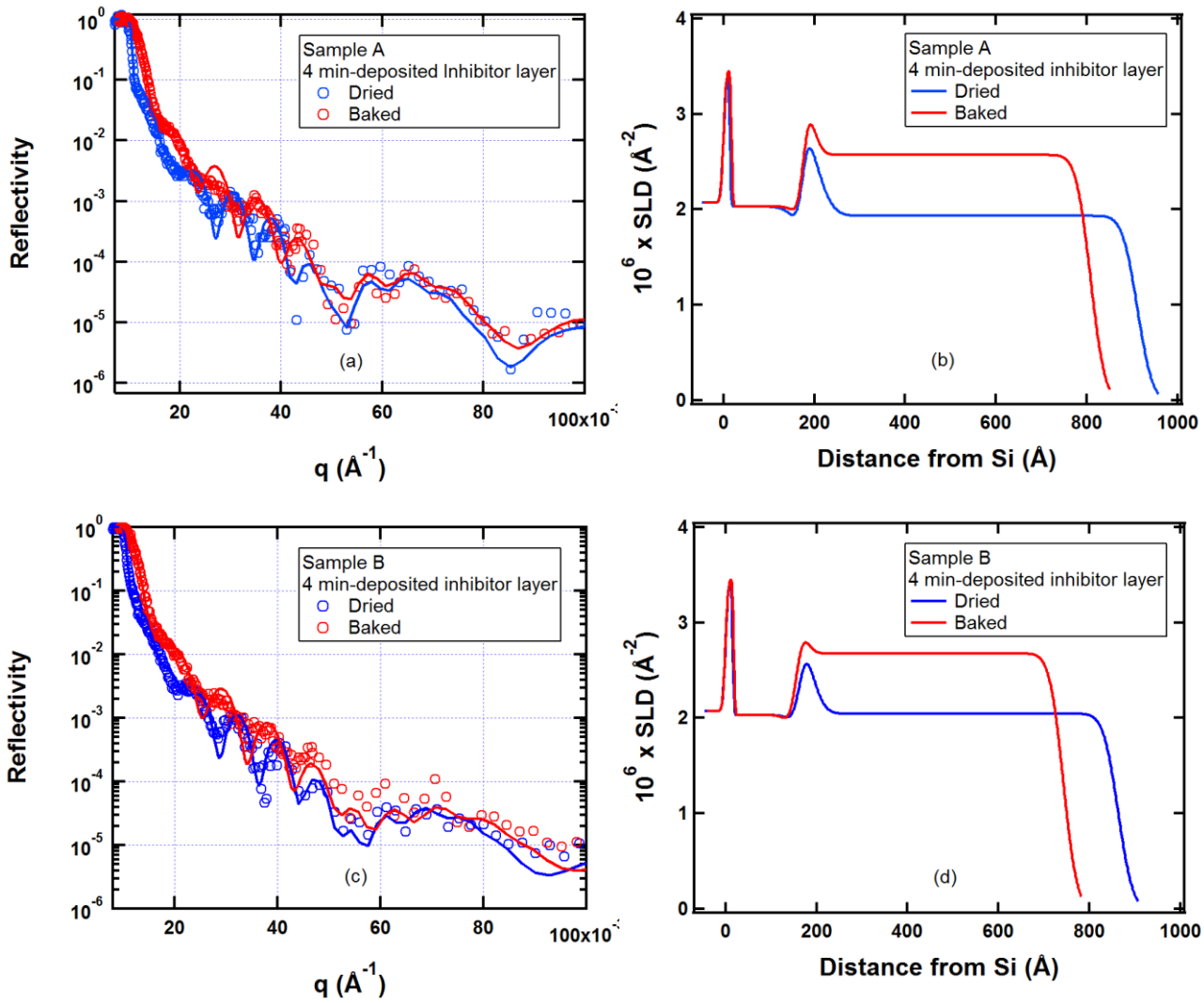

Figure 24. SPEAR NR data before and after vacuum baking of samples A and B in Figure 23.

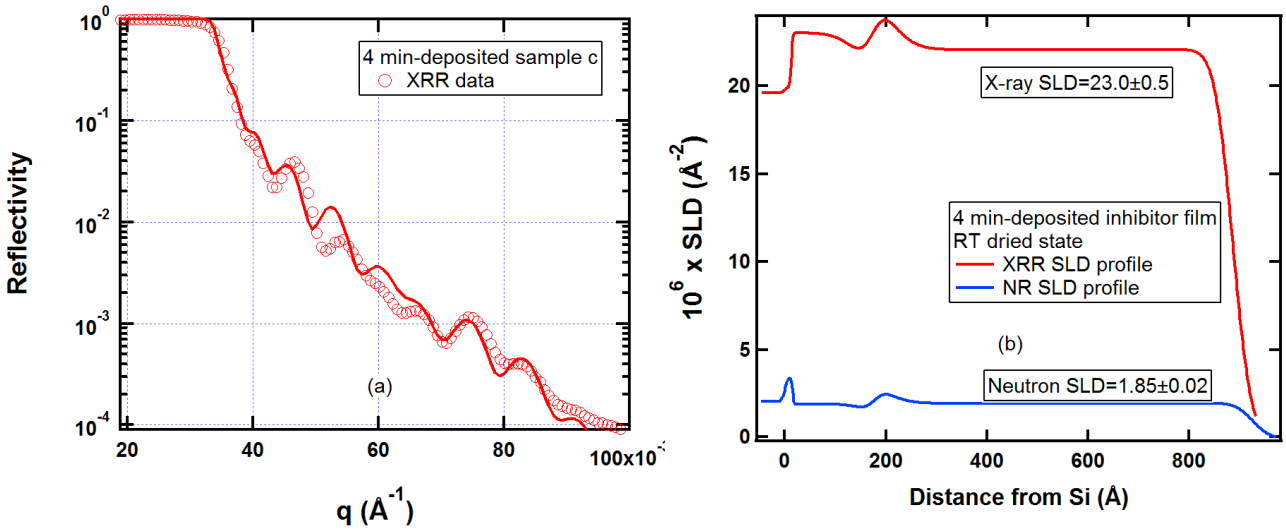

Figure 25. (a) XRR data and (b) XRR and NR SLD profile comparison for sample C (RT dried state). NR data are from SPEAR (Figure 23).

Equation 12 and 13 are the SLD of the EA-TCP layer before (hydrous, h) and after baking (anhydrous, a).

$$\mathrm{SLD_h} = \rho_\mathrm{h} \frac{N_\mathrm{A}}{M_\mathrm{h}} b_\mathrm{h} \tag{12}$$

$$\mathrm{SLD_a} = \rho_\mathrm{a} \frac{N_\mathrm{A}}{M_\mathrm{a}} b_\mathrm{a} \tag{13}$$

Where ρ_h is density of hydrated film and ρ_a is the density of the anhydrous film; N_A is Avogadro's number; b is the corresponding molecular scattering length, M_a, and M_h are the molecular weight of anhydrous and hydrous coating species.

Define the SLD of "anhydrous part" of hydrous metal oxide crystal in the deposition layer before baking as $\mathrm{SLD_{h-H2O}}$ (i.e. $\mathrm{SLD_{h-H2O}}$is the SLD of $\mathrm{MO_m}$ in the $\mathrm{MO_m}{\cdot}n\mathrm{H_2O}$ species).

$$\mathrm{SLD_{h-H2O}} = \rho_\mathrm{h} \frac{N_\mathrm{A}}{M_\mathrm{h}} (b_\mathrm{h} - n \times b_\mathrm{H2O}) = \rho_\mathrm{h} \frac{N_\mathrm{A}}{M_\mathrm{h}} b_\mathrm{a} \tag{14}$$

Based on metal-atom conservation (i.e., no Cr and Zr atoms are lost after vacuum baking) the number of hydrous oxide molecules ($Cr_2O_3\cdot x ZrO_2\cdot nH_2O$) is equal to the number of anhydrous oxide molecules ($Cr_2O_3\cdot xZrO_2$). Then the total scattering length from the dry part of hydrous oxide layer ($Cr_2O_3\cdot xZrO_2$ species in $Cr_2O_3\cdot xZrO_2\cdot nH_2O$) is equal to the total scattering length from the anhydrous oxide layer ($Cr_2O_3\cdot xZrO_2$ species in $Cr_2O_3\cdot xZrO_2$), as number of $Cr_2O_3\cdot xZrO_2$ species is constant and scattering length of $Cr_2O_3\cdot xZrO_2$ is unchanged. Additionally the total scattering length is the SLD times the volume:

$$SLD_\mathrm{h-H2O} \times V_\mathrm{h} = SLD_\mathrm{a} \times V_\mathrm{a} \tag{15}$$

where V is the volume of bulk layer. V is proportional to layer thickness (730 ± 20 Å and 620 ± 20 Å) since area is conserved.

The neutron scattering lengths and SLDs of the relevant compounds are listed below:

$$b_{Cr2O3} = 2.46 \times 10^{-4}\text{Å} \tag{16}$$

$$b_{\mathrm{ZrO2}} = 1.876 \times 10^{-4}\text{Å} \tag{17}$$

$$b_{\mathrm{H2O}} = -0.167 \times 10^{-4}\text{Å} \tag{18}$$

$$b_{\mathrm{a}} = b_{\mathrm{Cr2O3{\cdot}}x\mathrm{ZrO2}} = b_{\mathrm{Cr2O3}} + x\, b_{\mathrm{ZrO2}} \tag{19}$$

$$b_{\mathrm{h}} = b_{\mathrm{Cr2O3{\cdot}}x\mathrm{ZrO2{\cdot}}n\mathrm{H2O}} = b_{\mathrm{Cr2O3}} + x\, b_{\mathrm{ZrO2}} + n\, b_{\mathrm{H2O}} \tag{20}$$

$$\mathrm{SLD_h} = (1.98 \pm 0.06)\ \times 10^{-6}\text{Å}^{-2} = \rho_{\mathrm{h}} \frac{N_{\mathrm{A}}}{M_{\mathrm{h}}} (2.46 + 1.876x - 0.167n) \times 10^{-4}\text{Å} \tag{21}$$

$$\mathrm{SLD_a} = (2.72 \pm 0.06)\ \times 10^{-6}\text{Å}^{-2} \textbf{(}\text{from Figure 24}\textbf{)} \tag{22}$$

Starting from Equation 15 the right hand side is taken directly from the SLD and thickness measured in the anhydrous baked state in Figure 24 and the left hand side is calculated from Equations 14 using Equation 19 along with the thickness in the dried state from Figure 24 (Equation 22). Note that area is conserved during drying, so thickness is proportional to volume.

$$\begin{aligned} &\rho_{\mathrm{h}} \frac{N_A}{M_{\mathrm{h}}} (2.46 + 1.876x) \times 10^{-4}\text{Å} \times (730 \pm 20)\text{Å} \\ &= (2.72 \pm 0.06) \times 10^{-6}\text{Å}^{-2} \times (620 \pm 20)\text{Å} \end{aligned} \tag{23}$$

Multiplying and equating the left and right hand sides of Equation 21 and 23, $\rho_{\mathrm{h}} \frac{N_A}{M_{\mathrm{h}}}$ can be canceled, leaving *x* and *n* in the equation. After simplification, the hydrate number, *n*, is expressed as a function of *x*: $n = i + jx$, $i = 2.10 \pm 0.55$, and $j = 1.60 \pm 0.45$

Therefore $Cr_2O_3{\cdot}xZrO_2{\cdot}nH_2O$ is rewritten as Equation 24:

$$Cr_2O_3{\cdot}i\mathrm{H_2O}{\cdot}x(ZrO_2{\cdot}j\mathrm{H_2O}) \quad \text{with} \quad i = 2.10 \pm 0.55,\ j = 1.60 \pm 0.45 \tag{24}$$

Note that the hydrate number for chromium, *i*, is independent of the ratio, *x*, which specifies the zirconium oxide fraction.

The ratio *x* between $Cr_2O_3 \cdot iH_2O$ and $ZrO_2 \cdot jH_2O$ is calculated based on comparison of neutron SLD and x-ray SLD of the bulk EA-TCP layer in Figure 25**.**

$$\frac{\mathrm{SLD_{X-ray}}}{\mathrm{SLD_{Neutron}}} = \frac{23.0 \ \pm 0.5}{1.85 \ \pm 0.02} = 12.43 \ \pm 0.40 \tag{25}$$

$$\frac{\mathrm{SLD_{X-ray}}}{\mathrm{SLD_{Neutron}}} = 12.43 \ \pm 0.40 = \frac{b_{\mathrm{h,x-ray}}}{b_{h,neutron}} = \frac{(26.05 + 20.17x) \times 10^{-4}\text{Å}}{(2.10 + 1.60x) \times 10^{-4}\text{Å}} \tag{26}$$

where $b_{\mathrm{h,x-ray}}$ is x-ray scattering length and $b_{\mathrm{h,neutron}}$ is neutron scattering length of $Cr_2O_3 \cdot iH_2O \cdot x(ZrO_2 \cdot jH_2O)$. From Equation 26 the ratio, *x*, between $ZrO_2 \cdot jH_2O$ and $Cr_2O_3 \cdot iH_2O$ is 0.85 ± 0.14, so the as-deposited film composition is:

$$Cr_2O_3 \cdot iH_2O \cdot x(ZrO_2 \cdot jH_2O) \qquad (i = 2.10 \pm 0.55,\ j = 1.60 \pm 0.45 \text{ and } x = 0.85 \pm 0.14) \tag{27}$$

In contrast to Equation 27, one un-published report finds that TCP film contains little Cr. The lower Cr content in conventional films is consistent with Pourbaix diagrams, which show that Zr(IV) precipitates at a lower pH than Cr(III). In conventional deposition, the pH gradient is determined by Al dissolution rate, which decreases once the passivation film forms. The resulting shallow pH gradient favors Zr precipitation, eventually reaching the point where only Zr will precipitate. In EA deposition, by contrast, the pH gradient is steeper and is maintained by polarization. As a result, Zr and Cr are more likely to co-precipitate, as we observe.

5.4.4 EA deposition process

In the EA method proton reduction is controlled electrochemically; film deposition, therefore, is controllable and sustainable over a long period of time. The resulting film is uniform and arbitrarily thick. In addition the film is not contaminated by Al atoms.

For EA deposition, the oxide layer and part of the alloy are removed via anodic polarization in 25-vol% TCP solution (Figure 26(a)). The wafer is then cathodically polarized in 25-vol% TCP solution, causing the deposition of a hydroxide film on the bare alloy surface. Although TCP solution contains BF_4^-, Zr^{4+}, F^-, besides Cr^{3+}, the alloy-coated wafer is under cathodic polarization during deposition. As a result Al dissolution is suppressed and BF_4^- and F^- anions are excluded from the cathode. Under these conditions the EA-TCP film should be a Zr(IV)/Cr(III) hybrid with no contamination from F, B or Al.

In contrast to the immersion method, the alloy layer is not dissolved during film deposition, since the anodic reaction is water oxidation, which occurs on the graphite counter electrode. Although oxygen bubbles were observed, it is possible that Cr^{3+} oxidation also occurs. The water reduction potential is about 1.2 V (SHE), whereas $Cr_2O_7^{2-}/Cr^{3+}$ is roughly 1.3 V (SHE). SHE means that the voltage is referenced to the standard hydrogen electrode. The proton reduction reaction proceeds on the wafer surface at a constant rate because the driving force for this reaction

(electrons) comes from the external power supply. Thus, in contrast to the immersion case, the pH gradient near metal surface is maintained. The EA-TCP deposition rate is only affected by the availability of the Cr(III) and Zr(IV)in the solution.

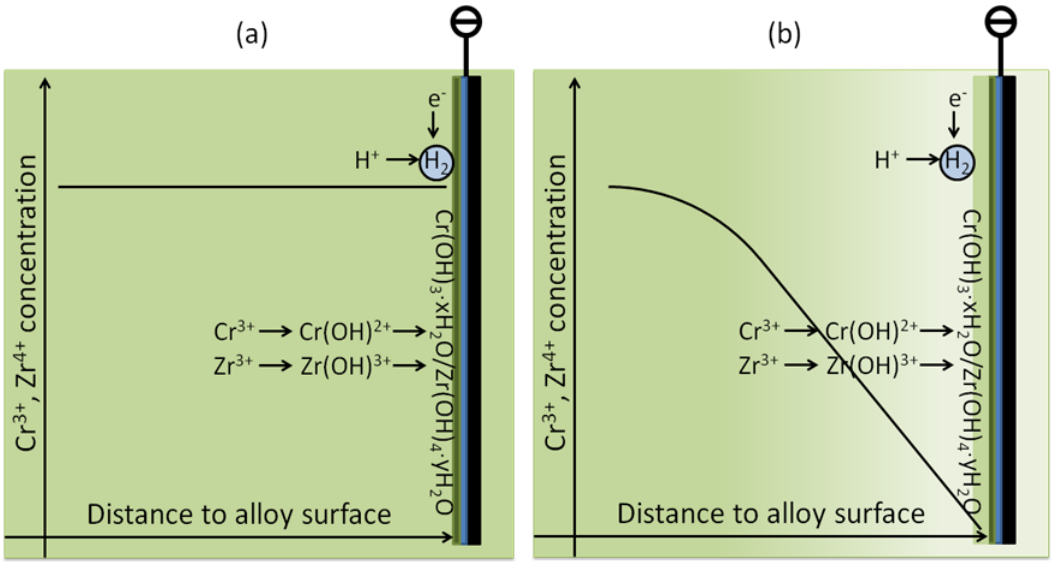

Figure 26. Schematics of TCP deposition via cathodic polarization in the initial state (a), and steady state (b) where a gradient in metal ion concentration exists. At high cathodic polarization, the reduction reactions rapidly transition from charge-transfer to diffusion control leading to kinetically-limited, steady-state growth.

The single layer structure observed in all as-prepared EA samples can be explained by a two-stage deposition (Figure 26): a fleeting initial state followed by continuous film growth. In the initial state the pH increases rapidly due to cathodic polarization leading to proton reduction and pH rise. Cr^{3+} and Zr^{4+} form hydroxy-cations that precipitate at the metal surface. The initial local concentration of Cr^{3+} and Zr^{4+} is high, a dense layer results. After a short period, these cations are quickly depleted so further deposition is limited by diffusion of Cr^{3+} and Zr^{4+} from bulk solution, leading to kinetically limited steady-state growth (Figure 26). During steady-state growth, electrons, protons, and Cr^{3+}, Zr^{4+} cations are all maintained at constant gradient. Therefore the EA-TCP film grows linearly with deposition time with little change in the film density or composition as shown in Figure 22.

Accelerator additives[31, 32] typically found in Cr(VI) and vanadate conversion coating systems such as F^- and $Fe(CN)_6^{3-}$ are not needed for EA deposition. Typically F^- is required for Al dissolution, and $Fe(CN)_6^{3-}$ is added to promote Al oxidation and Cr(VI) reduction. In the EA scheme these species are excluded during the cathodic polarization as discussed Xia and McCreery.[33]

5.4.5 Transition from hydroxide to crystal

Since the as-prepared EA-TCP film is a Zr(IV)/Cr(III) hydroxide complex, further evolution due to structural condensation is inevitable. NR data in Figure 21 and Figure 23 confirm this change.

Comparing the 4-min film (1680 ± 10 Å, SLD = 0.90 ± 0.02 × 10^{-6} $Å^{-2}$), and RT-dried film (730 ± 20 Å, SLD= 1.98 ± 0.06 × 10^{-6} $Å^{-2}$), thickness reduces while the scattering length per unit area (SLD × thickness) remains constant (1500 ± 40 × 10^{-6} $Å^{-1}$, and 1450 ± 80 × 10^{-6} $Å^{-1}$ respectively). The large difference in film thickness implies a structural change from amorphous to a more compact crystalline, perhaps from amorphous Zr(IV)/Cr(III) hydroxide to crystalline Zr(IV)/Cr(III) oxide ($Cr_2O_3 \cdot xZrO_2 \cdot nH_2O$).[31, 34] This transition partially occurred before the data in Figure 23 were collected.

5.4.6 EA-TCP film structure after vacuum baking

5.4.7 SIMS of EA-TCP film

SIMS data on EA-TCP film (Figure 27) confirm co-precipitation of Cr and Zr. The normalized peak intensities of ^{52}Cr and ^{90}Zr are 5.5×10^5 and 1.0×10^5 counts, after calibration by standards $CrK(SO_4)_2 \cdot 12H_2O$ (1.83 g/cm^3, ^{52}Cr = 3.5×10^5 counts) and K_2ZrF_6 (3.48 g/cm^3 ^{90}Zr = 5.7×10^5 counts). The $^{90}Zr/^{52}Cr$ atomic ratio is calculated to be 0.74 ± 0.16, confirming that the films contain comparable amounts of Zr and Cr.

The structure of TCP deposition films depends on how the films are deposited. Immersion films are different from EA films in that the latter grow linearly with cathodic polarization time after a thin dense layer forms at the metal interface.

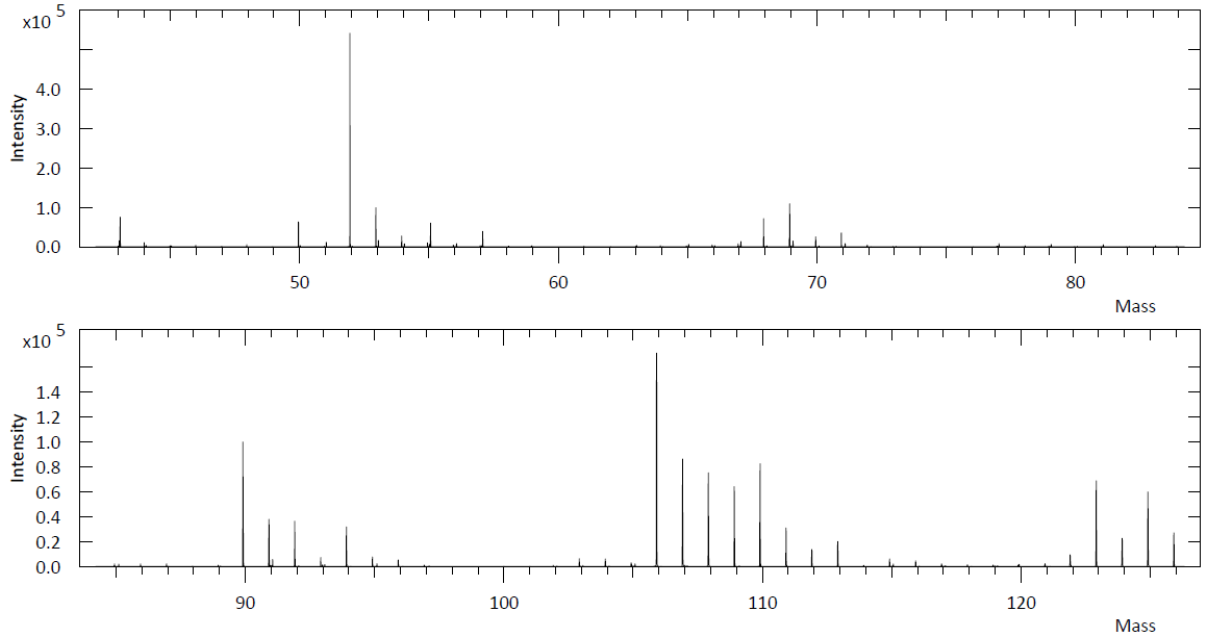

Figure 27. Positive-ion SIMS surface spectrum of EA-TCP film. Peaks at 50, 52, 53 are from Cr. Peaks at 90, 91, 91 and 94 are from Zr. Peaks between 106 and 111 are signals from the Pd substrate and ZrO_2. Peaks after 120 are due to Cr_2O_3.

5.4.8 Summary of EA deposition

EA deposition produces a denser, thicker TCP film compared to immersion. The dense interfacial layer between the metal and the bulk TCP deposition film is extremely thin due to rapid deposition in the initial state. Film thickness then depends on the time under cathodic

polarization. The composition of the film is $Cr_2O_3 \cdot iH_2O \cdot x(ZrO_2 \cdot jH_2O)$ (i =2.10 ± 0.55, j = 1.60 ± 0.45 and x = 0.85 ± 0.14) as determined by comparing the SLD before and after driving off the water of hydration by vacuum baking, and by comparing the neutron and x-ray SLDs. SIMS data from the EA-TCP film confirm co-deposition of Cr and Zr compounds.

5.5 *In situ* NR study of TCP passivity

Having established a deposition protocol and having determined the composition of the resulting films we no turn to the response of the films to a corrosive environment. We first compare bare Al with TCP-coated Al and then examine the influence of soluble Ce(III) inhibitor.

5.5.1 *In situ* NR of bare Al

A bare Al-coated wafer was tested first in the split liquid cell shown in

2. The NR data yielded information on the change in thickness of the Al layer when a constant potential of -930 mV vs. SCE was applied, which is an overpotential of +100 mV. This bare-metal study mimicked the Al-dominated anodic area on a bare AA2024-T3 surface.

Figure 28 shows the evolution of Al without TCP protection at a constant anodic potential in NaCl-D_2O solution in the split cell. We obtained NR curves (Figure 28(a)) at the beginning of polarization (blue), and after 3-h exposure (red). We measured low-angle $R - q$ snapshots at 0 – 20 min and 180 – 200 min. The 20-min snapshot has sufficient time resolution to capture the film thickness change during the active dissolution process.

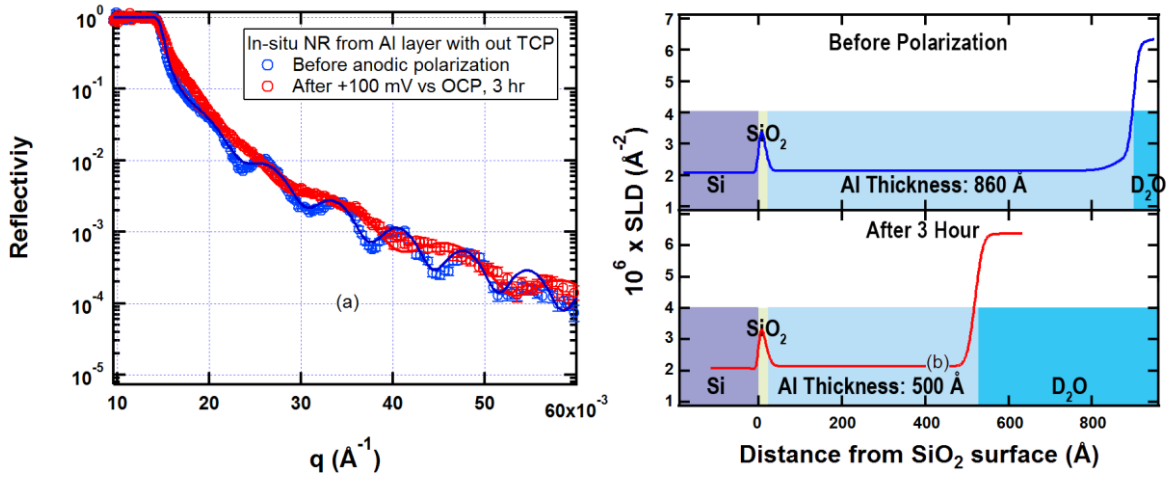

Figure 28. (a) SPEAR NR data (R − q plots) on a corroding Al layer in a split liquid cell. The data before and after 3-h exposure at 100 mV noble to the OCP in de-aerated NaCl-D_2O solution show that q spacing between fringes expands, indicating reduced thickness of Al layer. (b) SLD profiles based on the $R - q$ plots. The Al layer thickness changed by ~ 360 Å (from ~ 860 Å before exposure to ~ 500 Å after 3-hour exposure). A color scheme is adopted in the SLD profile to highlight the different layers present.

The 3-h reflectivity curve (red in Figure 28(a)) flattened after 3-h polarization, indicating a major structural change in the Al coating. Figure 28(b) gives the SLD profiles, which reveal the change in Al coating thickness. The 0-Å position on abscissa marks the surface of Si wafer. A native SiO_2 layer forms on Si with a thickness of 10 Å – 20 Å. Since SiO_2 has a higher SLD than Si, a

sharp peak is observed at the wafer surface. The SLD observed at large distances from the surface is the value expected for the NaCl-D_2O environment (6.37×10^{-6} Å^{-2}). The region between SiO_2 peak and NaCl-D_2O environment is the Al layer with a constant SLD of 2.14×10^{-6} Å^{-2}. Comparing the SLD profiles before (blue curve) and after 3-hour polarization (red curve), the thickness of Al changes from 860 ± 10 Å to 500 ± 10 Å.

The bare Al-coated wafer mimics the unprotected anodic area on AA2024-T3 when exposed to a corrosive environment. Also this experiment shows that the corrosion rate is matched to the time-resolution of the NR instrument. Below we show consistency between Al dissolution measured by NR and by the measured anodic current.

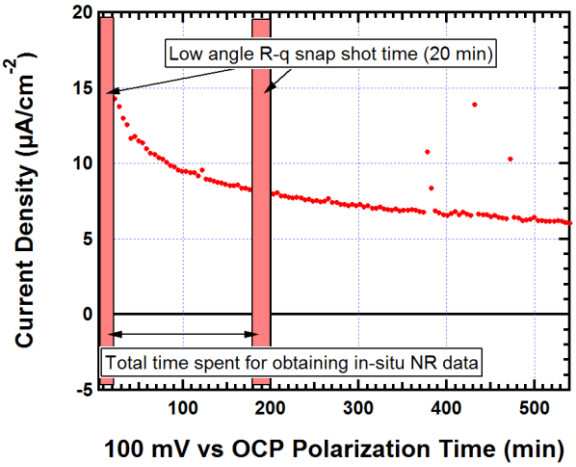

Figure 29. Current density recorded for bare Al in the split cell. The reduction in Al layer thickness is in agreement with the average in current density. The durations of the NR snapshots (Figure 28) are marked as vertical bars.

The *in situ* 3-hour polarization on the bare Al layer at an overpotential of +100 mV validates the correlation between the *in situ* electrochemical data and simultaneous NR SLD profiles. The current density collected indicates dissolution of the Al layer (Figure 28(b)). Assuming the anodic current is due to Al oxidation, the dissolved Al per unit area can be calculated based on integration of the measured current density between 0 and 180 minutes according to Faraday's Law.

$$F \times Z \times \frac{V \times \rho_{Al}}{A \times M_{Al}} = \int_0^{180\ min} i(t) \times \mathrm{d}t = 14600\ \mu\mathrm{C} \tag{28}$$

Where F is the Faraday's constant (96,485 C / mol); Z is the valence of Al^{3+}; V is the volume of dissolved Al; A in is total area of the corroding surface; ρ_{Al} is the mass density of Al; M_{Al} is the atomic weight of Al, i is the current density; and t is time. The dissolved Al in units of volume per unit area is calculated to be 380 ± 20 Å.

Based on the measured current density, the native oxide layer shows little resistance against anodic attack. The NR SLD profiles indicate the same behavior. Two NR *in situ* snapshots on the anode (Figure 28) were taken at 0 – 20 minutes and 180 – 200 minutes. The SLD profiles give an Al thickness change of 360 ± 10 Å, consistent with the thickness change based on the integration of the recorded current density in Figure 29. Consistency also assures that the electrochemistry is not compromised by the design of the split cell.

The *in situ* experiment on bare Al anode verifies the correlation of NR SLD profiles with the electrochemical response. In chloride-containing aqueous environment, a uniform Faradaic corrosion process was observed near the OCP on a bare Al surface as supported by the recorded corrosion current density and thickness change in the Al layer measured by NR.

5.5.2 *In situ* NR study of TCP passivity

The concept of metastable pitting is useful for understanding TCP passivation against pit initiation.[35-42] Metastable pitting refers to pit initiation/repassivation events that occur below the pitting potential, E_{pit}, where stable pitting occurs. The probability of metastable pitting depends on the corrosion environment, such as the Cl^- in electrolyte and the presence of inhibitors. Although TCP pretreatment forms a passive Cr(III)/Zr(IV) oxide layer, metastable pitting is observed on TCP passivated Al and Al alloys. Metastable pitting occurs in the passive range below E_{pit}, which may no longer be considered as a safe region. Some type of structural or chemical change in the TCP layer must be involved in metastable region that is linked to the susceptibility of pitting failure. Our aim is to validate the passivity of TCP under anodic conditions and determine the response of passive TCP films under metastable pitting conditions.

We observed the evolution of the TCP-covered Al anode exposed to progressively increasing anodic potentials in NaCl-D_2O solution. The DC polarization data in the split liquid cell were measured prior to the *in situ* NR in order to find the OCP (Figure 30). A sequence of NR snapshots revealed the TCP structure at different potentials above the OCP, which occurs at -1.00×10^3 mV. Each potential was applied for 1 hour. Each low-angle snapshot took 20 minutes, which is suitable for observation of film evolution.

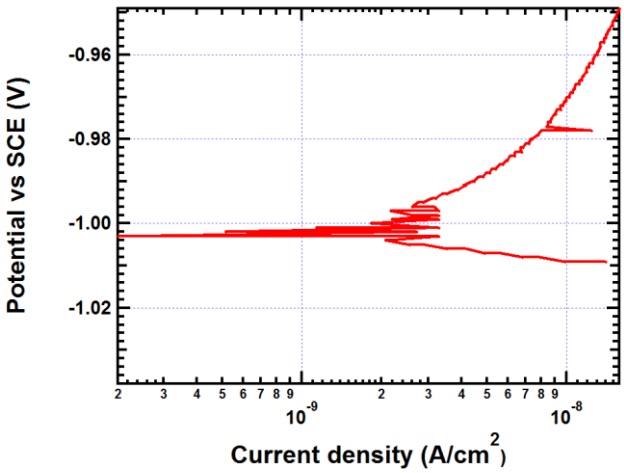

Figure 30. Dynamic DC polarization curves from TCP treated Al-coated wafer anode in the split liquid cell. The cell was filled with NaCl-D_2O solution and stabilized for 30 min prior the measurement. The OCP is indicated at -1.00×10^3 mV.

Figure 31 shows a sequence of $R - q$ plots from the TCP-coated sample at different potentials. No significant change was observed during the first 12 hours when potential was below -800 mV (Figure 31(a), red curves), indicating passivity. When the potential was nobler than the pitting potential (E_{pit} = ~ -800 mV), however, the TCP film started to degrade (Figure 31(a), blue).

Eventually the TCP film and entire Al layer dissolved as revealed by the disappearance of NR fringes (Figure 31(a), black).

The structural change in the TCP passive films under anodic conditions is revealed by the SLD profiles in the passive state (Figure 31(b), red) and after the film disrupted (Figure 31(b), black). The red SLD profile in Figure 31(b) shows a stable TCP film between ~ 150 Å and ~ 760 Å. Below 150 Å is the Al layer, whose thickness decreased from ~ 400 Å to ~ 150 Å due to the anodic step of EA-TCP deposition process. When the applied potential is nobler than -800 mV, however, both the TCP layer and the Al layer disappear (black profile), leaving wafer substrate directly exposed to D_2O solution (marked by the sharp SLD drop at 0 Å).

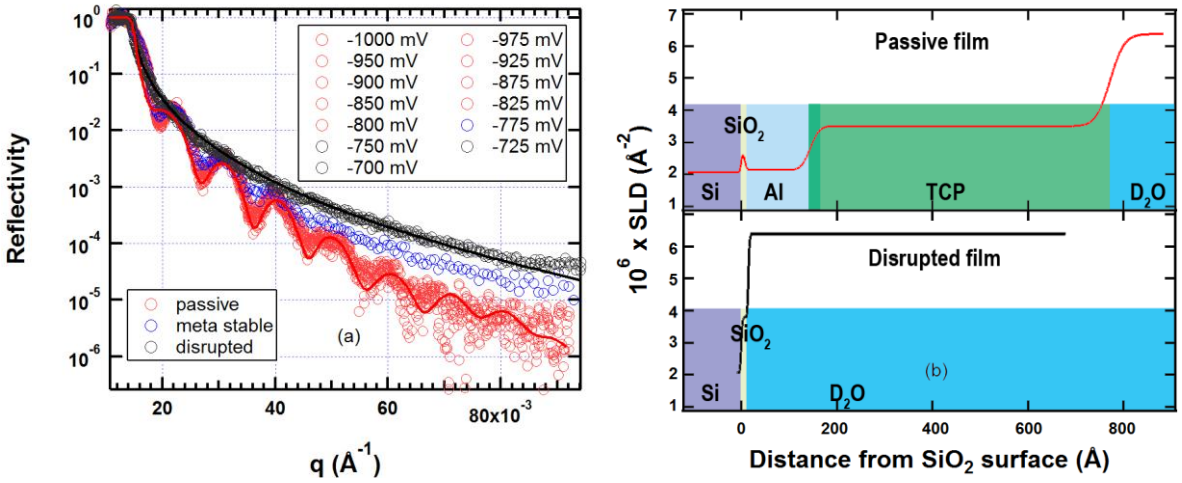

Figure 31. (a) SPEAR NR data ($R - q$ plots) for *in situ* TCP under anodic potentials. Below -800 mV the film is stable. However fringes disappeared after the potential reached -750 mV, indicating TCP coating and Al layer were stripped. (b) SLD profiles based on $R - q$ plots show the disappearance of TCP film as well as the Al layer after the potential exceeded E_{pit}. The position of D_2O solution drops from ~ 760 Å to 0 Å.

These experiments reveal that TCP has a dramatic effect on anodic polarization of Al. The bare metal film uniformly degrades over several hours under slight anodic polarization. With TCP protection, however, the Al layer is stable to an overpotential of +200 mV, above which Al starts to oxidize.

The evolution of current density for the TCP-protected sample shows radically different behavior compared to the bare Al. The protected system shows significant passive character even when applied the potential is +200 mV noble to the OCP.

The measured current density curves during the anodic polarization scan in Figure 31 are plotted in Figure 32(a) (-975 mV to -800 mV) and Figure 32(b) (-975 mV to -725 mV). In Figure 32(a), the measured current density remained below 10 nA / cm^2 at each polarization step. The TCP film effectively protects the underlying Al layer, indicating a passive state. The current density curve at -800 mV (red) however shows some peculiarities. Large "noise" peaks continuously popped up during the 1-hour step. Although the average current declined, these peaks imply some local breakdown in the TCP film that is immediately re-passivated. The cause of re-passivation is not clear. Perhaps Al corrosion product blocks the newly formed ion channels in TCP film. The current density curves for subsequent steps (-775 mV, -750 mV, and -725 mV) are included in Figure 32(b). The current at -775 mV rapidly increased from nA / cm^2 to μA / cm^2. The TCP

film loses its passivity at this potential and Al layer starts to dissolve. At -750 mV and -725 mV dissolution continues until there is no Al left on the silicon wafer.

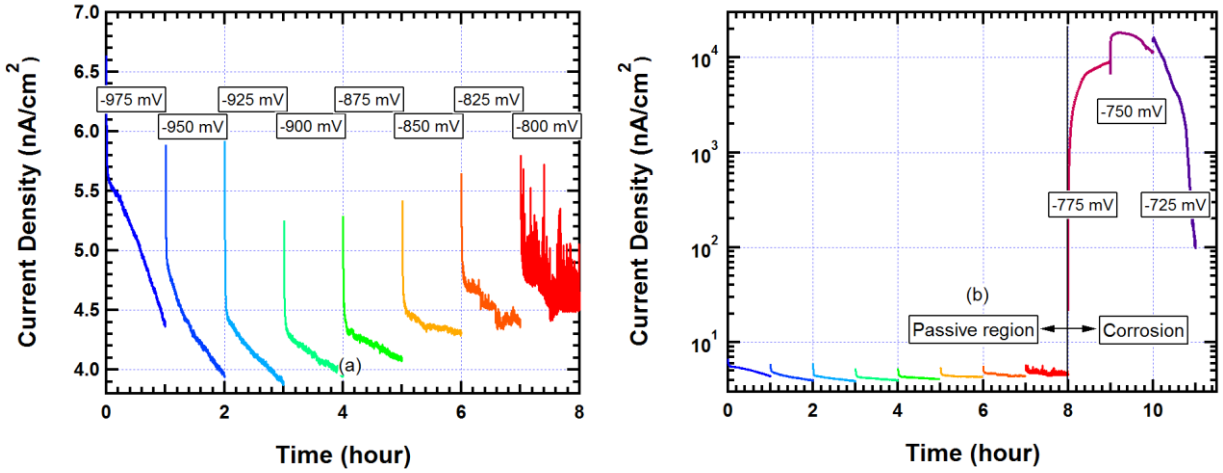

Figure 32**.** Current density curves of a TCP-coated sample after each potential step. (a) Recorded current densities in the passive region (-975 − -800 mV vs. SCE) were under 10 nA / cm^2. The red curve (at -800 mV) showed some instability, as indicated by the noise peaks. (b) The current density for potentials more noble than -775 mV jumped to μA / cm^2 scale, but eventually dropped back after the Al dissolved, leaving a bare silicon wafer. The curve at -725 mV illustrates this behavior within the time window of the experiment.

The passive film structure and failure mechanism in a pitting scenario are revealed by analysis of the NR data in Figure 31 for TCP-protected Al-wafer. When in passive range (below -800 mV), the TCP film is stable as indicated by the identical red $R - q$ plots in Figure 31(a) and SLD profile in Figure 31(b). The thickness of the Al layer did not change during these steps. Above the -800 mV TCP no longer suppresses the dissolution of Al layer. The entire system (Al and TCP) strips, leaving the oxide-covered silicon substrate directly in contact with the D_2O electrolyte. The metastable state (-775 mV) will be discussed later after we examine the water content of the TCP layer in the passive state.

To quantify the D_2O penetration into in the passive TCP film, we compared the SLD profile of the TCP film before and after D_2O exposure (Figure 33) below -800 mV. The SLD profile of the dry sample shows that a thin, dense interfacial layer exists between the metal and the bulk TCP film. In the wet state, this layer is masked in the high SLD wet film. We determined the composition of the bulk film in the dry state previously (Section 5.4.3) by a combination of neutron reflectivity and x-ray reflectivity: $Cr_2O_3{\cdot}iH_2O{\cdot}x(ZrO_2{\cdot}jH_2O)$ (i= 2.10 ± 0.55, j = 1.60 ± 0.45 and x = 0.85 ± 0.14).[43]

Comparing the SLD profiles of TCP films in the room-temperature dried state (Figure 33, blue curve), and in the split liquid cell (Figure 33, red curve), the SLD of the TCP film increases from 1.98 ± 0.06 × 10^{-6} Å^{-2} to 3.6 ± 0.1 × 10^{-6} Å^{-2}, while the thickness did not change significantly. The SLD increase can be explained by exchange of D_2O for the H_2O in Cr and Zr oxide hydrates that constitute the TCP film.

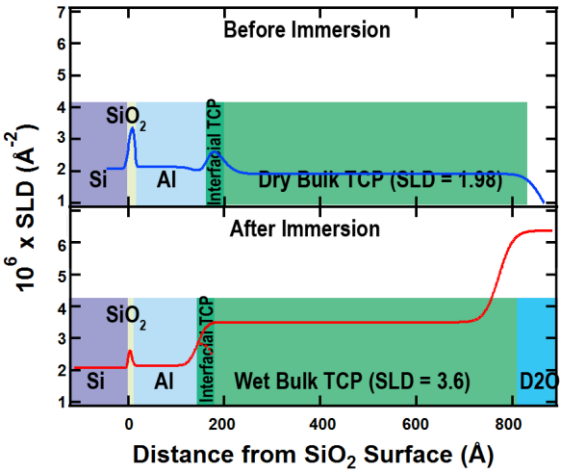

Figure 33. SLD profiles of RT-dried TCP samples before polarization (blue curve).[43] A dense interfacial TCP layer is observed between the bulk TCP film and Al. The SLD profile after exposure is plotted for comparison. The dense interfacial layer still exists in the wet state but is overwhelmed by the bulk TCP layer, which has higher SLD.

The molecular fraction, *f*, converted from hydrate to deuterate is calculated as:

$$\frac{3.6 \times 10^{-6}\text{Å}^{-2}}{1.98 \times 10^{-6}\text{Å}^{-2}} = \frac{b_{\text{Cr2O3}\cdot x\text{ZrO2}\cdot(i+xj)((1-f)\text{H2O}+f\text{D2O})}}{b_{\text{Cr2O3}\cdot x\text{ZrO2}\cdot(i+xj)\text{H2O}}} \tag{29}$$

where $i = 2.10 \pm 0.55$, $j = 1.60 \pm 0.45$ and $x = 0.85 \pm 0.14$.[43]

Given the neutron scattering lengths of the relevant compounds:

$$b_{Cr2O3} = 2.46 \times 10^{-4}\text{Å} \tag{30}$$

$$b_{\text{ZrO2}} = 1.876 \times 10^{-4}\text{Å} \tag{31}$$

$$b_{\text{H2O}} = -0.167 \times 10^{-4}\text{Å} \tag{32}$$

$$b_{\text{D2O}} = 1.915 \times 10^{-4}\text{Å} \tag{33}$$

Equation 29 yields $f = 40 \pm 5\%$, which means 40% of H_2O molecules in the Cr(III)/Zr(IV) oxide hydrate is exchanged, while the TCP film remains protective. This result shows that the bulk TCP film is not chemically inert when exposed to an aqueous environment, although it remains passive. Water molecules from the salt solution penetrate the bulk TCP layer by replacing the original water of hydration.

TCP passivity is attributed to the suppression of NaCl-D_2O solution penetration, hence acting as barrier against ion transport. Since the TCP bulk film retains its original dry-state structure with

no swelling, the Cr_2O_3/ZrO_2 matrix is not altered by exchange of hydrate water. If bulk salt solution penetrated the film it would swell. In the absence of such swelling, transport of Na^+, Cl^- and Al^{3+} is suppressed, as there is no bulk water to stabilize these ions. Suppression of ionic transport precludes Al dissolution. In addition, the dense interfacial layer is immune to both deuterate-hydrate exchange and bulk water penetration, so this layer also blocks ion transport.

Failure of the TCP film is attributed to penetration of bulk salt solution, which facilitates ion transport. Evidence for this failure mechanism comes from examination of the NR data in the metastable state at -775 mV. According electrochemical data (Figure 32) the TCP film loses protective character at this potential.

The $R - q$ plot in the metastable state is shown in Figure 34(a). Figure 34(b) compares the SLD profiles in the passive, metastable and failed states. In the metastable state the Al layer thins while the TCP film swells significantly, as indicated by both increased thickness and higher SLD. Compared to passive state the SLD increases from $3.6 \pm 0.1 \times 10^{-6}$ Å^{-2} to $5.7 \pm 0.1 \times 10^{-6}$ Å^{-2}. The higher SLD can be explained by complete conversion of crystal hydrate water plus physical invasion of bulk salt solution.

Given the SLD of D_2O (6.37×10^{-6} Å^{-2}), and $\mathrm{SLD}_{\mathrm{swollen\ TCP}}$ (5.7×10^{-6} Å^{-2}), the volume fraction, ϕ, occupied by NaCl-D_2O bulk solution in the metastable film can be estimated if we assume complete exchange of crystal hydration water plus penetration of bulk D_2O:

$$\mathrm{SLD}_{\mathrm{swollen\ TCP}} = (1-\phi)\mathrm{SLD}_{(\mathrm{Cr2O3}\cdot i\mathrm{D2O}\cdot x(\mathrm{ZrO2}\cdot j\mathrm{D2O}))} + \phi \times \mathrm{SLD}_{\mathrm{D2O}} \tag{34}$$

where $\mathrm{SLD}_{\mathrm{Cr2O3}\cdot i\mathrm{D2O}\cdot x(\mathrm{ZrO2}\cdot j\mathrm{D2O})}$ can be calculated from the known scattering lengths.

$$\frac{\mathrm{SLD}_{\mathrm{Cr2O3}\cdot i\mathrm{D2O}\cdot x(\mathrm{ZrO2}\cdot j\mathrm{D2O})}}{\mathrm{SLD}_{\mathrm{Cr2O3}\cdot i\mathrm{H2O}\cdot x(\mathrm{ZrO2}\cdot j\mathrm{H2O})}} = \frac{b_{\mathrm{Cr2O3}\cdot i\mathrm{D2O}\cdot x(\mathrm{ZrO2}\cdot j\mathrm{D2O})}}{b_{\mathrm{Cr2O3}\cdot i\mathrm{H2O}\cdot x(\mathrm{ZrO2}\cdot j\mathrm{H2O})}} \tag{35}$$

Substitution yields:

$$\phi = \frac{5.7 \times 10^{-6}\text{Å}^{-2} - 4.84 \times 10^{-6}\text{Å}^{-2}}{6.37 \times 10^{-6}\text{Å}^{-2} - 4.84 \times 10^{-6}\text{Å}^{-2}} = 50 \pm 10 \text{ vol\%} \tag{36}$$

The chloride-containing aqueous phase occupies approximately 50 vol% of the swollen TCP film. Both bulk and interfacial TCP layers are penetrated by salt solution. The aqueous environment now directly contacts the Al. Both Cl^- and Al^{3+} ions diffuse through the film. The entire passivation system fails and Al oxidizes as indicated by the recorded current density curves (Figure 32(b)).

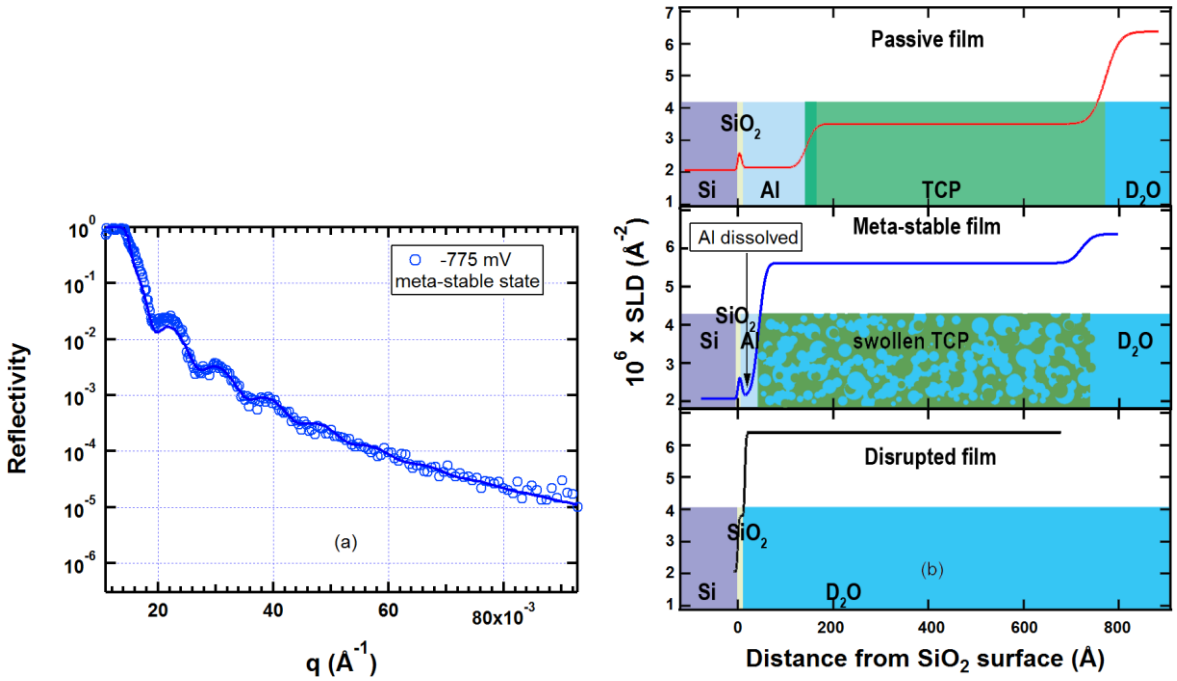

Figure 34. (a) SPEAR NR data (R − q plots) for the metastable state at -775 mV. (b) SLD profiles of the metastable state compared to the passive and failed states. In the metastable state the Al layer dissolves and TCP film swells. The SLD of the TCP layer is 5.7 ± 0.1 × 10^{-6} Å^{-2} and the thickness is 690 ± 20 Å.

5.5.3 Summary of TCP passivity

As a summary of the *in situ* TCP passivity study, a stable TCP structure is observed by NR when the film remains protective in a chloride-containing aqueous environment. However based on SLD profiles of the TCP film under stable conditions, approximately 40% of the solid hydrate water in the bulk TCP layer is exchangeable when exposed to an aqueous environment. In spite of exchange of hydration water, the Cr_2O_3/ZrO_2 matrix retains its original dry-state structure with no swelling. In the absence of bulk solution in the film, transport of Na^+, Cl^- and Al^{3+} is suppressed and the underlying aluminum remains fully protected. Passivity is attributed to suppression of ion transport by both the bulk and interfacial layers.

When the potential reaches pitting potential, the TCP film swells and loses passivity. The underlying aluminum dissolves as indicated by the current density in the μA/cm^2 range. The TCP film swells, but does not dissolve. In this swollen state the chloride-containing aqueous phase penetrates the entire TCP film including the dense layer at the metal interface. Ion transport is no longer suppressed so the aluminum under the swollen TCP film oxidizes. The TCP film itself disappears with a 25 mV increase in applied potential. When the compromised TCP film remains on the Al, the isolated microenvironment under the film is conducive to pitting.

5.6 Step-by-step anodic hardening by Ce(III)

5.6.1 Anodic hardening process

In spite of its robust passive nature low pitting resistance is a weakness of the TCP system. Stable pitting is coincident with water penetration and swelling of the TCP film, [21] although the TCP layer remains above the Al when pits stabilize and propagate (Section 5.5.2).[21, 43] Recent research has been focused on improving the pitting resistance by adding non-chromate inhibitors.[19, 31, 44-48]

It has been reported that the addition of Ce(III) enhances TCP systems against pitting on Al alloys.[49] Due to the fact that Ce(III) has both anodic[16-19] and cathodic[20] inhibition character, conventional electrochemical methods on Al alloys may be compromised by the intermingled intermetallic structure on alloy surface, resulting in contradictory data depending on electrochemical history. As discussed below (Figure 37**)**, for example, the open circuit potential (OCP) shifts in opposite directions: 1) after step-by-step anodic hardening in Ce(III) (green), implying anodic inhibition and 2) after simple immersion in Ce(III) (orange), which implies a strong cathodic inhibition effect.

Both Ce(III)-based and Ce(IV)-based inhibitor systems are reported to have active protection properties.[20, 48, 50-52] To obtain Ce(IV) in aqueous solution, however, requires a strong oxidizing agent such as hydrogen peroxide.

$$2Ce^{3+} + H_2O_2 + 2H^+ \rightarrow 2Ce^{4+} + 2H_2O$$

Because the effect of H_2O_2 on the EA-TCP film is unknown, we selected Ce(III). In the step-by-step experiment therefore we are studying the healing effect under anodic conditions by Ce(III) in the absence of Ce(IV).

We demonstrate a straightforward step-by-step approach to improve the pitting resistance of EA-TCP films in the presence of Ce^{3+}. In addition, dynamic DC polarization diagrams are compared to evaluate the corrosion protection of coatings with and without cerium ions present in solution.

In the step-by-step approach the applied potential was held for 1 or 2 hours at each step (Figure 35). The first step was at -740 mV, 20 mV higher than the original OCP. During subsequent 1-hour steps at -720 mV and -700 mV, the current density was not stable, fluctuating above and below 0 V. When the potential was further raised, current density gradually stabilized between 0 and 200 nA/cm^2. Some samples stabilized at values below 10 nA/cm^2, including the one in Figure 35. At -590 mV the current started to increase but decayed back after 1.5 hour. At -580 mV current density jumped to mA/cm^2 scale, implying that the passive film had failed. The limit for Ce(III) inhibition, -580 mV, was repeatedly confirmed with different samples.

The measured current density was nearly independent of potential and remained below 100 nA/cm^2 until the potential reached -580 mV. As pits continuously initiate and re-passivate, the surface condition of the EA-TCP film gradually improves. This initiation and re-passivation process makes the EA-TCP film more resistant to anodic reactions. Both current arrest and decreasing baseline indicate active Ce(III) inhibition.

The step-by-step experiment was also carried out on an EA-TCP passivated AA2024-T3 in the absence of Ce^{3+} as shown in Figure 36. These samples showed increasing in current density at all

potentials similar to a slowly corroding specimen. Note that the currents are 500 times larger in Figure 36 compared to Figure 35. Step-by-step testing on an uncoated control sample was also attempted. No significant inhibition effect was observed. Without an EA-TCP film the current was unstable.

In order to obtain DC polarization curves on the Ce(III)-inhibited EA-TCP sample, EA-TCP samples were step-by-step anodically polarized but stopped at -580 mV, just prior to breakdown. At this point dynamic DC polarization curves (anodic and cathodic branches) were measured from the new OCP. The two current branches were measured separately on different EA-TCP samples. The OCP of Ce(III)-inhibited EA-TCP sample increased to -680 ± 10 mV and the passive current density of anodic part dropped one-decade compared to the uninhibited sample. Cathodic current branch also decreased somewhat. E_{pit} also increased after Ce(III) inhibition. The improvement is significant in that: 1) OCP shifted +100 mV noble for the -1.50 V EA-TCP sample, 2) the anodic current density decreased by a factor of ten and 3) E_{pit} increased by 50 mV.

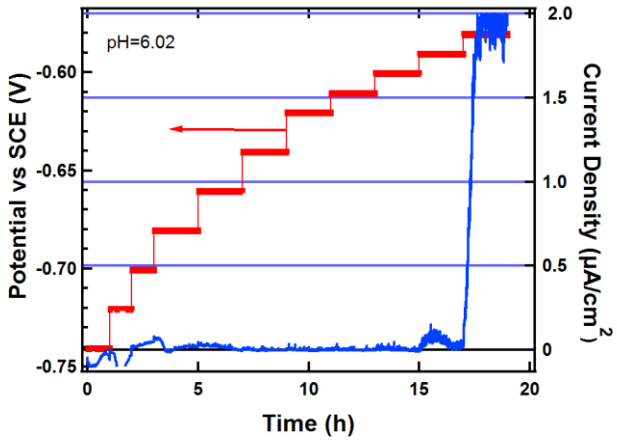

Figure 35**.** Step-by-step anodic polarization of an EA-TCP coated AA2024-T3 in 1 wt% NaCl with 0.1 wt% $CeCl_3$ de-aerated aqueous solution (blue line). Left axis is applied potential (red curve). The right axis is the current density (blue curves).

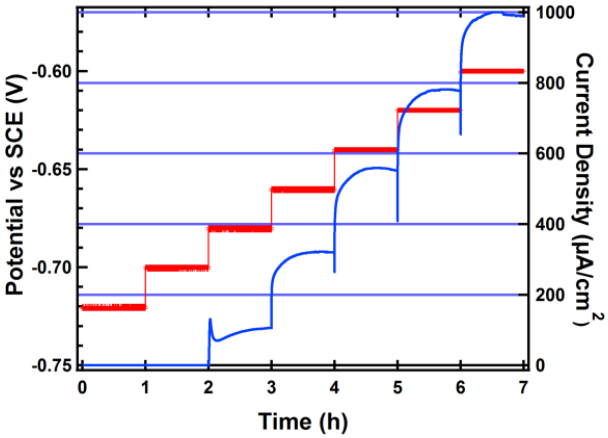

Figure 36. The step-by-step polarization data for EA-TCP coated AA2024-T3 in 1% NaCl solution without Ce^{3+}. The current density reaches 0.1 mA/cm^2 in third step -680 mV, indicating failure. Note that the current density is 500 times greater than in Figure 35.

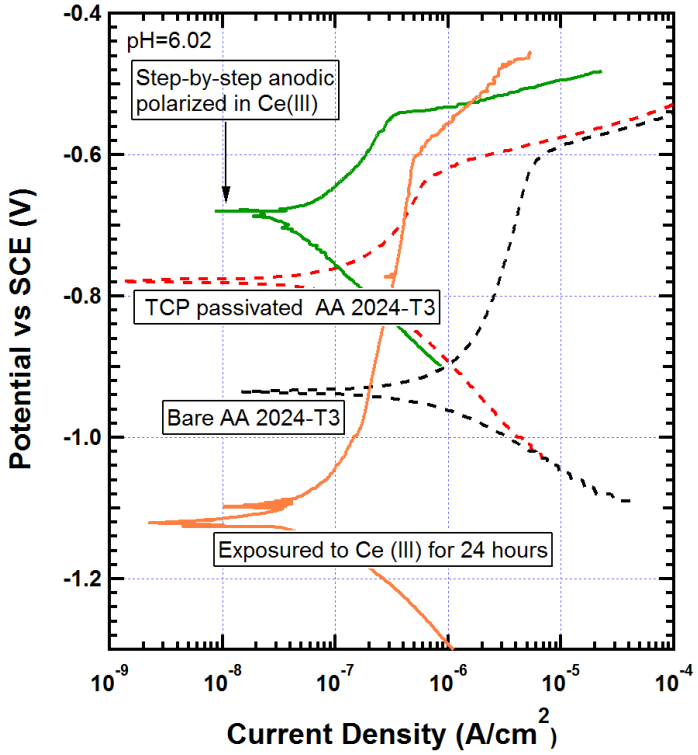

Figure 37. DC polarization curves of AA2024-T3 coupons with and without TCP protection and Ce(III) inhibition. The green curve measured after step-by-step anodic polarization in Ce(III) shows an increased OCP, while the orange curve measured after 24-hour immersion in Ce(III) shows a decreased OCP compared to the bare AA2024-T3 alloy (black), and TCP-passivated AA2024-T3 (red) without Ce(III) inhibition. Except for the bare alloy, all specimens were TCP-coated AA2024-T3 coupons.

5.6.2 Effect of pH

The pH of the Ce(III) inhibition solution in Figure 37 was measured to be 6.02. In order to probe the pH limits of Ce^{3+} step-by-step inhibition, we performed experiments at pH = 7.97 (Figure 38) and pH = 4.03 (Figure 39). Both tests show a limit at -580 mV. That is, the limiting potential for Ce (III) step-by-step inhibition is pH independent in the range from 4 to 8.

5.7 *In situ* evolution of TCP film on Al under Ce(III) anodic hardening

This section is devoted to exploring morphological evolution of TCP films under anodic conditions. Ce(III) cathodic inhibition will be discussed in Section 5.8. Understanding the evolution of the TCP film under Ce(III) anodic hardening requires a well-defined TCP-passivated Al anode for step-by-step polarization so the evolution of the TCP film can be interrogated by NR. The step-by-step anodic hardening method is described in Section 4.9 and below.

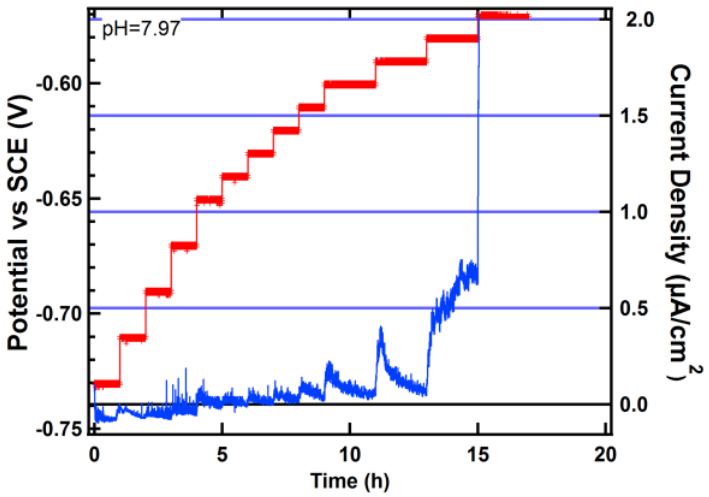

Figure 38. Step-by-step anodic polarization of -1.50 V EA-TCP coated AA2024-T3 in 1 wt% NaCl and 0.1 wt% $CeCl_3$ de-aerated aqueous solution. The pH was adjusted to 7.97. The short-term and long-term passivation effects are apparent between 7 and 13 h.

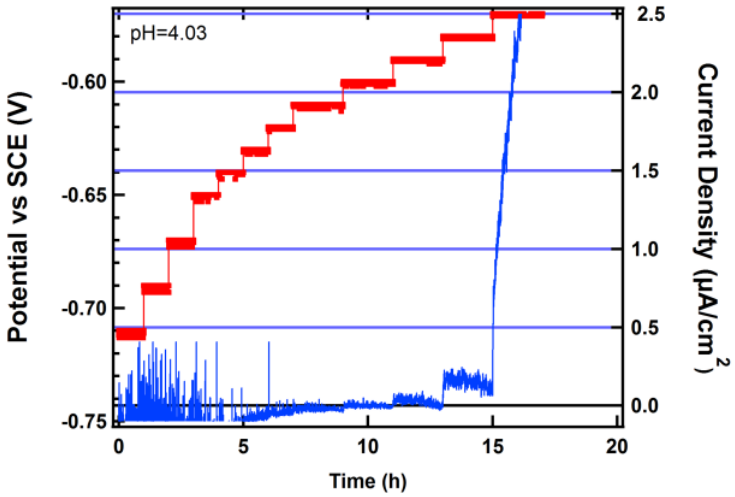

Figure 39. Step-by-step anodic polarization of -1.50 V EA-TCP coated AA2024-T3 in 1 wt% NaCl and 0.1 wt% $CeCl_3$ de-aerated aqueous solution. The pH was adjusted to 4.03.

5.7.1 *In situ* NR of Ce(III) anodic hardening pure Al

The Ce(III) anodic hardening experiment on TCP-passivated AA2024-T3 alloy (Section 5.6) indicates improved pitting resistance compared to the results in un-inhibited NaCl electrolyte.[21] In Figure 40 the current density curves for TCP passivated pure Al at a sequence of constant anodic potentials are compared to the system without Ce(III). Both curves show a corrosion current < 10 nA/cm^2, indicating a passive state. The passive range of Ce(III)-inhibited TCP, however, is expanded to nobler potentials (-800 mV to -750 mV), followed by a transition stage at -725 mV, where current rises to ~100 nA/cm^2. The current baseline in the passive state is also substantially lower than the un-inhibited case. These observations imply anodic inhibition following step-by-step polarization in the presence of Ce(III). We refer to this effect as "anodic hardening."

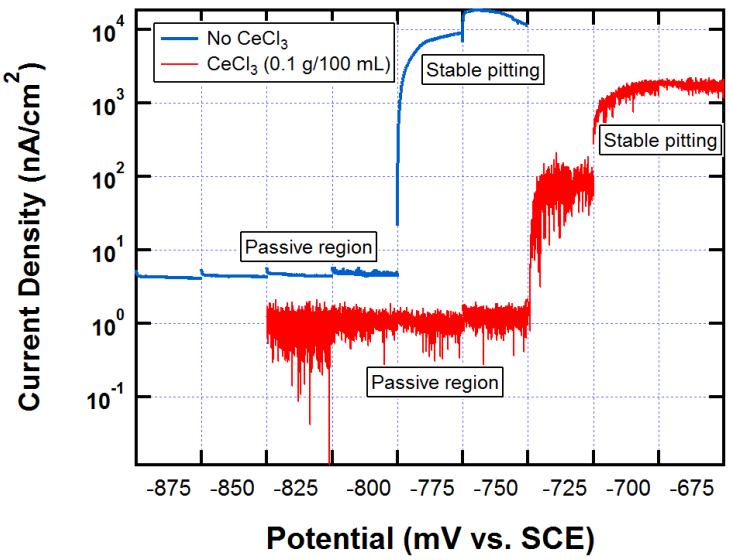

Figure 40. Step-by-step potentiostatic scan of a TCP-passivated pure Al anode in 0.1 wt% $CeCl_3$-inhibited 1-wt% NaCl-D_2O solution (red), compared to the case without Ce(III) (blue). The passive region of the TCP-passivated Al anode extends to higher potentials with a lower current baseline during Ce(III) inhibition. A transition region at -725 mV is observed prior to the stable pitting above -700 mV. The counter electrode was a Au-coated wafer. The uninhibited data are from *in situ* work described in Section 5.5.1.[21]

For the inhibited coupon at the transition potential of -725 mV the baseline increases to ~ 100 nA/cm^2, but the film remains passive. Even in the stable pitting regime at -675 mV there is modest passivation with current density reaching only ~ 1 μA/cm^2.

NR snapshots and corresponding SLD profiles of the Ce(III) inhibited system at -825, -800, -775, -750 and -725 mV are displayed in Figure 41. The sample in the cell was exposed to the solution for 30 minutes, resulting in a stable OCP (~ -850 mV) before the step-by-step polarization was started. The snapshot at -825 mV was finished 45 minutes after the initial polarization. The NR snapshots and SLD profiles between – 825 mV and -750 mV are essentially identical. A small change at high q is observed in the -725 mV scan.

The distribution of Ce(III) species in TCP film changes little after initial penetration. The plateau with an SLD = (7.5 ± 0.1) x 10^{-6} indicates that Ce(III) is enriched at the film/solution interface. For comparison, Figure 41(b) also shows the SLD profile for the dry state before polarization and the profile for the uninhibited state in 1 wt% NaCl solution and polarized at a potential within passive region (from -900 mV to -800 mV). These data are taken from Figure 33.

The SLD profile shows that D_2O and $Ce(OD)_3$ have fully penetrated the TCP film by 1 hour and that further polarization has minimal impact on the film morphology. The $Ce(OD)_3$ species is indicated because of its large scattering length, which is required to explain the observation that the film SLD is larger than D_2O. The film thickness does not change significantly, so the amount of Ce(III) in the TCP structure can be estimated from the increase in the SLD from the passive green curve to the Ce(III) enriched state in Figure 41, as is done below.

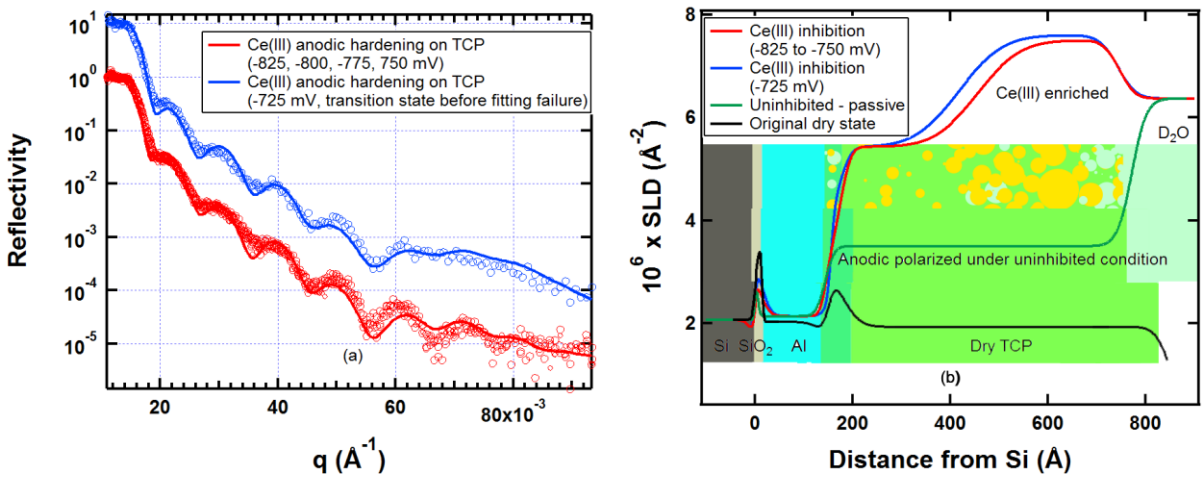

Figure 41. SPEAR NR data ($R-q$ plots, and SLD profiles) for *in situ* evolution of TCP-coated pure Al exposed to step-by-step anodic polarization (-825 mV to -725 mV) in Ce(III)-inhibited NaCl solution (0.1 g $CeCl_3$, 1 g NaCl in 100 ml D_2O, de-aerated). a) $R-q$ plots below -725 mV are identical; b) a small change in higher q range was observed at the transition potential of -725. c) SLD profiles indicate significant Ce(III) distribution within the TCP layer, compared to the original dry TCP (black), and the TCP film under anodic polarization in passive region (-900 mV to -800 mV) without Ce(III) inhibition (green), which is corresponds to the blue current profile in the passive region in Figure 40. The difference in SLD between the uninhibited and inhibited curves is attributed to Ce penetration. Details regarding the uninhibited TCP data can be found in Section 5.5.[21]

5.7.2 The content of Ce(III) in TCP film

SLD profiles of Ce(III)-inhibited TCP (Figure 41) indicate a distribution of Ce species within the bulk TCP layer. The distribution is not uniform, as the SLD value measured near the sample surface is $(7.5 \pm 0.1) \times 10^{-6}$ Å^{-2}, compared to $(5.5 \pm 0.1) \times 10^{-6}$ Å^{-2} close to TCP/Al interface. The concentration of Ce species in the inhibited TCP layer can be estimated from these values.

The first analysis is based on the observed SLD value of the Ce(III) inhibited TCP layer and the assumption that the content of D_2O, H_2O, Cr and Zr in the TCP layer does not change with potential. The SLD value of the Ce(III) inhibited TCP layer can then be expressed as the sum of the SLD of the D_2O-penetrated TCP (as discussed elsewhere[21] and in Section 5.5) and the SLD due to the content of the relevant Ce(III) compound (Equation 37). The SLD value of water-penetrated TCP ($SLD_{D2O\text{-bulk film}}$) is obtained from the red curve in Figure 33(b). The Ce species is assumed to be $Ce(OD)_3$ of unknown density.

$$SLD_{\text{total}} = SLD_{\text{D2O}-\text{bulk film}} + \rho_{\text{Ce(OD)3}}\, b_{\text{Ce(OD)3}} \tag{37}$$

where $SLD_{\text{D2O}-\text{bulk film}} = 3.6 \pm 0.1 \times 10^{-6}$Å^{-2}, and $\rho_{\text{Ce(OD)3}}$ is the molecular number density of $Ce(OD)_3$. At the TCP sample surface, where the SLD_{total} is $7.5 \pm 0.1 \times 10^{-6}$ Å^{-2}, and concentration of Ce is high,

$$SLD_{\text{Ce(OD)3}} = \rho_{\text{Ce(OD)3}}\, b_{\text{Ce(OD)3}} = 3.9 \pm 0.1 \times 10^{-6}\text{Å}^{-2} \tag{38}$$

Close to the TCP/Al interface, where the SLD_{total} is 5.5 $\pm$ 0.1 × 10^{-6} $Å^{-2}$ content of $Ce(OD)_3$ is less

$$SLD_{\mathrm{Ce(OD)3}} = \rho_{\mathrm{Ce(OD)3}}\, b_{\mathrm{Ce(OD)3}} = 1.9 \pm 0.1 \times 10^{-6} Å^{-2} \quad (39)$$

These values are used below to calculate the Cr/Ce ratio.

The major components of the TCP layer are Cr(III) oxide and Zr(IV) oxide. Previous work found[43] the Cr/Zr ratio to be 2:0.85 (Section 5.4.3). We use this ratio to calculate atomic ratio between Cr and Ce to estimate the relative concentration range of Ce(III) in the inhibited TCP film.

The calculated neutron scattering lengths of the relevant compounds,

$$b_{\mathrm{Ce(OD)3}} = 4.226 \times 10^{-4} Å$$

$$b_{\mathrm{Cr2O3}} = 2.46 \times 10^{-4} Å$$

$$b_{\mathrm{ZrO2}} = 1.876 \times 10^{-4} Å$$

$$b_{\mathrm{H2O}} = -0.167 \times 10^{-4} Å$$

$$b_{\mathrm{D2O}} = 1.915 \times 10^{-4} Å$$

The measured SLD of the dry film[43] is, $\mathrm{SLD}_{\mathrm{Dry\ TCP}} = 1.98 \times 10^{-6} Å^{-2}$.

Given the above values, the Cr number density is calculated from the dry data (Equation 40) and the Ce number density is calculated from the $\rho_{\mathrm{Ce(OD)3}}\, b_{\mathrm{Ce(OD)3}}$ (Equation 41)

$$\rho_{\mathrm{Cr}} = 2 \times \frac{\mathrm{SLD}_{\mathrm{dry\ TCP}}}{b_{\mathrm{Cr2O3 \cdot iH2O \cdot x(ZrO2 \cdot jH2O)}}} \quad (40)$$

$$\rho_{\mathrm{Ce(OD)3}} = \frac{SLD_{\mathrm{Ce(OD)3}}}{b_{\mathrm{Ce(OD)3}}} \quad (41)$$

$\rho_{\mathrm{Cr}}/N_{\mathrm{A}} = 1.9 \times 10^{-2} \mathrm{mol/cm^3}$ and $\rho_{\mathrm{Ce(OD)3}}/N_{\mathrm{A}} = 7.5 \times 10^{-3} \sim 1.5 \times 10^{-2} \mathrm{mol/cm^3}$. The two values represent the range of the SLD values in Equations 38 and 39. The atomic ratio of Cr/Ce is estimated to be

$$\mathrm{Cr{:}\,Ce} = \rho_{\mathrm{Cr}}/N_{\mathrm{A}} : \rho_{\mathrm{Ce(OD)3}}/N_{\mathrm{A}} \quad (42)$$

For the upper limit, Cr:Ce = 2:1.6; for the lower limit the ratio is 2:0.8. So the ratio of Cr:Zr:Ce in the TCP bulk layer after Ce(III) anodic hardening (step-by-step polarization from -825 to -725 mV) is expressed as Equation 43.

$$\mathrm{Cr} : \mathrm{Zr} : \mathrm{Ce} = 2 : x : y = 2 : 0.85 \pm 0.14 : 1.2 \pm 0.4 \tag{43}$$

where the error of *y* value for Ce is due to its distribution range in TCP layer from the surface to Al interface; the *x* = 0.85 value is the ratio between Cr and Zr previously measured in the TCP films.[43]

The Cr number density at the original dry film/Al interface is also calculated for comparison.

$$\rho_{\mathrm{Cr-interface}}/N_{\mathrm{A}} = \left(2 \times \frac{\mathrm{SLD_{dry\ interface}}}{b_{\mathrm{Cr2O3 \cdot iH2O \cdot x(ZrO2 \cdot jH2O)}}}\right)\Big/ N_{\mathrm{A}} = 3.5 \pm 0.5 \times 10^{-2}\mathrm{mol/cm^3} \tag{44}$$

The Ce concentration of about $\sim 1 \times 10^{-2}\mathrm{mol/cm^3}$ is comparable to the Cr concentration in the film but three orders of magnitude larger then that in solution, which seems unreasonable. This result implies that the relevant Ce compound has a higher scattering length, perhaps $CeCl_3$ hepta-deuteo-hydrate for which $b = 10.3 \times 10^{-4}$ Å; the SLD of the crystal is 10.3×10^{-6} Å^{-2}.

We also explored a model where Ce(III) exchanges with Cr(III). The exchange model assumes the SLD increase is due to the conversion of TCP film from Cr(III)/Zr(IV) mixture to Ce(III)/Zr(IV). However neutron scattering length of Ce_2O_3 is 2.70×10^{-4} Å, which is close to Cr_2O_3 (2.46×10^{-4} Å). The total SLD of the TCP layer is not sensitive to this conversion.

Based on these calculations, the nature of the Ce inhibited film is uncertain. The unusually high SLD of the Ce penetrated film is hard to justify assuming known cerium compounds. The high SLD is required to fit the critical edge. The critical edge is measured at the low-angle instrument setting where alignment is most critical. These experiments need to be repeated to verify the position of the critical edge.

5.7.3 Inductively coupled plasma (ICP) atomic emission spectroscopy Ce leaching and Cr exchanging

Although the Ce compound in the inhibited film remains uncertain, elemental analysis by inductivity coupled plasma analysis confirms the presence of Ce after anodic hardening. Figure 42 shows atomic concentration of Ce, Cr, Zr in NaCl (1 wt%) water solution over 20 days. Substantial amount of Ce leached out from the anodically hardened TCP alloy, which is reasonable since the NR data indicate a Ce(III) enriched layer after the step-by-step polarization. Cr released from the TCP film with and without anodic hardening is also considerable, while the Zr curve is almost zero. The amount of Cr leached indicates its relative instability compared to Zr in the TCP layer and the possibility of exchange by Ce during anodic hardening. If we include this fact into the previous calculation the content of Ce(III) will be somewhat higher.

The significant amount of Ce(III) is important for understanding Ce(III) anodic hardening. Besides the improved pitting resistance of the anodically hardened TCP film the Ce(III)-enriched layer could serve as a reservoir, which sustains active healing over long term usage in realistic field scenario.

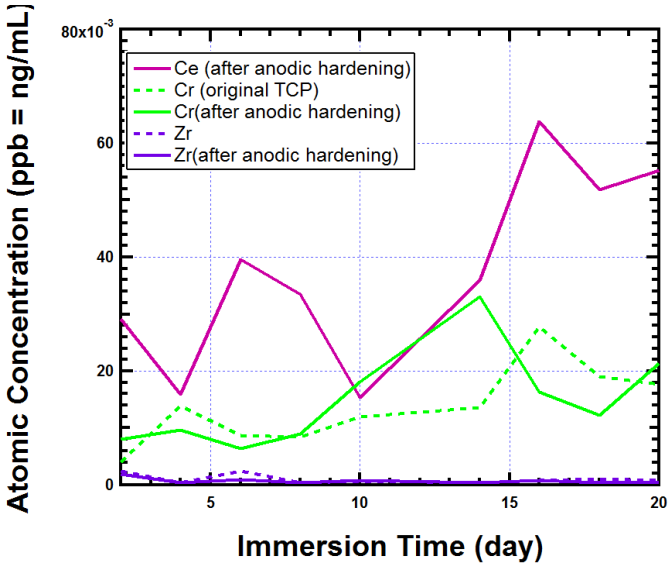

Figure 42. ICP data on the Ce, Cr, Zr atomic concentration in NaCl (1 wt%) water solution. A TCP-passivated AA2024-T3 sample and a TCP-passivated AA2024-T3 sample after Ce(III) anodic hardening were immersed in NaCl (1 wt%) water solution for 20 days. Solution samples were taken every 3 ~ 4 days, to track the concentration of Ce (purple), Cr (green) and Zr (blue) released without hardening (dashes) and after anodic hardening. Substantial amount of Ce is measured. The concentration of Cr from both samples is also considerable, while the Zr leaching is nil.

5.7.4 *In situ* NR of Ce(III) cathodic hardening

Ce(III) cathodic inhibition has also been reported in conjunction with TCP coatings.[20, 47, 50, 52, 53] For example, after simple immersion in Ce(III) the orange DCP data in Figure 37 show that the OCP of the TCP-passivated AA2024-T3 alloy shifts to lower potential, which implies a strong cathodic inhibition effect that is related to passivation of the intermetallic inclusions on the alloy surface.[19, 45, 47] Typically Cu-rich inclusions provide cathodic sites for proton reduction reaction due to its galvanic effect. We chose TCP-passivated pure Al electrode to represent the cathodic sites and generate a similar or even more aggressive cathodic conditions via potentiostatic control. Measuring the evolution of the TCP film under cathodic inhibition in the presence of Ce(III) is the objective of this section.

The split cell configured for cathode interrogation is shown in Figure 2(b). The cell was stabilized for 30 minutes before polarizing the TCP-coated Al anode to -730 mV. This potential results in a transition state condition with current density of +200 nA/cm^2. This transition state is beyond the limit of short-term Ce(III) anodic inhibition; i.e., corrosion current does not decline within one hour. However using the TCP-coated Al cathode, the corrosion current profile over 24 h shows slow attenuation (Figure 43). In this experiment the neutron beam impinged on the TCP-coated Al cathode to detect changes due to Ce(III) inhibition.

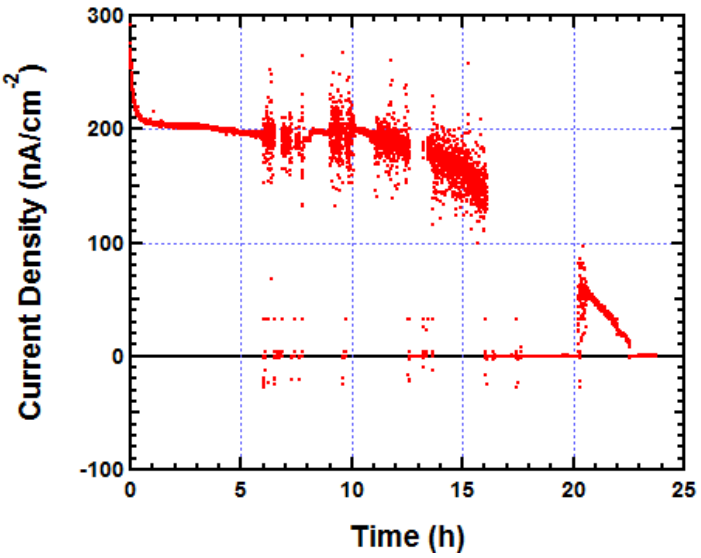

Figure 43. Anodic current density profile when the TCP-coated Al anode was controlled at transition stage at -730 mV. The current drops to 0 at 23 hour. The origin of the noise is uncertain; it may be due to mechanical vibrations, poor electrical connection or metastable pitting.

The NR data (Figure 44) show that the TCP film on the cathode changed continuously during the 24-hour polarization in Ce. Three significant features are found in the SLD profiles (Figure 44(b)): The SLD of the bulk TCP film increases from $(4.4 \pm 0.2) \times 10^{-6}$ Å^{-2} to $(5.7 \pm 0.1) \times 10^{-6}$ Å^{-2} over 24 hours; the bulk film thickness increased from 760 ± 10 Å to 1000 ± 10 Å between hour 12 and hour 24 hour; and a SLD peak formed at the Al/TCP interface after 18 h, when the current density in Figure 43 starts to show a substantial decrease. The initial SLD of the bulk TCP film, $(4.4 \pm 0.2) \times 10^{-6}$ Å^{-2}, is primarily due to H_2O penetration, which leads to oxide hydrate exchange by D_2O. The D_2O/H_2O exchange was described in Section 5.5.[21] The SLD increase from $(4.4 \pm 0.2) \times 10^{-6}$ Å^{-2} to $(5.7 \pm 0.1) \times 10^{-6}$ Å^{-2} during the *in situ* experiment can be partially attributed to the further D_2O/H_2O hydrate exchange, but is dominated by penetration of bulk D_2O electrolyte into the film structure as demonstrated in Section 5.5. Significant swelling occurs after hour 12; the content of water in the swollen structure is consistent with our previous observation on swollen TCP film under anodic polarization without inhibition, which leads us to postulate that it is primarily D_2O solution, not Ce(III) that increases the SLD of the bulk TCP layer to $(5.7 \pm 0.1) \times 10^{-6}$. At hour 15, a SLD peak at 250 Å appears, which is assumed to be an indication of a Ce(III)-enriched interface, as represented by orange species in Figure 44 (c).

During the first 12 hours, no significant inhibition is observed as the anodic current density is constant at ~ 200 nA/cm^2 (Figure 43). After 15 h the current attenuates and drops to 0 after 23 hours. We cannot determine whether Ce(III) cathodic inhibition occurs on the cathode based on the anodic 24-hour *in situ* current density in Figure 43. Although the exchange current is not measured in this experiment, the observed current attenuation is consistent with Ce(III) anodic hardening on the TCP-passivated Al anode, which eventually suppresses the current to zero as the OCP shifts in the noble direction Figure 44(c).

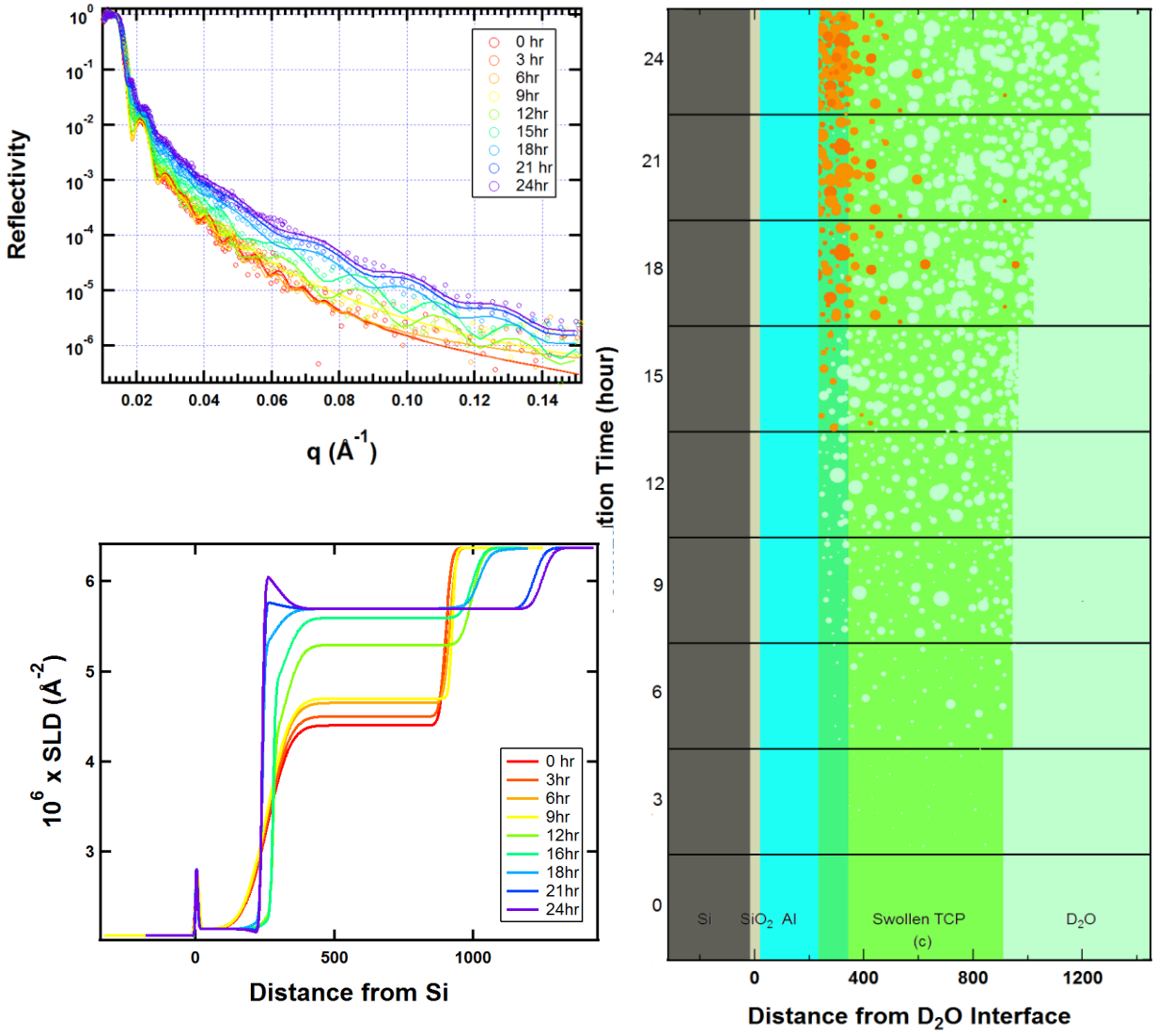

Figure 44. SPEAR NR data R − q plots (a), SLD profiles (b) and layered model as a function of time (c) for *in situ* TCP-coated Al cathode under Ce(III) inhibition during constant polarization of the anode at -730 mV. The evolution of the structure and composition of the TCP bulk layer in the SLD (b) profiles reflect the continuous change as observed in R − q plots (a). A peak at Al/TCP interface forms after 18 hours, at which point the TCP film thickness increased significantly. c) Illustration of the structural and chemical composition evolution in TCP layer showing build of Ce at the metal-film interface.

5.7.5 Current profile of a cathodically polarized TCP-passivated pure Al /Si wafer

It must be emphasized that the current drop in Figure 43 is unrelated to cathodic inhibition since only anodic current is measured. In order to assess cathodic inhibition, and *ex situ* potentiostatic experiment was carried out at UC on a nominally identical TCP-coated Al wafer in the same Ce-NaCl solution (Figure 45). The Gamry PCI4 300 potentiostat was used with a 2-in diameter flat

electrochemical cell and a SCE reference. We used a graphite counter electrode for the *ex situ* potentiostatic experiment.

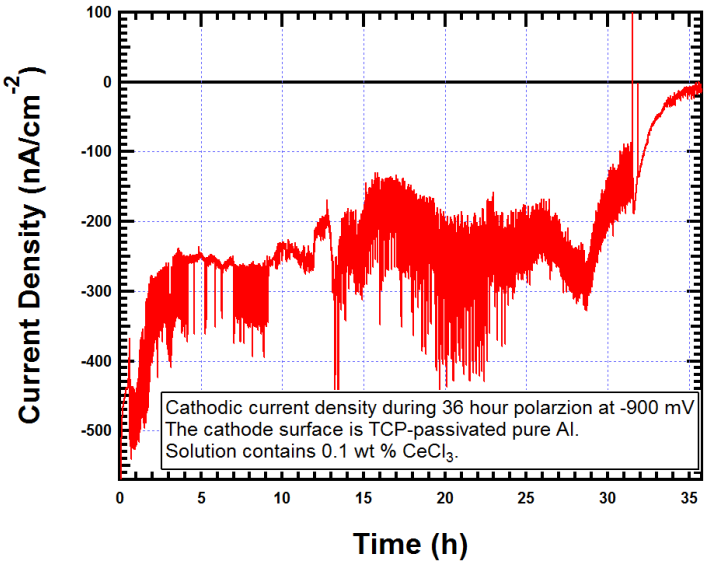

Figure 45. Current density profile at constant cathodic polarization as a function of time. The TCP-coated Al cathode was polarized at -50 mV vs. OCP (-850 mV vs SCE) for 36 hours in de-aerated $CeCl_3$ (0.1 wt%) NaCl (1 wt%) water solution. The current attenuation is an indication of Ce(III) cathodic inhibition.

The OCP of the TCP-passivated Al cathode was measured to be -850 mV vs. SCE after 30 minutes stabilization in the de-aerated $CeCl_3$ (0.1 wt%) NaCl (1 wt%) water solution. The sample was then polarized cathodically to generate a current in the range from ~ −600 to ~ −200 nA/cm^2 (similar to the *in situ* experiment condition). Eventually the constant polarization potential was adjusted to – 50 mV vs. OCP (Figure 45**)**.

Although the transition takes somewhat longer on the cathode (Figure 45) than for the *in situ* experiment (Figure 43), the cathodic current drops to zero within 36 h. When the current reaches zero at 36 h indicating the cathode OCP has shifted -50 mV vs. the original OCP. The shift of the OCP in the active direction is consistent with the OCP shift observed on the alloy in Figure 37, implying cathodic inhibition during the 24 h period when the data in Figure 43 and Figure 44 were measured. It must be emphasized, however, that the current in Figure 45 is not the corrosion exchange current, so we cannot be certain of cathodic inhibition this experiment.

5.7.6 Ce(III) precipitation at Al/TCP interface

Generally Ce(III) precipitation is triggered by the pH increase, which usually occurs on random cathodic sites where the proton reduction reaction occurs. Precipitation of Ce(III) on such sites is assumed to be related to the current drop as observed in Figure 45. We used NR to track the evolution of the TCP-coated Al cathode to verify the content of Ce(III) in the film as evidence supporting the proposed TCP evolution model under cathodic conditions in the presence of Ce(III). NR interrogation of the cathode reveals a SLD peak at the Al/TCP interface between hour 18 and hour 24. Because the SLD value of the Al/TCP interfacial peak exceeds that due to water imbibition, there is a strong implication that $Ce(OD)_3$ is involved since 1) Al dissolution is suppressed; 2) the formation of AlH_3 or AlD_3 requires aggressive conditions; 3) The TCP layer

itself is compromised by proton reduction, and can hardly further densify at the interface; 4) water has reached the maximum content. Additional $Ce(OD)_3$ precipitation at Al/TCP interface is consistent with the currently accepted mechanism for Ce(III) cathodic inhibition.[45, 47, 52] Ce(III) precipitation is accompanied by the additional water, which swells the film, allowing Ce(III) to pass through and reach the high pH region at the TCP/Al interface.[20] The swelling stage triggers Ce(III) to precipitate. This scenario is consistent with the observation that TCP passivated AA2024-T3 exhibits a reduced OCP after 24 hour immersion (orange curve in Figure 37), due to localized cathodic inhibition on noble intermetallic.[19, 46, 47, 52]

The concentration of Ce species in the inhibited TCP layer can be estimated based on the same numerical model used in previous section, which assumes that the content of D_2O, H_2O, Cr and Zr in the TCP layer does not change as the Ce species penetrates the film.

The peak SLD value of the $Ce(OD)_3$ precipitation at Al/TCP interface can then be expressed as the sum of the original SLD of the Al/TCP interface plus the contribution due to the content of the $Ce(OD)_3$, Equation 45.

$$\mathrm{SLD_{peak}} = \mathrm{SLD_{interface}} + \rho_{\mathrm{Ce(OD)3}}\, b_{\mathrm{Ce(OD)3}} \tag{45}$$

where $\rho_{\mathrm{Ce(OD)3}}$ is the molecular number density of $Ce(OD)_3$, and SLD_{peak} is $(6.1 \pm 0.1) \times 10^{-6}$ $Å^{-2}$ (Figure 44(b)).

Since the $SLD_{interface}$ is hard to measure accurately due to the sharp boundary, we estimated the minimum and maximum by taking the value of a virgin interface $(3.6 \pm 0.5) \times 10^{-6}$ $Å^{-2}$ (as measured in Section 5.5), and the value of fully swollen TCP $(5.7 \pm 0.1) \times 10^{-6}$ $Å^{-2}$, as in the bulk layer in Figure 44. The molecular density is calculated via Equation 46.

$$\frac{\rho_{\mathrm{Ce(OD)3}}}{N_{\mathrm{A}}} = 1.5 \times 10^{-3}\mathrm{mol/cm^3} \sim 9.8 \times 10^{-3}\mathrm{mol/cm^3} \tag{46}$$

where N_A is Avogadro number.

This concentration range is very large compared to the Ce(III) concentration in the bulk solution (4×10^{-6} mol/cm^3) but is comparable to the density of Cr in the film (3.5×10^{-2} mol/cm^3), calculated from the formula $Cr_2O_3 \cdot iH_2O \cdot x(ZrO_2 \cdot jH_2O)$ in Section 5.7.

The NR data on both the cathode and anode show very large SLD indicating massive water invasion, but the film remains on the metal. This situation is similar to the situation observed for uninhibited Al in section where the film fails. Further work is required to be sure that Ce inhibition can suppress the corrosion current under such conditions.

5.8 Interface morphology of anodized aluminum

Aluminum anodizing is a standard technique for corrosion protection of aluminum alloys. Anodized aluminum shows unusual structure[54] consisting of two forms of anodic aluminum oxide (AAO), an inner nonporous barrier oxide and an outer porous oxide.[55] The porous structure is typically a self-ordered hexagonal array of cells with cylindrical pores with diameters

of 250 Å to 0.3 µm and depths exceeding 100 µm.[54] The thin barrier layer (100-1000 Å) is found at the bottom of the pores in contact with the metallic Al surface.

XRR and NR have never been used to elucidate the morphology of AAO. Reflectivity is particularly useful to examine the interfacial relationship between dense and porous aluminum oxide. Since NR and XRR require thin films (< 3000 Å), however, conventional anodizing protocols must be modified to achieve thin, smooth AAO films. Part of this research therefore was devoted to exploration of the optimal conditions to produce films suitable for reflectivity. This effort led to a new anodization strategy that could lead to improved oxides on metal other than Al, such as Mg (see section 5.8.4).

5.8.1 Optimum anodizing voltage for AA 2024

The voltage used for common anodizing protocols depends on the acid medium: 15-25 V in 20 wt% sulfuric acid, 60-100 V in 5% phosphoric acid, and 40-60 V in 3% oxalic acid. For thin aluminum films on Si wafers, however, the high local current density during anodizing could dissolve the film before the formation of AAO. An optimum voltage had to be identified for thin film anodizing. We used XRR for these studies since it is available in our laboratory. XRR, however, has the limitation that the oxide layer is not as evident as in NR because the SLDs of the oxide and the metal are similar. Nevertheless, XRR reveals whether the film thickness increases or decreases, which is the key issue in this kinetic study.

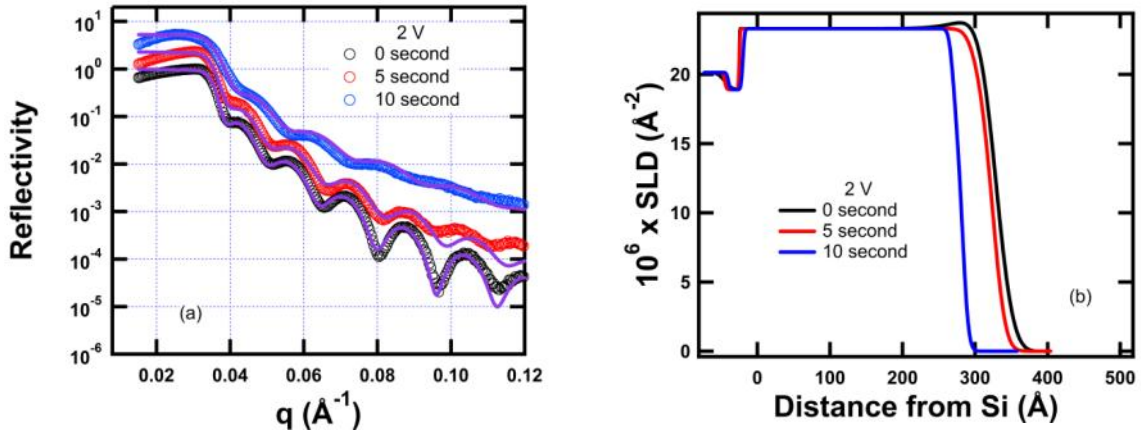

Figure 46 2-V XRR data for AA 2024. The SLD profile shows that the overall film thickness increases by 50 Å in 10 s as the oxide layer forms. A four-layer model is required to fit the 10-s data consistent with complex oxide layer consisting of a thin barrier layer at the metal surface and a porous layer at the air surface.

The optimal voltage was established from the kinetics of AAO film formation at three constant anodizing voltages (2, 5 and 10 V) applied to AA 2024-coated Si wafers. The voltage sweet spot is determined by a balance between oxide formation and dissolution (Figure 46 - Figure 48). If the voltage is too high (10 V), the 400-Å metal coating oxidizes ($Al \rightarrow Al^{3+} + 3e^-$)in 10 s as shown in Figure 48. At 2 V (Figure 46) the oxide forms at the metal surface but dissolves at the solution interface:

$$2Al + 3OH^- \rightarrow Al_2O_3 + 3H^+ + 6e^-$$

$$Al_2O_3 + 6H^+ \rightarrow 2Al^{3+} + 3H_2O$$

which also leads to thinning of the metal without significant oxide growth. At 5 V (Figure 47) continuous oxide growth occurs since the oxide forms at the metal interface faster than it dissolves at the solution interface.

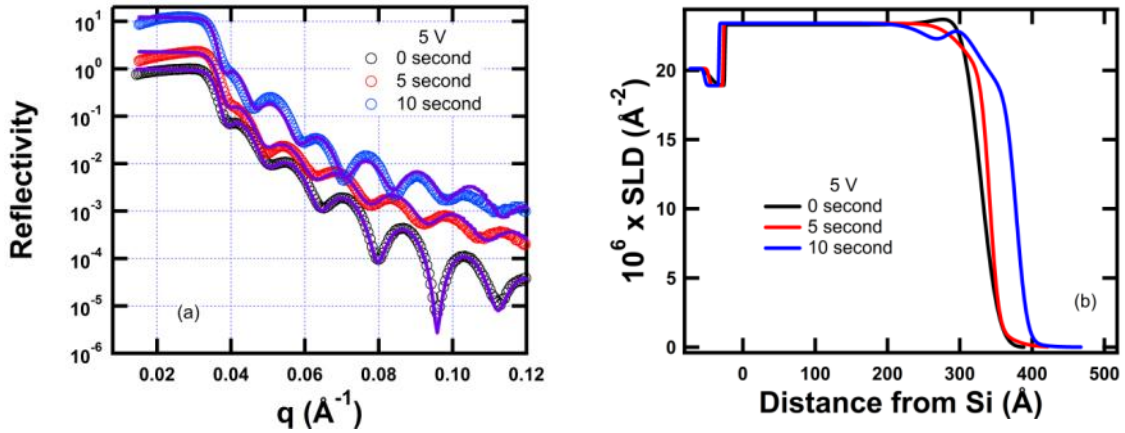

Figure 47. 5-V XRR data for AA 2024. The SLD profile shows that the overall film thickness increases by 50 Å in 10 s as the oxide layer forms. A four-layer model is required to fit the 10-s data consistent with complex oxide layer consisting of a thin barrier layer at the metal surface and a porous layer at the air surface.

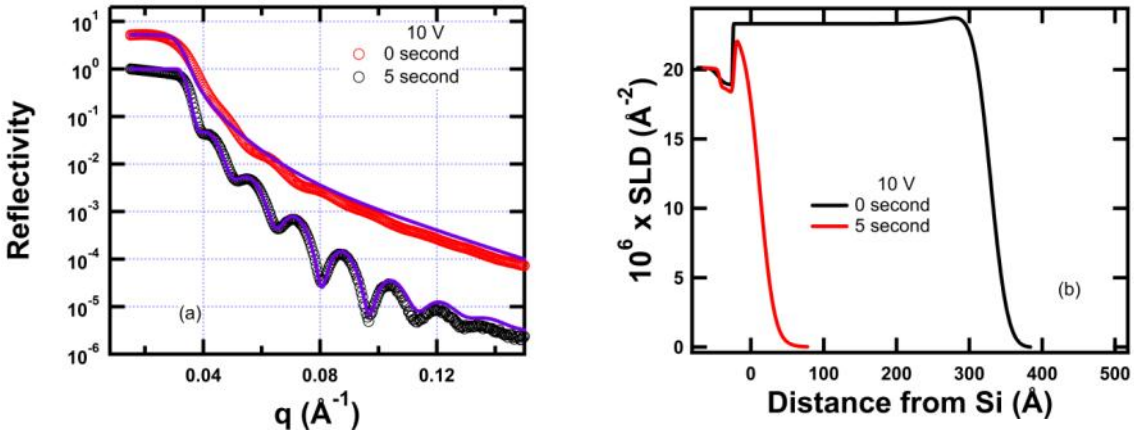

Figure 48. 10-V XRR data for AA 2024. The overall alloy film thickness decreases by 330 Å in 5 s indicating rapid stripping of the metal without significant oxide formation.

We observed that the oxide on AA2024 is unstable and subject to delamination. Additional work below therefore is on pure Al. Using a combination a current limit under voltage control it is possible to achieve sensistive control of the oxide layers on pure Al-coated Si stubstrates.

5.8.2 Optimum anodizing voltage for pure Al

X-ray reflectivity of pure Al-coated samples reveals similar kinetics and mechanisms although the anodized aluminum oxide film for nominally pure Al (AA1100) is more stable so destruction of the film is less likely to occur. As shown in Figure 49 and Figure 50**,** at lower voltages (2 and 5 V), neither 5 nor 10 s anodizing strips the Al layer.

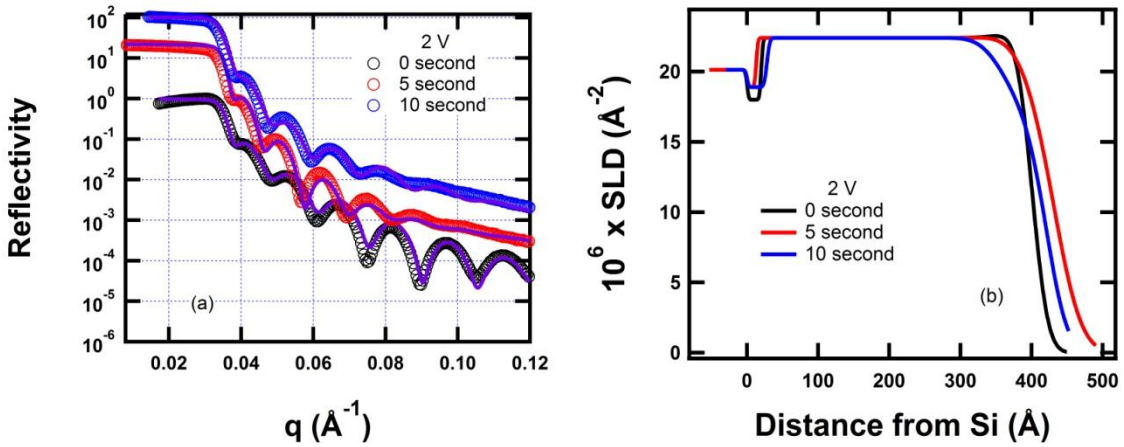

Figure 49. 2-V XRR data for pure aluminum. The SLD profile shows changes at the oxide surface, but minimal reduction of the thickness of the underlying metal**.**

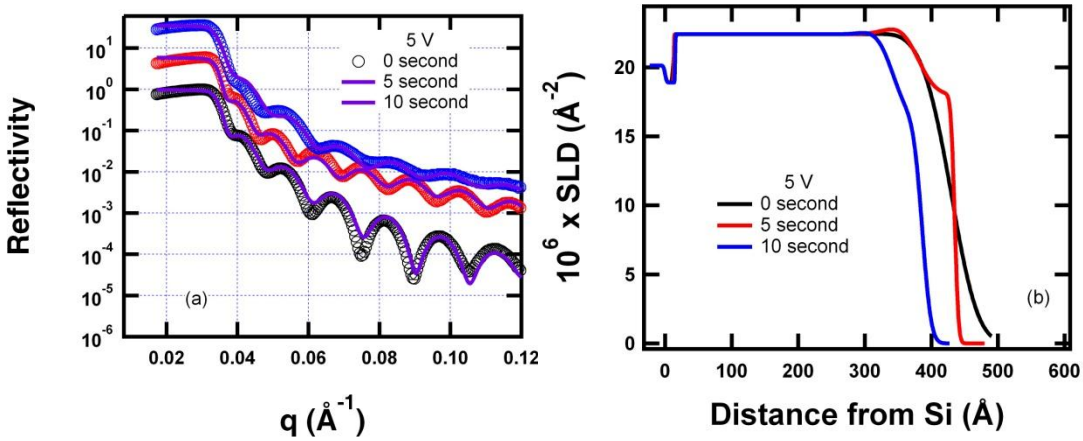

Figure 50. 5-V XRR data for pure aluminum (AA1100). The Al layer decreases quickly by ~80 Å during 10 s anodizing based on the fitting parameters. However, the thickness of the anodic aluminum oxide layer increases by only 40 Å. The anodized film is too thin for the study of interface morphology.

At a higher voltage (5 V, Figure 50) the growth of anodic aluminum oxide is slightly faster than at 2 V. Evidence of a two-layer oxide starts to emerge. Similar to the anodizing of AA2024 the oxide is protective so the film does not strip. At 10 V, however, anodizing strips the Al (Figure 51), similar to the alloy (Figure 48).

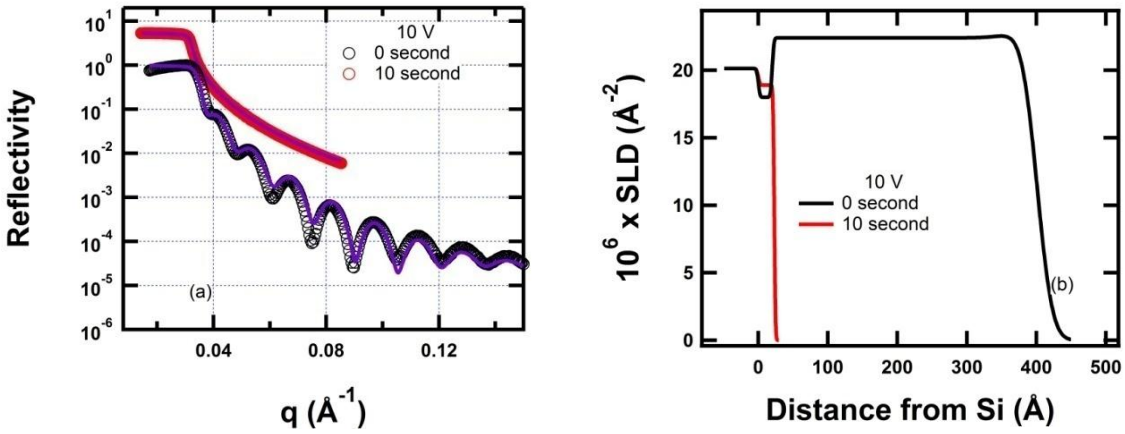

Figure 51. 10-V XRR data for pure Al (AA1100). The film strips in 10 s.

We conclude from these kinetic studies that there is an optimal anodizing voltage for both AA2024 and AA 1100. This optimum voltage balances the formation of metal oxide and the dissolution of oxide. If the voltage is too high (10 V), the film dissolution dominates anodizing for both alloy and pure Al. However AA2024 and pure Al anodizing perform differently at 2 V, where pure Al shows greater stability. We attribute this difference to the fact that the copper content in AA2024 favors oxidation of O^{2-} ions to form oxygen bubbles, which leads to irregular morphology of the porous AAO structure. For thin films in our study, the oxygen evolution can disrupt the film.

Pure Al proved most suitable for anodizing experiments. For pure Al we achieved smooth 3500-Å films, which are ideally suited for NR and XRR experiments (see below).

5.8.3 AAO morphology for AA2024 and pure Al

The kinetic studies above show that distinct AAO films are achieved at 5V in 20 wt% sulfuric acid for anodizing times longer than 10 s. We settled on 30-s to give oxides sufficiently thick to distinguish the two porous layers without completely stripping the underlying metal. Figure 52(a) compares the XRR data for the control sample (400-Å AA2024 on Si wafer) and the anodized sample. The total film thickness increases from 380 to 430 Å due to the formation of the oxide. The derived SLD profile (Figure 52(b)) reveals two oxide layers both of which are quite porous. Assuming the film is pure Al_2O_3 (i.e. unhydrated), the bottom layer is 30-Å thick with a density of 3.0 g cm^{-3} (based on SLD = 24.9×10^{-6} Å^{-2} as shown in Figure 52(b), and SL = 14.0 ×10^{-12}cm for Al_2O_3). The top layer is 145 Å thick with a density of 2.6 g cm^{-3} (SLD = 21.2×10^{-6} Å^{-2}). These densities are both lower than the density of crystalline Al_2O_3 (3.95 g cm^{-3}), implying substantial porosity in both layers (24.0% for bottom, and 34.2% for the top layer). The denser Al_2O_3 layer forms at the metal interface and more porous layer forms at the solution interface as expected from work of others.

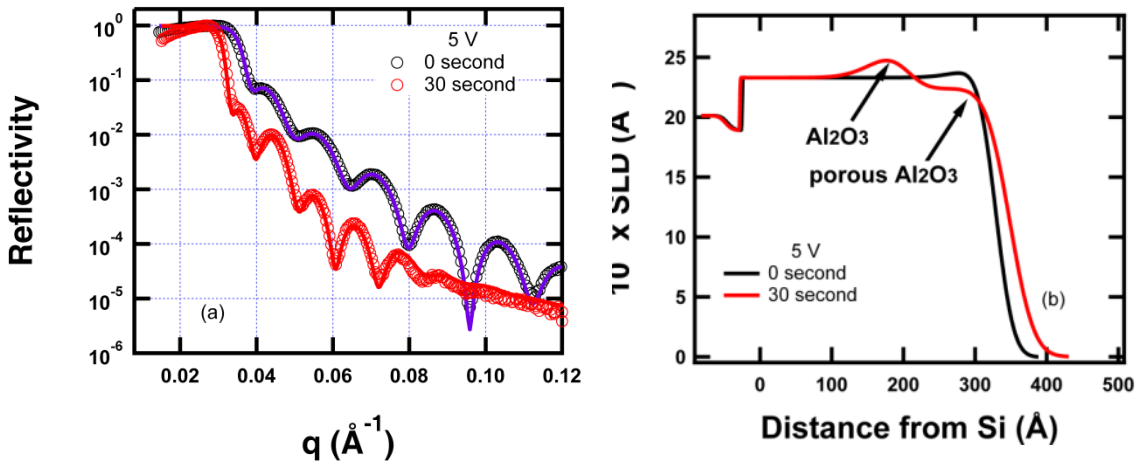

Figure 52. (a) XRR data and (b) SLD profiles of the AA2024 on Si wafers. The anodized sample (anodized in sulfuric acid at 5 V for 30 s) is compared with bare AA 2024. A four-layer (on top of Si) model is required to obtain reasonable agreement with the experimental data. The four layers are SiO_2, Al (density of 2.7 g cm^{-3}), dense Al_2O_3 (density of 3.0 g cm^{-3}), and porous Al_2O_3 (density: 2.6 g cm^{-3}). The densities of the Al_2O_3 are all lower than the density of crystalline Al_2O_3.

For pure Al, we achieved smooth metal films up to 3500-Å thick. We observed well-developed AAO on 3500-Å pure Al anodized for 60 s in 20-wt% H_2SO_4 solution (Figure 53(a)). The SLD profiles (Figure 53(b)) show that there are four layers in the anodized samples (SiO_2, Al (density of 2.7 g cm^{-3}), dense Al_2O_3 (density of 2.8 g cm^{-3}), and porous Al_2O_3 layers (density of 2.4 g cm^{-3})). The 60-s sample exhibits a 1770-Å porous Al_2O_3 layer.

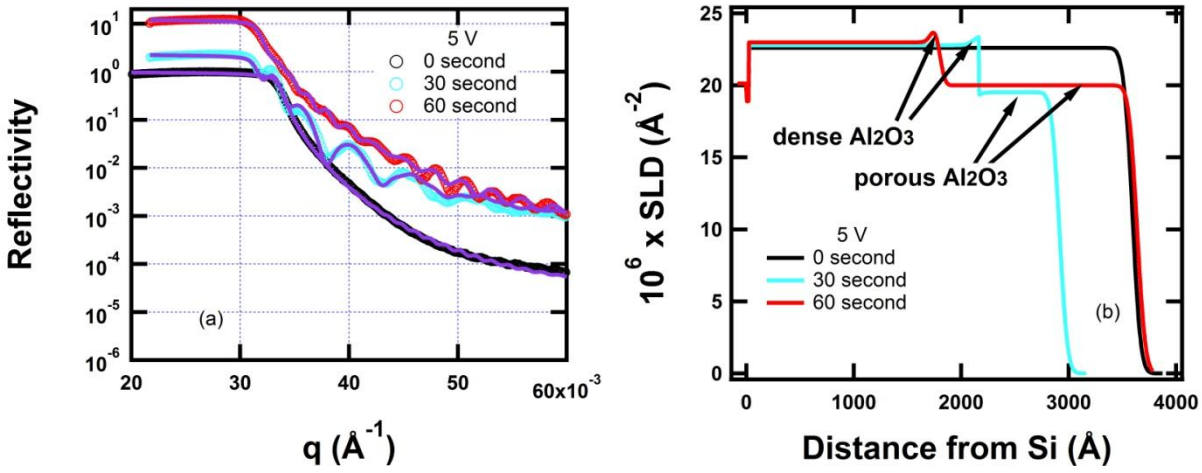

Figure 53. (a) X-ray reflectivity and (b) SLD profiles of the anodized pure Al-coated (3500 Å) Si wafer. The lower x-ray SLD values for the Al_2O_3 outer layer show that porous structures (density of 2.4 g cm^{-3}) were obtained.

Comparing the 30-s (in dark blue) and 60-s (in light blue) data in Figure 53(b), the growth rate of the porous Al_2O_3 layer increases. Small change in Al results in large change in porous AAO, which implies that dissolution of Al_2O_3, slows from 30 to 60 s compared to from 0 to 30 s.

We verified that the oxide (Figure 53**)** is the porous Al_2O_3 using the scanning electron microscopy (SEM). In both 30-s and 60-s samples we observed (Figure 54) an ordered porous structure (array of cells with cylindrical pores) with pore diameters of ~5 nm.

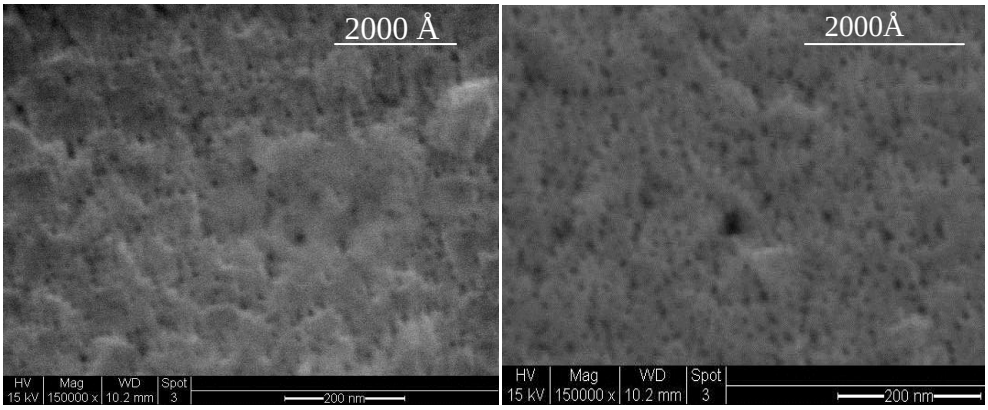

Figure 54. SEM images of the anodic porous Al_2O_3 film on 3500-Å Al-coated Si wafer. The Al_2O_3 film (a) and (b) were obtained by anodizing at 5 V in 20 wt% sulfuric acid for 30 s and 60 s, respectively. An average pore diameter of less than 50 Å is observed.

5.8.4 New anodizing protocol: current-limited and voltage-controlled anodizing

The above results show that we can grow films suitable for XRR analysis with pore diameters less than 50 Å. For the sealing studies to follow, however, we need larger pores, which require higher voltage. Higher voltages, however, strip the thin Al films required for XRR analysis. To circumvent this incompatibility between film thickness and pore size, we developed an alternative anodizing protocol. We apply a higher voltage but control the growth rate so that the Al substrate is not consumed.

To achieve large pores on a thin substrate, we applied concurrent voltage and current control. We used the power supply to set a limit on the current density. We then execute normal voltage-control but with a higher voltage (15 or 20 V). When the current density reaches the limiting value, however, current control takes over. As will be shown below, this strategy works because the dimensional scale of the pores is fixed within the first 20 s (Section 5.9).

The anodizing scheme was tested on 3000-Å pure Al coated Si wafers in a 20-wt% H_2SO_4 solution for 30 s. At a constant voltage of 15 V, the current density was limited at 0.009, 0.013, and 0.015 A cm^{-2}, respectively. The reflectivity results shown in Figure 55 indicate significant structural differences for these samples. At low current density (0.009 A cm^{-2}), the top AAO surface is very rough with no fringes indicating the formation of a thick Al_2O_3 beyond the resolution limit of the instrument. The four-layer model (SiO_2, Al, dense AAO, and porous AAO) is also necessary to fit the reflectivity for all samples, resulting in the SLD profiles shown in Figure 55 (b). Most of the Al remains unconsumed for all current limits. The thickness and the SLD of the porous AAO layer vary with increasing current limit.

As shown by results in Figure 56 **t**o obtain a porous AAO layer with combination of reasonable thickness and high porosity, a current density limit of 0.015 A cm^{-2} should be used.

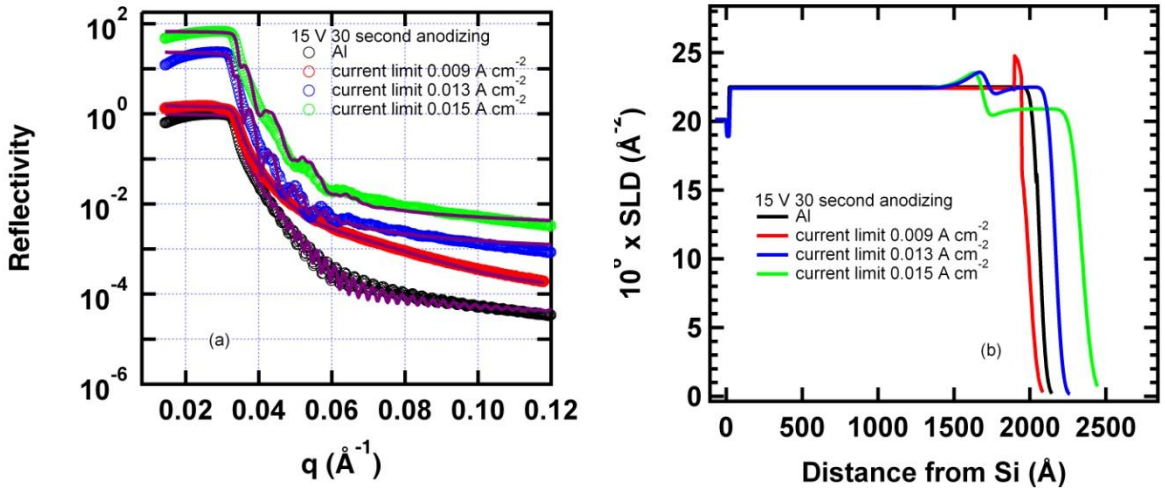

Figure 55. (a) X-ray reflectivity and (b) SLD profiles of the anodized pure Al-coated Si wafers under combined voltage and current control. As the current limit increases, the porous AAO layer thickens and becomes less dense. The density and thickness of the inner AAO layer, however, is independent of the current density limit.

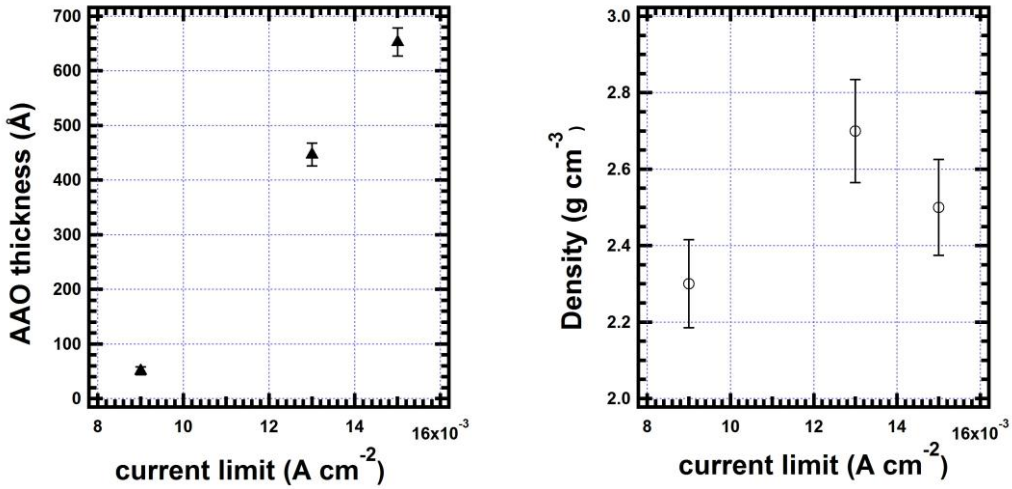

Figure 56. (a) Thickness and (b) density of the porous AAO using the concurrent limited-current and voltage control method (at 15 V in 20 wt% H_2SO_4 solution). Current limit varies from 0.009 to 0.015 A cm^{-2}.

The new anodizing method is compared with the simple voltage-control protocol in Figure 57. The current-limited, voltage-controlled anodizing method produces films with reasonable thickness and porosity. Without current density limit, the Al layer dissolves quickly at 15 V, and the formed AAO film immediately detaches from Si substrate, resulting in a bare Si wafer with only few nm of Al coating left.

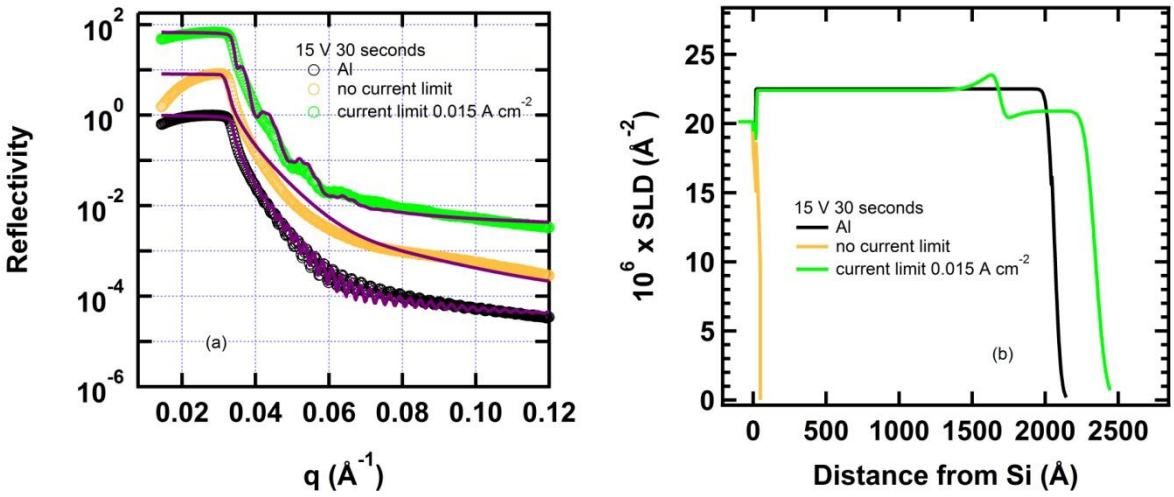

Figure 57. Comparison of (a) X-ray reflectivity and (b) SLD profiles of the anodized pure Al-coated (2000 Å) Si wafers with and without current limit. At 15 V without current limit, Al and AAO dissolve rapidly leaving minimal Al (in orange). With simultaneous current limit and voltage control (15 V), a dense AAO and a porous AAO layer are formed (red).

From the above data we conclude that to obtain a thick AAO with high porosity, a simultaneous current limit at 0.015 A cm^{-2} and voltage at 15 V is required. For most of the samples studied above by this method less than 1000 Å of pure Al is unconsumed so we can apply the same anodizing strategy on 1000-Å Al coated Si wafers with a goal to utilize the most of the Al coating. We applied a current limit of 0.015 A cm^{-2} and a voltage control of 15 V on these 1000-Å Al-coated Si wafers anodized in 20 wt% H_2SO_4 solutions for 15 to 20 s.

5.8.5 Morphological structure of AAO by current-limited, voltage-controlled anodizing

Samples prepared by the simultaneous current limit (0.015 A cm^{-2}) and voltage control (15 V) are ideal to examine the relationship between process parameters and AAO morphology.

Figure 58 and Figure 59 are the XRR and NR results for 1000-Å pure Al. The 1000-Å thickness is optimum given resolution of the instruments. This thickness also accommodates thick AAO layers. The XRR data show that porous AAO forms with thickness of 1200 Å after anodizing at 15 V for 15 second, and 1050 Å from NR data (Figure 59)

Agreement between XRR and NR data on thickness profile of AAO show that the anodic Al_2O_3 using sulfuric acid anodizing is smooth and at the optimal thickness for future *in situ* sealing studies.

Based on Equations 47 and 48 we compare the two SLD profiles from XRR and NR data shown in Figure 58 and Figure 59, to determine the chemical composition of Al_2O_3 in the porous layer.

$$\frac{\boldsymbol{SLD_{x-ray}}}{\boldsymbol{SLD_{neutron}}} = \frac{(\sum_{molecule} \boldsymbol{b_i})_{x-ray}}{(\sum_{molecule} \boldsymbol{b_i})_{neutron}} \tag{47}$$

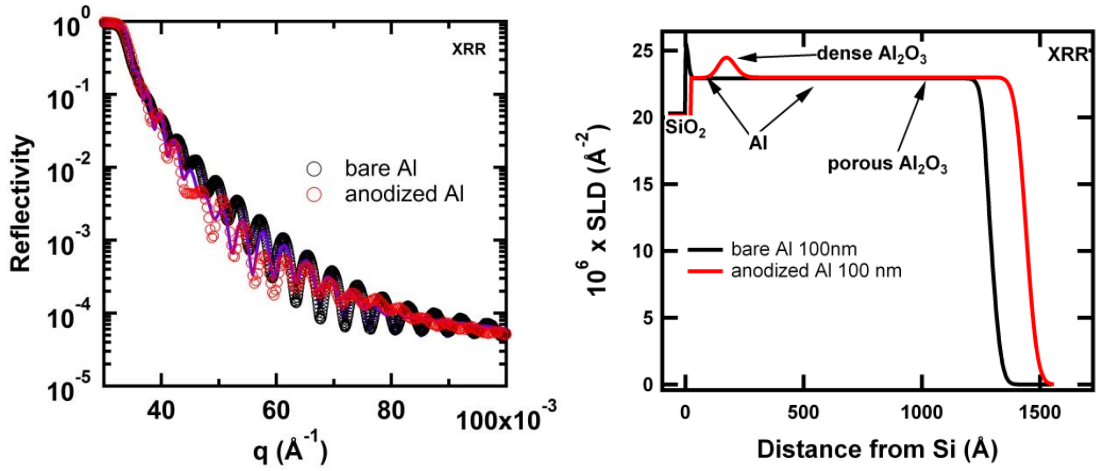

Figure 58. (a) XRR and (b) SLD profiles of the anodized pure Al prepared under optimized conditions. The solid purple lines in (a) are the fits. A density of 2.7 g cm^{-3} was obtained for the porous Al_2O_3 outer layer. Note that the oxide and pure Al have virtually the same SLD consistent with the fact that XRR is only weakly sensitive to chemical composition.

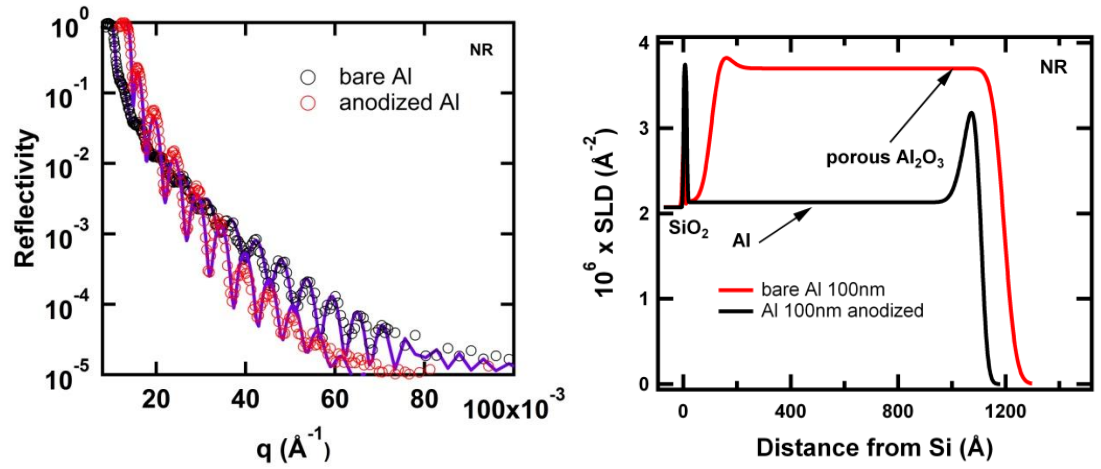

Figure 59. (a) SPEAR neutron reflectivity and (b) SLD profiles of the anodized pure Al-coated (1000 Å) Si wafer. These are the same samples as Figure 58. The solid purple lines in (a) are the fits. A density of 2.6 g cm^{-3} was calculated for the porous Al_2O_3 outer layer assuming pure Al_2O_3 composition. Comparing to Figure 58 one observes that NR is much more sensitive to chemical composition since the neutron SLD of Al_2O_3 is quite different from that of the metal.

Assuming a chemical composition of $Al_2O_3 \cdot x\ H_2O$ and substituting the b_i value known for Al, H and O, we have the relationship between x-ray and neutron scattering length as follows

$$\frac{SLD_{x-ray}}{SLD_{neutron}} = \frac{(b)_{\mathrm{Al2O3,x-ray}} + x \times (b)_{\mathrm{H2O,x-ray}}}{(b)_{\mathrm{Al2O3,neutron}} + x \times (b)_{\mathrm{H2O,neutron}}}$$

$$\frac{SLD_{x-ray}}{SLD_{neutron}} = \frac{\big((2 \times 13 + 3 \times 8) + x \times (2 \times 1 + 8)\big) \times 0.28 \times 10^{-12}}{((2 \times 0.345 + 3 \times 0.58) + x \times ((2 \times -0.374 + 1 \times 0.58)) \times 10^{-12}} \quad (48)$$

A x-ray SLD value of 23.0×10^{-6} Å^{-2} and a neutron SLD value of 3.7×10^{-6} Å^{-2} obtained from Figure 58 and Figure 59 were used for the calculation of chemical composition of $Al_2O_3 \cdot x\ H_2O$, resulting in $x = 0.287 \pm 0.012$. Therefore a composition of the AAO is $Al_2O_3 \cdot (0.29 \pm 0.06)\ H_2O$, which indicates minimal hydrate water.

Using the chemical composition of $Al_2O_3 \cdot 0.29\ H_2O$, we can calculate the AAO molecular weight, *M*, as 107, and its x-ray scattering, and neutron scattering lengths. Substituting these values in Equation 2 and using the x-ray SLD value of 23.0×10^{-6} Å^{-2} or a neutron SLD value of 3.7×10^{-6} Å^{-2}, the density of the $Al_2O_3 \cdot 0.29\ H_2O$ is calculated to be 2.8 ± 0.14 g cm^{-3} in good agreement with the NR and XRR results. This analysis is slightly compromised if other ions are incorporated in the film, but even that situation can be sorted out by measuring the dehydrated the film or comparing deuterated and hydrogenated films.

5.9 Characterization of AAO by ultra small-angle x-ray scattering (USAXS) and small-angle neutron scattering (SANS)

XRR and NR have revealed the interface morphology profile normal to the AAO surface. The in-plane morphology of the porous AAO can be explored by small angle scattering. The details about ultra small-angle x-ray scattering (USAXS) and small-angle neutron scattering (SANS) techniques are given in section 4.5.3. Since we are not limited to thin films in this case, we studied pure Al foils using the conventional voltage control method.

5.9.1 Growth of porous AAO

The growth of porous AAO was investigated by anodizing of Al foils (0.001 inch in thickness, and 2 × 2 inches) at 15 V in a 20 wt% sulfuric acid for increasing times at a 10 s interval. Figure 60 reveals the development of USAXS profile as a function of anodizing time. The intensity of the interference peak increases as the anodizing time increases signaling the development of more and/or larger pores.

A three-level unified fit was used for fitting of the USAXS data. The details of unified fit are discussed by Beaucage et al.[56] The unified approach is common in the SAXS community, but in our case, we had to take into account the spatial correlation of the pores. Using code imbedded in the Irena package form Argonne National Laboratory the parameters for a correlated pore structure were extracted.[7] A representative unified fit of the AAO is shown in Figure 61. The results on the Guinier and Porod regions for all three levels are summarized in Table 3. As shown, the first level (largest *q*) is a unified fit with correlation parameters of 264 Å for ζ (inter-pore distance), and 8.0 for packing factor. Using the correlation parameters, interference between densely packed hexagonal pore structure is taken into account in the unified fit. The same fitting approach was applied to all data shown in Figure 60 except for pure Al (non-correlated system was assumed). The first structural level is due to the porous AAO outer layer (Table 3).

Table 3. First-level parameters from 3-level unified fitting of the USAXS data of Al foil samples. The parameters are the Guinier and Porod parameters described in Section 4.5.3. There is no first level for Al.

Sample	R_G**(Å)**	***G***	***B***	***P***	***ζ***	***Packing factor***
Pure Al	N/A	N/A	N/A	N/A	N/A	N/A
AAO (10 sec)	70.34	38.17	0.23476	0.5	261.99	5.2369
AAO (20 sec)	73.28	112.16	1.338e-05	4	262.28	8
AAO (30 sec)	76.22	304.14	3.071e-05	4	264.76	8
AAO (40 sec)	73.52	714.25	7.273e-05	4	272.62	8
AAO (50 sec)	81.61	594.30	4.317e-05	4	272.40	8
AAO (60 sec)	74.04	1396.52	7.798e-05	4	270.96	8
AAO (70 sec)	75.67	1764.99	6.999e-05	4	277.81	8
AAO (80 sec)	74.37	2736.66	9.995e-05	4	275.46	8
AAO (90 sec)	73.50	2046.82	7.925e-05	4	271.20	8
AAO (100 sec)	75.83	2205.92	1.031e-04	4	273.91	8
AAO (110 Sec)	75.39	3807.1	1.200e-04	4	272.40	8
AAO (120 sec)	71.21	5193.4	1.905e-04	4	264.14	8

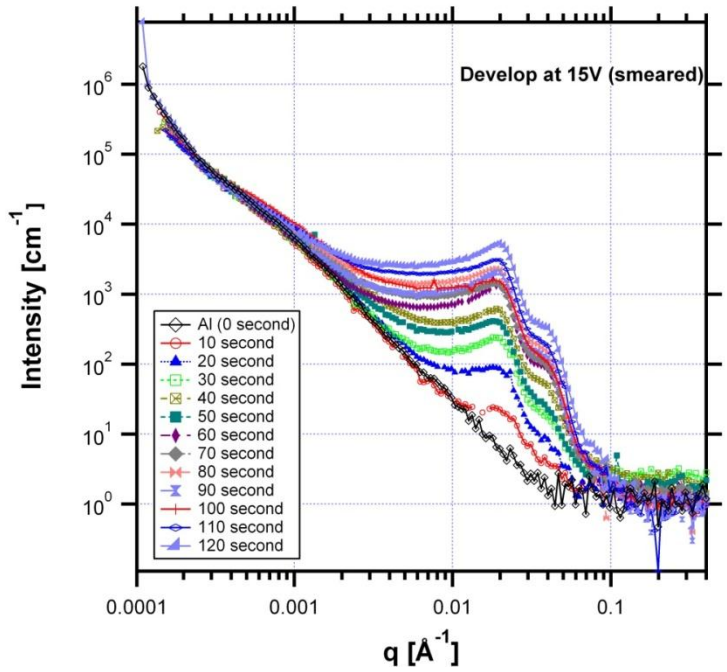

Figure 60. Slit-smeared USAXS data showing the evolution of AAO porosity for pure Al foils anodized at 15 V in 20 wt% H_2SO_4. The data are on dry samples removed from the anodizing bath at various time up to 120 s. Scattering in the peak region is due to pore formation.

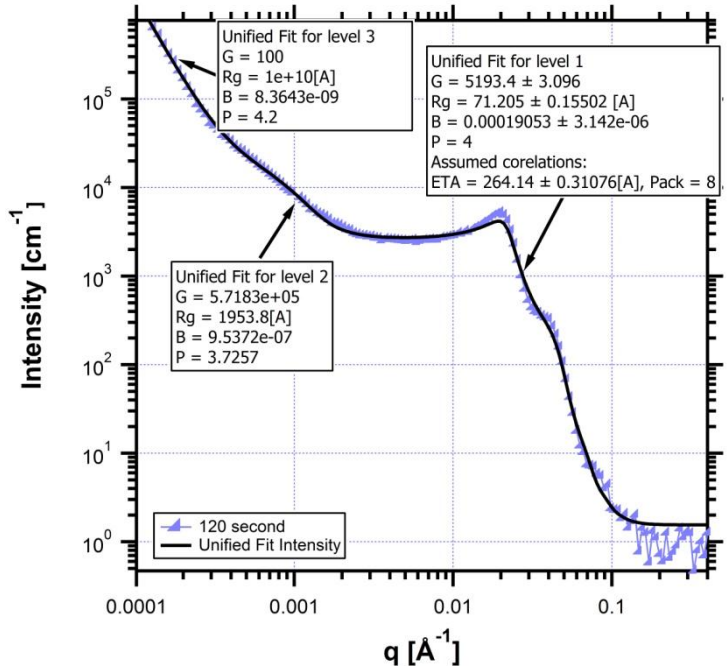

Figure 61. A representative 3-level unified fit for the AAO film formed by anodizing for 120 s. The R_G, *G*, *B*, *P* values are shown for all three levels. For level 1, a correlated system is assumed to account for the peak. The values for correlation range, ζ, and packing factor, *pack*, are also shown. The fitting is done on the slit-smeared data.

The AAO structure is commonly recognized as a hexagonal array of straight non-intersecting channels as shown in Figure 62. Since the pores are the minority phase, R_G measures the pore radius, not the strut thickness.

$$l_p = 2 \times \sqrt{2} R_G \tag{49}$$

The correlation length, ζ, is approximately the inter-pore distance. The pore size (l_p) is estimated by relationship between inter-pore distance and the wall thickness as follows

$$l_s = \zeta - l_p \tag{50}$$

Based on values in Table 3 and Equations 49-50, we calculated the pore diameter, wall thickness, and inter-pore distance shown in Figure 62, which reveals the kinetics of pore growth.

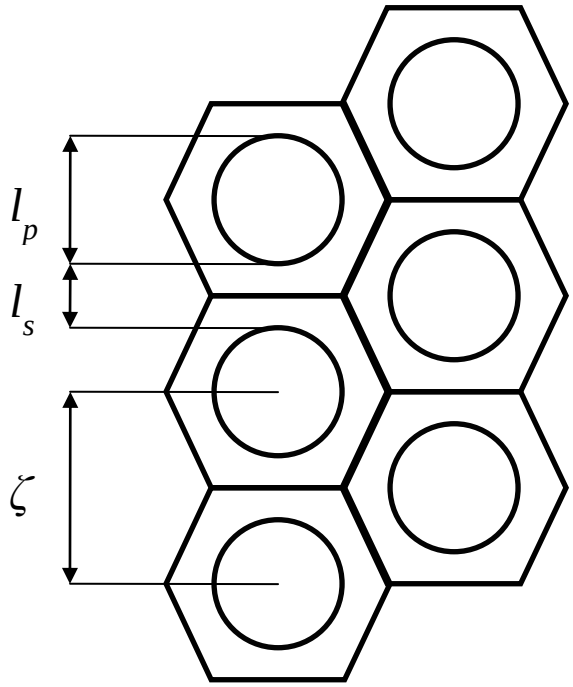

Figure 62. Schematic top view of the structural features of AAO. Pore diameter (l_p), wall thickness (l_s) and inter-pore distance (ζ) can be determined by the Guinier parameters obtained from unified fit of the USAXS data.

The dependence of these parameters on anodization time is shown in Figure 63. The pore morphology is fixed in the first 20 s. The fact that the intensity continues to increase (*G* parameter in Table 3 from 10 to 120 s) means that the pore length increases with anodization time. The pore length therefore can be calculated by

$$L = \left(\frac{\mathrm{G}}{N_v SLD^2 4\pi R_g^2}\right)^{1/2}$$

(51)

where G, and R_g are the fitting parameters from Guinier's regime as shown in Table 3, N_v is the number density of the pores, and SLD is the average scattering length density of Al_2O_3. As shown, the pore diameter, interpore distance and wall thickness are independent of time and the pore length increases linearly with time.

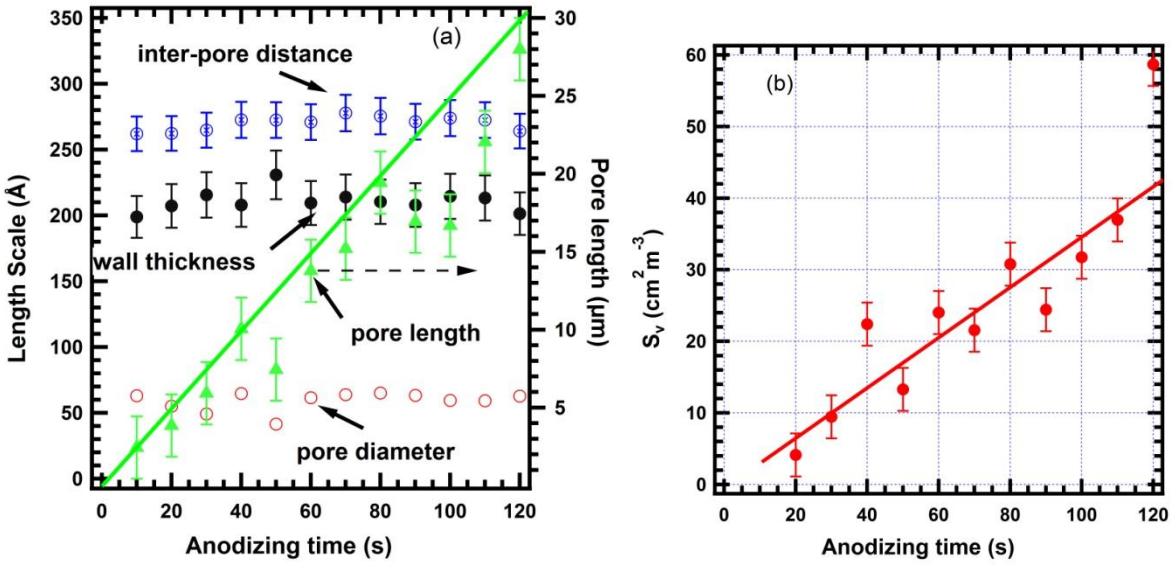

Figure 63. The evolution of (a) pore diameter, wall thickness, inter-pore distance and (b) surface area during anodizing time 0 to 120 s. The structure stabilizes after 20-s of anodizing. The pores fully penetrate the film at 120 s. The surface area increases monotonically with increasing anodizing time due to pore length growth.

5.9.2 Surface area analysis of the AAO structure

The surface area per unit volume can be calculated (Equation 7) from the first-level unified fit of the USAXS data. The surface area analysis was developed by our group[57] and adopted in the IRENA package. A density of 2.65 g cm^{-3} is used for the porous Al_2O_3 as the average from the XRR and NR analysis described earlier (Figure 58 and Figure 59). The surface area results are plotted in Figure 63(b). The surface area per unit volume (S_v) increases as anodizing time increases from 10 to 110 s monotonically.

5.9.3 Anisotropy of the AAO structure

To determine pore orientation, the angle (Φ) at which the beam strikes the sample (normal = 0°) and edge-on = 90°) was varied. The 120-s sample where the pores penetrate the entire foil was used for this experiment. The USAXS intensities are shown in Figure 64. The correlation peaks disappear for all non-face-on samples showing that the pores grow normal to the foil surface.

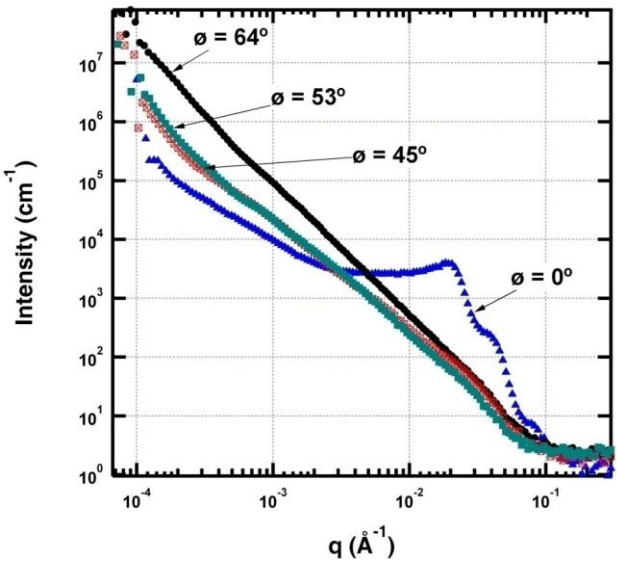

Figure 64. Effect of foil orientation on USAXS profile. Φ is the angle between scattering vector *q* and the plane of the foil. The pattern shows that pores are oriented perpendicular to the foil surface.

5.9.4 Effect of voltage and electrolyte on AAO structure by USAXS and SANS

We investigated the effect of voltage and electrolyte by anodizing at 10, 15, and 20 V in 20 wt% sulfuric acid, 3% oxalic acid and 5% phosphoric acid solutions. The samples were anodized until all the Al is converted to AAO. Since the kinetics of reactions is different, the time needed for Al conversion into AAO is therefore different. For sulfuric acid at 15 and 20 V, 120 and 60 s are needed, respectively. For 10 V the anodizing time is longer than 60 minutes. For oxalic acid and phosphoric acid solutions an anodizing time longer than 60 minutes is needed. The USAXS and SANS results for the final anodized products in air are plotted in Figure 65 and Figure 66.

The dependence of AAO structure on voltage is revealed by both USAXS and SANS data in Figure 65. As the voltage increases (in 20-wt% sulfuric acid electrolyte) the position of the interference peak shifts to lower *q*. The 3-level unified fits of the USAXS data are shown by solid lines in Figure 65(a) and the wall thickness, pore size and inter-pore distance are obtained from the level-1 fitting parameters. The results are plotted in Figure 67(a), which show the relationship between pore size and anodizing voltage.

The effect of electrolyte is more significant than the voltage as shown in Figure 66. Pores formed in both oxalic acid and sulfuric acids are more correlated (show a more distinct peak) than when formed in phosphoric acid. Sulfuric acid produces smallest pore size at the same anodizing voltage.

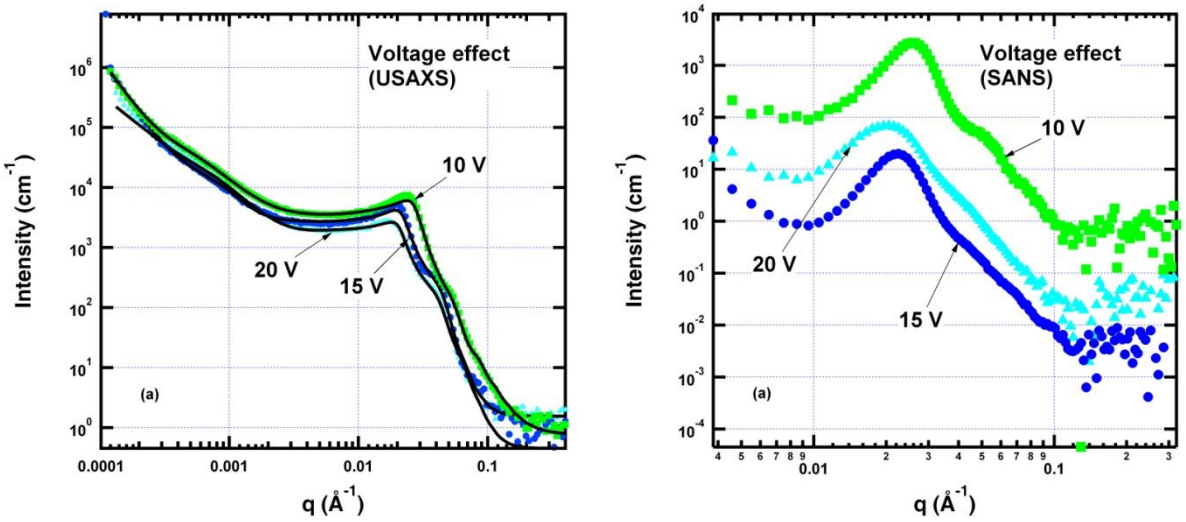

Figure 65. (a) USAXS and (b) SANS data on pure Al anodized at different voltage. Maximum time of anodizing was used for all voltages assuming that in the final structure Al is completely converted into AAO. Samples are measured in air. The solid lines in (a) are the 3-level unified fits of the intensities. The USAXS data are slit-smeared

The dependence of pore size, wall thickness, and inter-pore distance on voltage and anodizing electrolyte is compared in Figure 67 (b). We observe a monotonic relationship between pore size and voltage. The pore size is the greater in phosphoric acid than in oxalic acid and sulfuric acid.

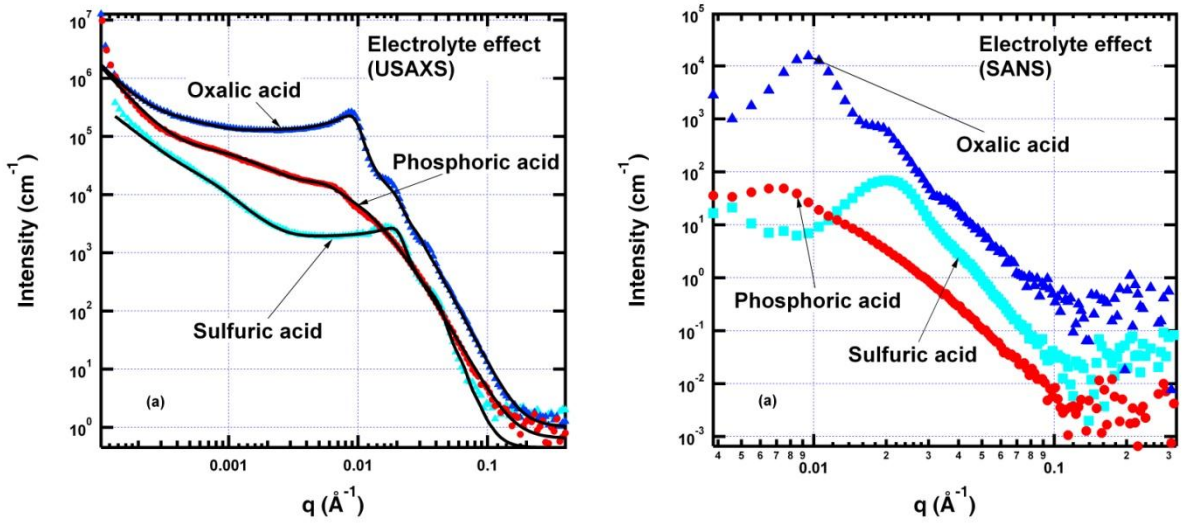

Figure 66. (a) USAXS and (b) SANS data on AAO samples prepared in different anodizing electrolyte (sulfuric acid, oxalic acid, and phosphoric acid). Maximum time of anodizing was used for all samples assuming that all the Al is converted into AAO. The solid lines in (a) are the 3-level unified fits of the intensities. The USAXS data are slit-smeared.

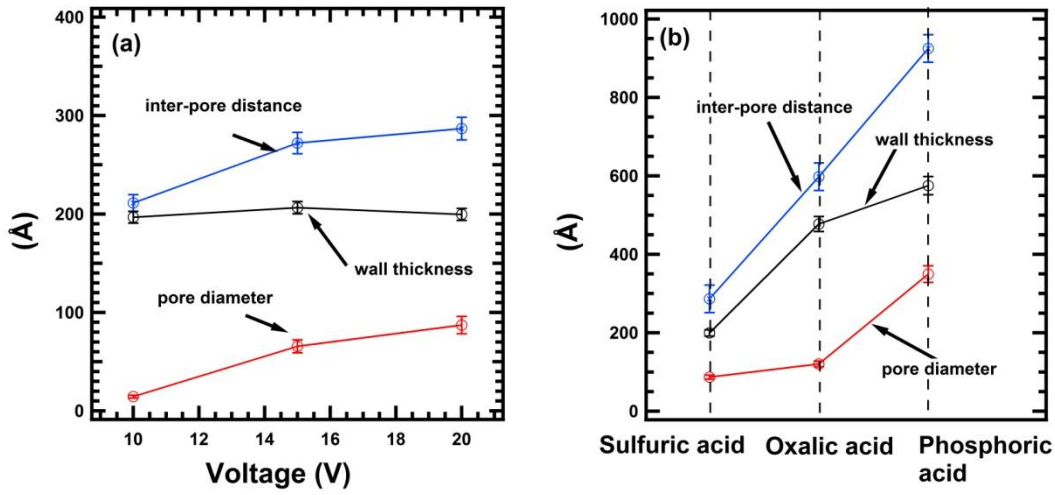

Figure 67. Effect of (a) anodizing voltage and (b) electrolyte solution on AAO structure by USAXS data.

5.9.5 Validation of AAO composition by USAXS and SANS

The intensities of USAXS and SANS for a through-thickness AAO sample are compared in Figure 68 for a sample anodized in oxalic acid. The ratio of measured USANS and USAXS intensities should be independent of the sample density and proportional to the ratio of x-ray scattering length to neutron scattering length by

$$\frac{I(USAXS)}{I(USANS)} = \frac{(SLD_{x-ray})^2}{(SLD_{neutron})^2} = \left(\frac{\Delta r_{x-ray}}{\Delta r_{neutron}}\right)^2 \tag{52}$$

As shown in Figure 68, the intensity ratio from experimental data is 35.89 ± 0.08. For oxalic acid, the contrast ratio of 35.9 is in reasonable agreement with the value of 33.6 based on composition of $Al_2O_3 \cdot 0.29\ H_2O$ determined from combination of XRR and NR discussed in earlier section.

5.10 Sealing on AAO

Sealing is necessary to improve corrosion resistance of the porous AAO film. Sealing strategies, based on various combinations of temperatures and chemical composition of the sealing bath, all improve corrosion resistance to some extent. The structural alternation induced by sealing and the impact of structure on corrosion resistance, however, had not been investigated previously.

In this section, we first compare the effect of different sealing methods on corrosion performance of AAO. XRR, NR, USAXS and SANS are used to investigate the structural modification caused by sealing. Cold nickel acetate sealing is of particular interest because this method has been reported to be a promising sealing technology to compete with the conventional hot water sealing. Therefore the impact of cold sealing on pore structure is discussed in detail.

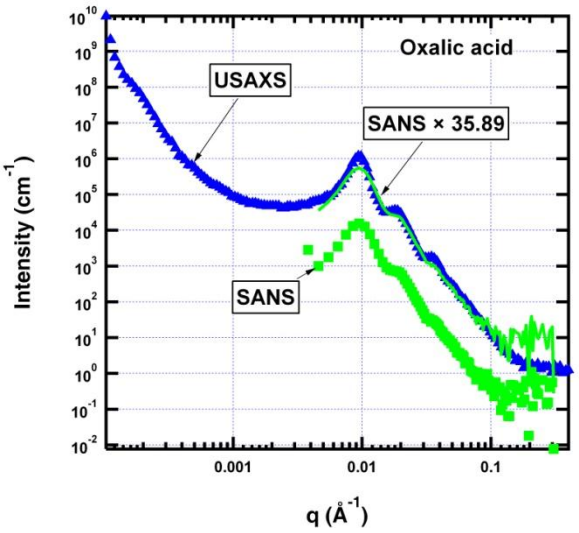

Figure 68. Intensity ratio of USAXS to SANS for through-thickness AAO samples obtained in 3% oxalic acid at 20 V. A contrast ratio of 35.89 ± 0.08 is obtained. The value is 33.62 based on composition of Al_2O_3. For comparison to SANS data, the USAXS data shown in this figure are desmeared.

5.10.1 Effect of Sealing on corrosion performance

We first investigated the corrosion performance of anodic films (pre- and post-sealing) on Al coupons using dynamic direct current polarization (DCP) and electrochemical impedance spectroscopy (EIS). Three sealing methods (hot water, saturated cold nickel acetate, and 5 g/L hot nickel acetate sealing) were applied on the AA1100 coupons (2 by 2 inches).

The DCP curves before and after sealing are compared in Figure 69. For all sealed samples, the corrosion performance improves as revealed by a combination of higher OCP, lower cathodic current density and lower anodic current density. Sealing by hot nickel acetate shows the highest OCP (-0.48 V), while sealing by cold nickel acetate shows the least improvement over the un-sealed sample. The mechanism of different sealing methods is the object of this study and will be explored using combination of USAXS, XRR, and NR techniques as discussed in the following section.

Electrochemical impedance spectroscopy (EIS) measures the ohmic resistance (*R*) and capacitance (*C*) of the passive films from the current response to an alternating potential. The product *RC* is the characteristic relaxation time.

As expected from the Hoar and Wood models[58] our EIS spectra typically contain two time constants[59] which are due to a thin, compact, inner barrier layer and the outer porous layer. For a system with a 200-Å barrier layer and a 1-μm porous layer, the capacitance of the barrier layer is around 0.5 μF/cm^2, while the capacitance of the porous layer (unsealed) is around 0.001 μF/cm^2.[58] The capacitance of the water-saturated porous layer is so small that it can only be detected at frequencies higher than 10^7 Hz. On unsealed films, therefore, the measured spectra for frequencies below 10^5 Hz consist mainly of the contribution from the inner barrier layer.[60] Our EIS results on unsealed anodic films are consistent with the above analysis. As shown in the Bode plots (Figure 70) obtained during exposure to 1-wt% NaCl, we observed one time constant for the unsealed sample as shown by the single maximum in the phase angle plot (black dashed

line). Such behavior is observed because the outer layer is "transparent" to EIS due to water intrusion. The capacitance of the dense barrier layer (estimated to be 0.8 μF / cm^2 from the Bode plots) is responsible for the observed time constant. This value is higher than the 0.5 μF / cm^2 given by Hoar and Wood for a 200 Å-thick barrier layer,[58] suggesting a thinner layer due to different anodizing conditions. In addition, the total ohmic resistance calculated from the Bode plots (black line) is 1.6×10^4 ohm, higher than the resistance expected from single layer of porous structure. Therefore, we conclude that the response peak at 10 Hz must be due to the barrier layer postulated by others in anodic films.

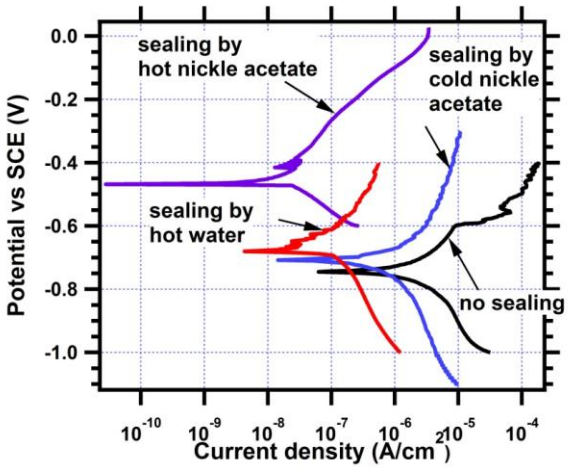

Figure 69. DCP for anodic films with and without sealing in 1 wt% NaCl de-aerated aqueous solution. All samples were conditioned at OCP for 30 min prior to the scan. The scan rate was 1 mV / s. Hot sealing in nickel acetate (purple) yields highest OCP, and lowest anodic current density.

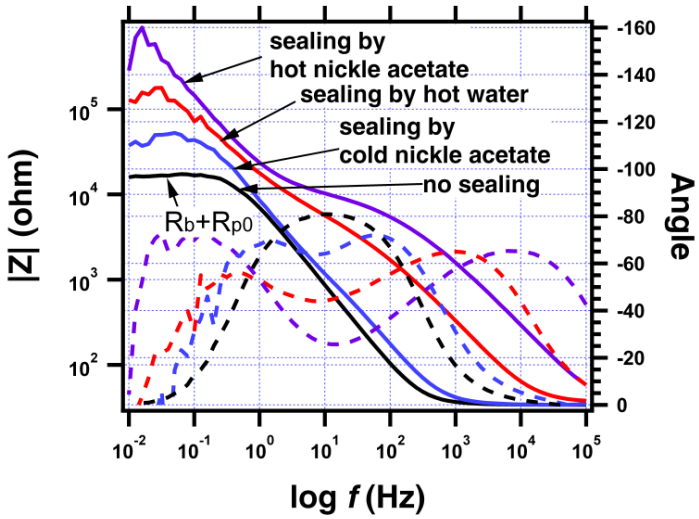

Figure 70. Bode plots for sealed and unsealed anodic films. Dashed lines are the phase angles (right axis), and the solid lines are the impedances (left axis). The unsealed sample shows only one time constant. The sealed samples (red, blue, and purple dashed lines) show two maxima, suggesting increased pore resistance R_{p0}. The hot sealing methods improve the corrosion resistance more than the cold method as shown by the increase of $R_b + R_{p0}$ of the sealed samples.

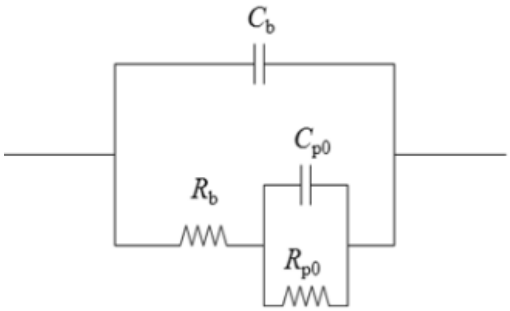

Figure 71. Equivalent circuit of anodized Al alloys. R_{p0} is the ohmic resistance of porous layer, R_b is the ohmic resistance of barrier layer, C_{p0} is the capacitance of porous layer, and C_b is the capacitance of barrier layer.

The phase angles of the sealed samples (blue, red, and purple dashed lines) all show two maxima. The response at high frequencies is attributed to the porous oxide layer. The second maximum arising at low frequency is due to the denser barrier layer at the metal interface.

Bode plots also show improvement of the corrosion resistance for sealed samples. The resistance of the barrier (R_b) and porous (R_{p0}) layers extracted from the impedance data based the equivalent circuit shown in Figure 71 are summarized in Table 4. The overall corrosion resistance is measured by R_b + R_{p0}. As shown in Table 4, all sealing methods show increased pore resistance (R_{p0}), implying that sealing increases the corrosion resistance by filling the pore structure. The resistance of the barrier layer, R_b after sealing also increases, which implies that this layer is porous as well, consistent with the XRR results described earlier. In addition, the capacitances of both the porous and dense layers decrease for all sealed samples. Therefore, sealing modifies both the porous and dense Al_2O_3 layers. Hot nickel acetate shows the highest R_{p0} and lowest $C_{p0.}$ The improvement by cold sealing with nickel acetate, however, is limited due to the incomplete penetration of the sealing agent into the barrier-layer pores.

Table 4. Estimated resistance of porous layer (R_{p0}), resistance of barrier layer (R_b), capacitance of porous layer (C_{p0}) and capacitance of barrier layer (C_b) from the EIS spectra.

Anodic film	R_{p0} (ohm)	R_b (ohm)	C_{p0} (μF / cm^2)	C_b (μF / cm^2)
Unsealed	34	1.63×10^4	N/A	0.8
Sealed by saturated cold nickel acetate	5×10^3	4.52×10^4	0.4	0.56
Sealed by boiling water	8×10^3	1.49×10^5	0.08	0.44
Sealed by 5g/L hot nickel acetate	2×10^4	9.08×10^5	0.04	0.2

5.10.2 Impact of sealing on pore structure

The impact of sealing on AAO pore structure was measured by USAXS and SANS. The results shown in Figure 72 lead to similar conclusions from both USAXS and SANS. The AAO structure after sealing by cold nickel acetate (both saturated, and 5 g/L) and hot water is significantly different from that after sealing by hot 5 g/L nickel acetate, implying different sealing mechanisms. Three-level unified fits of the USAXS data for all samples in Figure 72(a) are shown as solid lines. The alteration of the pore size, wall thickness, and inter-pore distance is summarized in Table 5.

The wall thickness increases from 210 Å to ~250 Å for cold nickel acetate sealing. The corresponding pore size decreases indicating deposition of the sealant on the pore walls. Within error there is no dependence on the nickel acetate concentration.

Hot water sealing leaves the cylindrical pore structure intact with a slight decrease on the inter-pore distances. However, the wall thickness increases by a factor of two indicating swelling of the skeleton due to hydration by water. Hot nickel acetate sealing, not only alters the inter-pore distance but also increases the wall thickness. There is only a faint signature of the original pore structure after hot nickel acetate sealing. Therefore, hot nickel acetate fills the pores and deposits on the air surface.

Table 5. Pore size, wall thickness, and inter-pore distance of the through-thickness AAO samples after being sealed by different methods (30 minute immersion for all samples). The parameters are extracted from the USAXS data. The AAO samples before sealing are obtained by anodizing at 15 V in 20 wt% sulfuric acid for 120 s.

Sample	**Pore size, l_p (Å)**	**Wall thickness, l_s (Å)**	**Inter-pore distance (Å)**
AAO (no sealing)	55 ± 10	210 ± 14	261 ± 2
Sealing by cold nickel acetate (5g/L)	21 ± 5	251 ± 20	270 ± 5
Sealing by saturated cold nickel acetate	15 ± 5	250 ± 21	265 ± 4
Sealing by hot water	N/A	382 ± 123	260 ± 6
Sealing by hot nickel acetate (5 g/L)	N/A	N/A	N/A

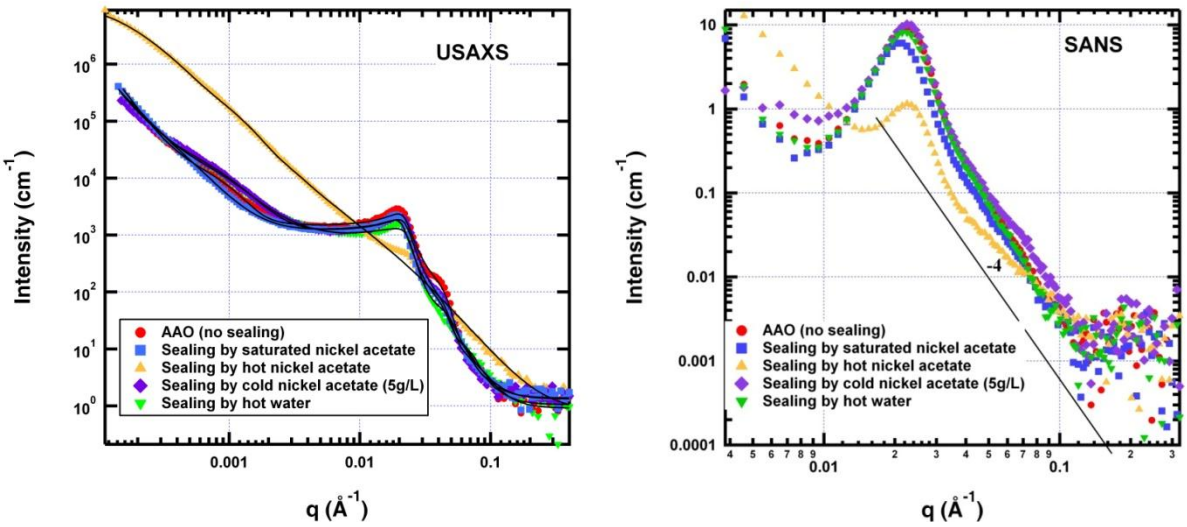

Figure 72. (a) Slit-smeared USAXS and (b) SANS data on through-thickness AAO samples sealed by different methods. The solid lines are a 3-level unified fit of the USAXS intensities. All samples were exposed for 30 min. Sealing by saturated nickel acetate was cold sealing.

5.11 Cold nickel acetate sealing: XRR and NR

Although cold nickel acetate has been proposed to replace conventional hot nickel acetate and hot water sealing methods, we found from USAXS that 30-min cold nickel acetate sealing (saturated or unsaturated) does not significantly alter the original porous AAO structure. The saturated system was chosen for further analysis to resolve the relationship between sealing protocol, structure and performance using XRR and NR.

Cold saturated nickel acetate sealing was examined by NR and XRR as a function of exposure time. First we describe the results of XRR and NR experiments on dry samples after 30-min exposure in the sealing bath. Then we describe two 12-h experiments where we tracked the evolution of the films *in situ* using NR. After 12-h exposure, XRR on the dry samples shows that the final morphology is very different from that observed after 30-min exposure.

5.11.1 Short-term cold saturated nickel acetate sealing by *ex situ* XRR and NR

In preparation for cold nickel acetate sealing, anodizing was performed on 1000-Å Al-coated Si wafers at 15 V in a 20-wt% sulfuric acid at a constant voltage of 15 V for 20 s. Since the Al film is thin the current limit was set at 0.015 A cm^{-2}. The final samples were air-dried for 24 hours after cleaning in de-ionized water. Sealing was performed using saturated nickel acetate solutions. The wafers were immersed in the sealing solution for 30 min at room temperature. The samples were rinsed in de-ionized water and dried in ambient before XRR and NR measurements.

The XRR results on the dry samples (Figure 73) indicate the morphological change induced by anodizing and sealing. Fitting requires a four-layer model for anodized samples both before and after sealing. Before sealing, these four layers on top of Si are SiO_2, Al with a density of 2.7 g cm^{-3}, barrier-layer Al_2O_3 (density of 3.0 g cm^{-3}), and porous Al_2O_3 layers (density of 2.8 g cm^{-3}). The 1000-Å Al coating was almost completely converted into AAO leaving only 20 Å of Al.

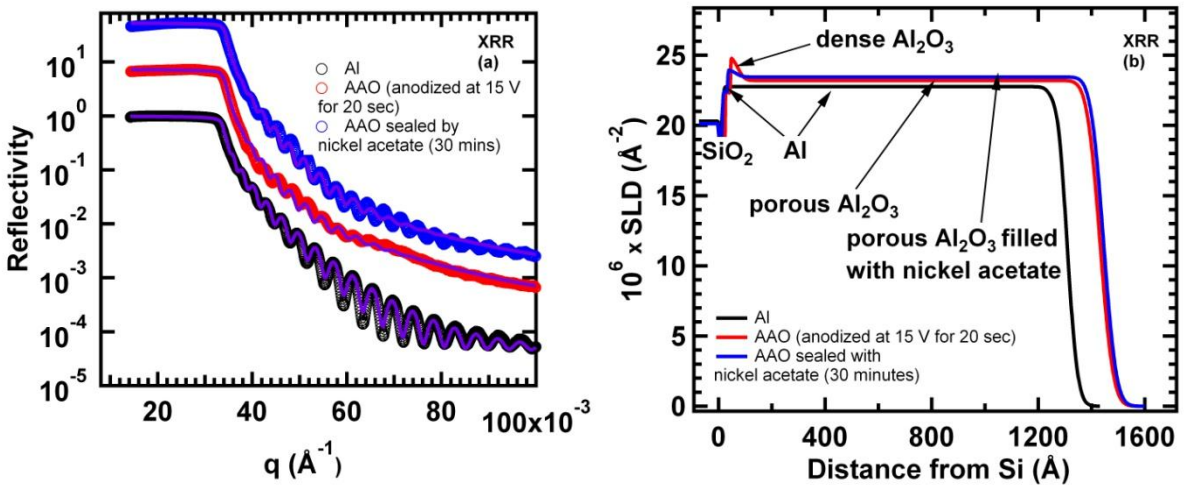

Figure 73. Saturated nickel acetate sealing (a) XRR data and (b) SLD profiles on the Al-coated Si wafers. The anodized sample before sealing (red, anodized in sulfuric acid at 15 V for 20 s), and after sealing (blue, sealied with saturated nickel acetate for 30 minutes) are compared with the bare Al sample (black, 1000-Å pure Al coated wafer). The results indicate minimal change after 30-min sealing.

After sealing, SLD profiles show the four layers on top of Si are also SiO_2, Al, dense Al_2O_3 (density of 3.0 g cm^{-3}), and porous AAO layers partially filled with nickel acetate (slightly higher density of 3.1 g cm^{-3}). Comparison of samples before and after sealing shows that the thickness of the film remains constant during immersion in the sealing bath. There is no deposition of the sealing agent on top of the AAO. Instead small amount of nickel acetate decorates the pores giving a slightly increased density for the AAO layer (from 2.8 to 3.1 g cm^{-3}).

NR confirms that only small amount of nickel acetate remains in the pores after 30-min exposure. As shown in Figure 74, a four layer model is also required to obtain reasonable fitting (solid lines) for both anodic samples (before and after sealing): Si, Al, dense Al_2O_3 (density of 2.9 g cm^{-3}), and porous Al_2O_3. The density of the porous layer also increases (from 2.5 to 2.6 g cm^{-3}) as was observed with XRR (Figure 73). The density values, however, do not agree with the XRR results on the same sample, reflecting the inadequacy of the assumption of constant composition. The thickness shows the same trends, but again with some discrepancy in absolute values compared to the XRR results.

5.11.2 Long-term cold nickel acetate sealing by *in situ* NR

The XRR and NR data for the 30-min dry samples in Section 5.11.1 show minimal change on sealing, which raises questions regarding the alleged beneficial effects of cold nickel acetate sealing. To further elucidate the sealing process we used *in situ* NR in a liquid cell to monitor the evolution of the AAO for 12 h in the 50 g/L cold nickel acetate sealing bath. 50g/L is within a factor of 2 of saturation. Two protocols were used, the first involving continuous exposure and the second involving initial exposure to D_2O followed by a subsequent exposure to 50 g/L nickel acetate solution. These protocols are referred to one-step and two-step sealing.

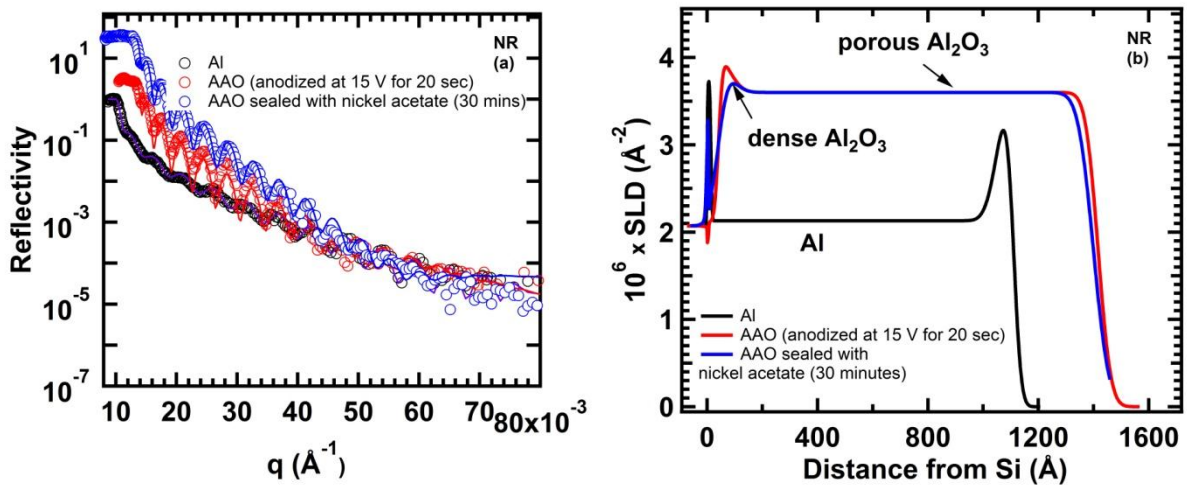

Figure 74. (a) SPEAR NR data and (b) SLD profiles of the pure Al-coated Si wafers. The anodized sample before and after sealing in cold saturated nickel acetate for 30 min are compared with the bare Al sample (in black, 1000-Å pure Al coated wafer). Little change is observed on sealing.

One Step Sealing: An anodized sample (anodized on 1000Å Al-coated Si wafers at 15 V in a 20 wt% sulfuric acid at a constant voltage of 15 V with a current limit of 0.015 A cm^{-2} for 20 s) was mounted in the NR liquid cell filled with 50 g/L nickel acetate in deuterated water. NR snapshots taken every three hours (Figure 75) reveal significant change from the dry state to the sealed state (after 1.5 hours exposure), particularly for the critical edge, which shifts to higher *q* (as shown by insert of Figure 75 (a)), indicating an increased SLD of the outer porous AAO layer. The film thickness, however, is unchanged during the first 1.5 hours of immersion. Therefore, nickel acetate solution initially penetrates into the pores of AAO without swelling of the film. After 1.5 hours, however, the SLD and thickness of the AAO layer increase, implying a swelling effect due to solution penetration of the pore walls.

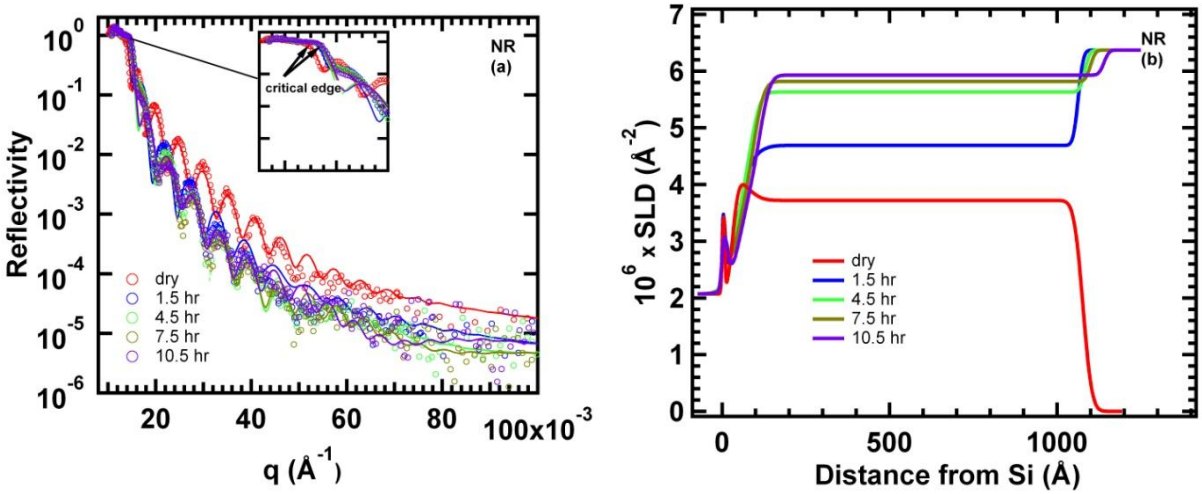

Figure 75. One-step sealing: (a) SPEAR *in situ* NR data and (b) SLD profiles of the anodized Al during sealing by cold 50 g/L nickel acetate. The penetration of nickel acetate solution occurs within 1.5 h. Swelling after 1.5 hours is indicated by increased thickness and SLD of the porous AAO layer.

After 12-h exposure in *in situ* NR cell the sample was dried and examined by XRR. The results in Figure 76 indicate a deterioration of the outer layer of the sealed AAO film. Both the thickness and SLD of the outer porous AAO layer decrease for the sealed sample. In particular, much lower SLD is needed to fit the double critical edge seen in Figure 76(a). However, the dense AAO layer and bottom AAO region show higher SLD (25×10^{-6} Å^{-2}) implying enrichment by nickel acetate or some other nickel compound at the bottom of pores. The reduced SLD at the air surface is attributed to dislodging and/or dissolution of interpore struts, although further work is needed to confirm this speculation.

Two Step Sealing: To separate the effect of D_2O penetration from that of nickel acetate deposition cold nickel acetate sealing was further investigated in a two-step NR experiment. The AAO sample was first immersed in D_2O for 2 h and examined *in situ* by a NR. Then the D_2O bath was replaced by 50 g/L nickel acetate solution at RT. Two NR snapshots were taken at 1.5 and 12 h after the second step (Figure 77). The SLD increases rapidly on exposure to D_2O, but no immediate change is observed on exposure to the 50 g/L nickel acetate solution; the green and blue lines overlap in both the NR data and the SLD profiles. On further immersion up to 12 h, swelling occurs as revealed by the increasing SLD and thickness (purple line). A pore volume fraction of 0.22 was calculated based on the SLD for fully hydrated (green line in Figure 77) and dry states (red line in Figure 77)). After 12 h immersion (purple line in Figure 77)), the calculated porosity is higher at 0.35, indicating penetration of D_2O (and nickel acetate) into the skeletal of the porous AAO, which is also porous.

The results of the two-step experiment in Figure 77 are very similar to the one-step data in Figure 75, which indicates that the observed SLD increase is due primarily to D_2O penetration. Additional water penetration and swelling over the next 12 hours leads to a final structure that is nearly identical to the 1-step experiment. XRR data after drying (Figure 78**)** are also very similar to the 1-step data (Figure 76).

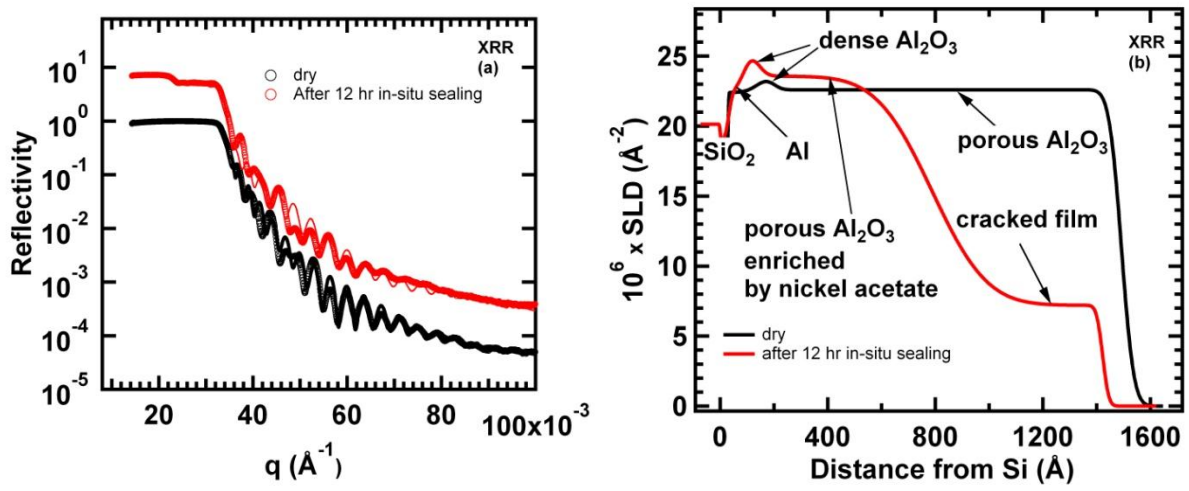

Figure 76. (a) XRR data and (b) SLD profiles of the dry anodized Al before and after one-step sealing by cold nickel acetate. After *in situ* sealing for 12 hours and air-drying, the sample shows significantly lower SLD at the air surface but larger SLD at the metal surface.

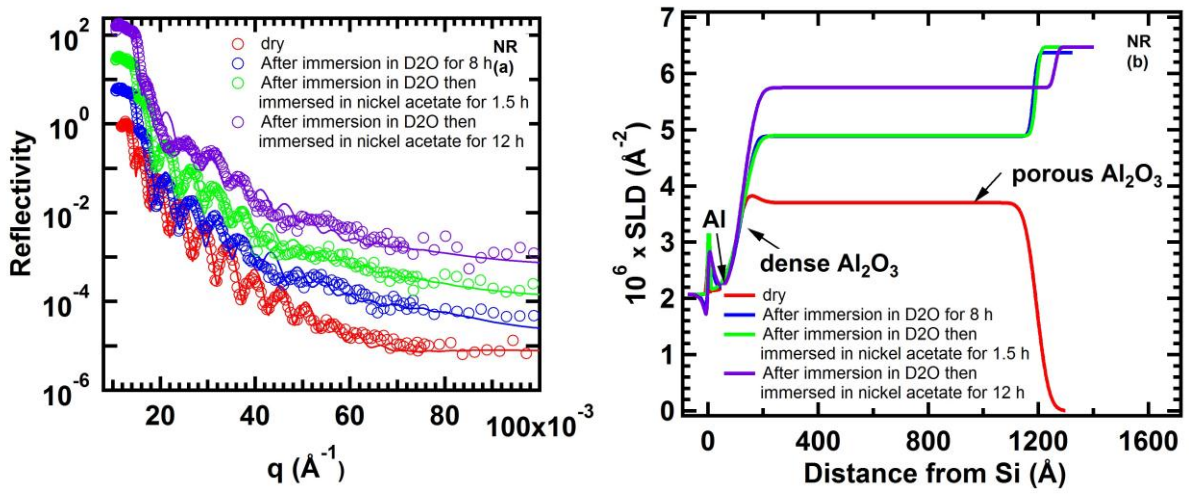

Figure 77. Two-step sealing: (a) SPEAR NR data and (b) SLD profiles of the anodized Al during a two-step sealing by cold 50 g/L nickel acetate. In the first-step the sample is exposed to D_2O. In the second step D_2O solution is replaced by a saturated nickel acetate solution. No change occurs in the second step indicating that the observed SLD shift is due to D_2O penetration. Swelling occurs on further immersion due to additional solution penetration into the Al_2O_3 struts.

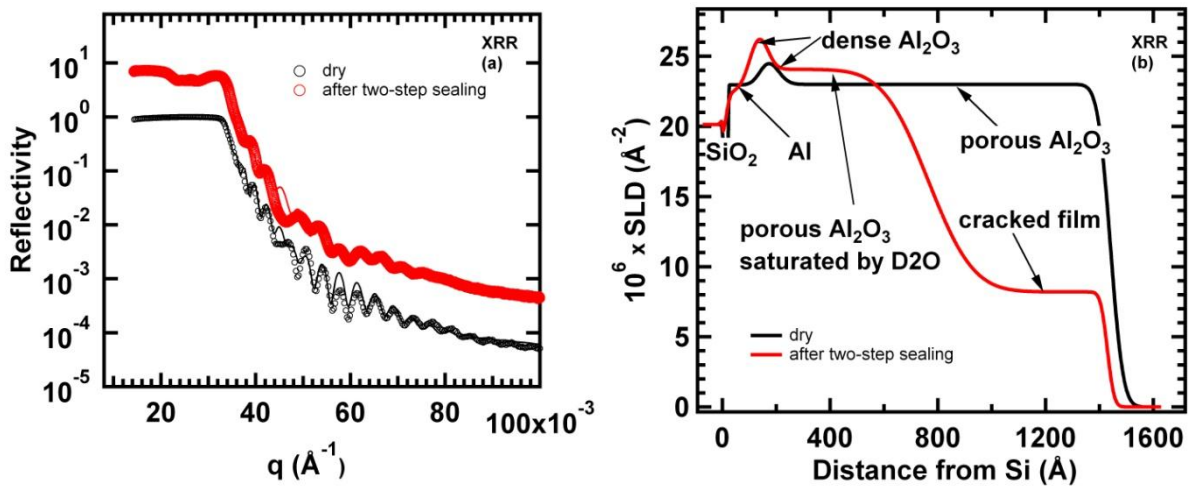

Figure 78. (a) XRR data and (b) SLD profiles of the anodized Al before and after a two-step sealing by cold 50 g/L nickel acetate. After the first-step saturation in D_2O, the second-step immersion for 12 hours destruct the outer layer of the AAO resulting in much lower SLD.

These *in situ* NR results reveal that long exposure to cold nickel acetate solution leads to deterioration of the porous layer. The solution initially penetrates the pores causing the increased SLD with no change in pore morphology. Over the next 12 hours the porous layer imbibes additional solution with some swelling. Very likely the solution penetrates and fills the free volume in the pore walls leading to deposition of nickel oxide or nickel acetate. On drying the presence of the nickel compound in the walls and barrier layer leads to stresses in the solid struts that causes deterioration or breakage of the struts leading to loss of strut material at the outer surface. As a result, the SLD of the outer layer drops considerably on drying. At the same time,

the SLDs of the inner part of the porous layer and the barrier layer increase indicating deposition of a Ni compound in these inner regions.

These results show that the morphology of the dry sealed sample depends on exposure time. Over a period of 12 h a nickel compound deposits primarily in the bottom of the pores. Resulting drying stresses degrade the outer porous layer. By contrast, 30-min exposure (Figure 74) leads to minimal deposition without degradation of the outer layer.

Under cold conditions, there is a trade off between sealant loading and surface degradation. As a result cold nickel acetate sealing is not an equivalent replacement for hot nickel acetate, which fills the pores and covers the surface without degradation. These findings are supported by the corrosion performance experiments discussed in section 5.10.1, which show the superiority of hot nickel acetate.

6. Conclusions and Implications for Future Research and Implementation

This project demonstrates that most interfacial issues important to corrosion control can be elucidated by NR and XRR. So far we have not found any passive metal that cannot be deposited on silicon wafers if suitable buffer layers are used. In addition, TCP work shows that conversion coatings can be deposited and tracked during deposition and failure. Finally, aggressive anodizing conditions produce anodic films that show beautiful reflectivity profiles.

The data produced give corrosion scientists their first glimpse at active corrosion processes. The evolution of a surface can now be measured in near real time. Moreover failure on highly passive metals can be accelerated by application of an anodic potential.

6.1 Conclusions regarding substrate preparation

Metal substrates (Cu, Al and Al-Cu alloy) suitable for NR/XRR technology can be prepared by e-beam evaporation. The optimum metal substrate thickness is ~1000 Å, although successful experiments were carried out with films between 200 and 3500 Å. A number of factors determine the optimum thickness including instrument resolution, required smoothness and the aggressiveness of the corrosive environment.

Substrates can also be prepared by annealing of layers Al-Cu films. Vacuum annealing (300 ˚C for 15 hours followed by 450 ˚C for 5 min) transforms the layered pure Al and pure Cu of proper thickness ratio into a uniform Al-Cu alloy with tunable microstructure. This possibility, however, was not pursued in the current project.

6.2 Conclusions regarding vanadate films

Vanadate films on AA2024 optimized for NR measurement were achieved with 30-s exposure to 1/10 diluted vanadate precursor solution. The top part of the AA2024 substrate anticipates film formation by dissolving into the precursor solution and locally raising up the pH at the metal substrate surface. $K_3Fe(CN)_6$ plays an important role in the formation of the vanadate film as an accelerator for the Al^0/Al^{3+} redox couple.

The typical thickness of vanadate film on AA2024 under the experimental conditions is 800 - 1000 Å. A layered film structure is observed. The bottom thin (< 100 Å) layer at the metal-inhibitor film interface is more hydrophobic than the bulk film, which plays a critical role in corrosion protection.

The vanadate film is a water barrier. Although the water wets the air-side surface and penetrates the top bulk film, the hydrophobic vanadium-rich interface layer remains untouched. The bulk film is less hydrophobic (5-vol% water content). The water also swells the bulk film leading to a 9% thickness increase.

Vanadium is enriched at the metal-coating interface while the bulk layer contains other elements. If the VCC film contains only vanadium and oxygen, the calculated atomic formulas for bottom and bulk top layers are V_2O_5 and V_2O_{12}, respectively. The corresponding densities are (1.5 ± 0.02) g/cm^3 and (1.84 ± 0.02) g/cm^3, respectively.

The formation mechanism of vanadate film is proposed as a four-stage process. The dissolution of metal increases the pH at the metal-precursor interface, which triggers the precipitation of vanadium species. The resulting gel retards subsequent deposition, resulting a layered structure. When the film dries the film fully dehydrates and forms an insoluble protective film.

The capability of probing a buried inhibitor films was demonstrated by non-destructive determination of vanadate film structure under epoxy top coating. No inhibitor layer grows under and uncompromised epoxy top coat even though the inhibitor solution is known to penetrate the epoxy layer.

6.3 Conclusions regarding TCP films

The structure of TCP deposition films depends on how the films are deposited. Immersion films are different from electro-assisted films in that the latter grow linearly with cathodic polarization time after a thin dense layer forms at the metal interface. In the immersion experiment, proton consumption is driven by the metal dissolution. The film itself, however, inevitably restricts metal dissolution. Metal-ion diffusion though the film becomes increasingly difficult as the film grows. Thus dissolution is retarded and proton consumption is replenished by ions from the bulk solution. The pH gradient decreases, leading to a Zr-rich surface, which is rough and defective.

Electro-assisted deposition produces a denser, thicker TCP film compared to immersion. The dense interfacial layer between the metal and the bulk TCP deposition film is extremely thin due to rapid deposition in the initial state. Consumption of hydrogen ions is controlled by the applied potential, leading to diffusion-controlled, steady-state growth after the interfacial layer forms. Film thickness then depends on the time under cathodic polarization. The composition of the film is $Cr_2O_3 \cdot i H_2O \cdot x(ZrO_2 \cdot jH_2O)$ (i =2.10 ± 0.55, j = 1.60 ± 0.45 and x = 0.85 ± 0.14) as determined by comparing the SLD before and after driving off the water of hydration by vacuum baking, and by comparing the neutron and x-ray SLDs. SIMS data from the EA TCP deposition film confirm co-deposition of Cr and Zr compounds.

These experiments represent the first measurements on the structure and composition TCP films. The new data provide the opportunity to learn how TCP films form and what the optimum structure is for corrosion protection. At this point it is not clear which film is most protective. The immersion film is thin, less dense (lower SLD) and rich in Zr(IV). The EA films, on the other hand, have an extremely thin dense layer, and are overall thicker and denser. The EA film also has more Cr(III), which could affect corrosion protective properties. Further investigation of Cr(III) and Zr(IV) precipitation on a polarized substrate is needed to optimize the Zr/Cr ratio.

6.4 Conclusions regarding Ce(III) inhibition of TCP films

Step-by-step anodic polarization is shown to be a straightforward assessment tool to evaluate self-healing potential and determine the upper potential limit of Ce(III) inhibition on TCP films. The observed upper limit is for the alloy is -580 mV in aqueous solution ($4 < pH < 8$). According to the step-by-step current density profile Ce(III) inhibition takes time to activate, particularly near the upper potential limit.

The combined electrochemical and NR data reveal the structural and chemical information in TCP layer under both anodic and cathodic conditions. We draw the following conclusions:

Firstly, Ce(III) is identified in the TCP layer under anodic polarization. Ce(III) extends the passive potential range and reduces the passive current baseline. In other words, Ce(III) in the film "delays" the occurrence of pitting failure. NR data reveal significant Ce throughout the film, but more concentrated at the film/aqueous interface.

Assuming a stable TCP matrix with constant Cr and Zr content the estimated concentration ratio of Ce(III) in the film after anodic hardening is $\mathrm{Cr} : \mathrm{Zr} : \mathrm{Ce} = 2 : 0.85 \pm 0.14 : 1.2 \pm 0.4$. The concentration of Ce could be even higher if the calculation includes the partial conversion of the TCP matrix from Cr(III) to Ce(III).

The Ce(III)-enriched TCP layer implies that the anodically hardened TCP film could serve as a leaching reservoir for long term active healing. The ICP data imply a possible exchange between Cr and Ce during anodic hardening, leading to leaching of both ions over 20 days.

The *in situ* NR data on the TCP-passivated Al cathode show continuous film evolution over 24 h. Besides the increasing water content in the TCP bulk layer, a peak forms after 20-h polarization, implying a densified Al/TCP interface. The most likely explanation for new interface is precipitation of $Ce(OD)_3$. Building on the generally accepted mechanism for Ce(III) cathodic inhibition, the precipitation process starts after the TCP layer expands due to water imbibition. Ce(III) ions then pass through the loose structure and precipitate at the TCP/Al interface, where localized pH rises due to the proton reduction reaction. Comparing the SLD value before and after 24-hour polarization, molar concentration of $Ce(OD)_3$ at the peak is calculated to be between $1.5 \times 10^{-3}\mathrm{mol/cm^3}$ and $9.8 \times 10^{-3}\mathrm{mol/cm^3}$.

The two-TCP-coated Al electrode configuration is not best suited for observation of *in situ* cathodic Ce(III) inhibition. For future work on *in situ* Ce(III) cathodic inhibition, it would be ideal to polarize a TCP-passivated Al cathode cathodically vs. a Au-coated wafer anode and measure both NR and the cathodic current as the cathode passivates. It is also necessary to measure the exchange current by DC polarization at the end of the inhibition process to be sure the cathode has passivated.

6.5 Conclusions regarding AAO films

The interface morphology of the anodized aluminum oxide was determined by combined XRR and NR techniques. In order to prepare AAO on thin Al coatings, we developed a concurrent current-limited and voltage-controlled anodizing strategy. This method prevents the detachment of thin AAO films from Si substrate at the same time it achieves good control over the thickness and porosity of the AAO layer. USAXS measurements on Al foils complement XRR and NR, to reveal the relationship between porous structure and deposition voltage and solution electrolytes. The pore diameter, wall thickness and interpore distance all increase with voltage. These parameters also depend on the anodizing media with the smallest pores in sulfuric acid and the largest in phosphoric acid.

USAXS results implies that hot nickel acetate sealing differs from cold sealing and hot water sealing in that the latter do not show significant structural change on 30 min exposure to the sealing bath. On the other hand, hot nickel acetate sealing fills the pores completely and deposits on the air surface as well.

Long-term exposure to cold nickel acetate leads to densification of the AAO at the metal interface, but also degradation of the AAO at the air interface. Cold nickel acetate fills only the

bottom of the pores at interface with metal substrate, as shown by our *ex situ* NR and XRR, and *in situ* NR results. The mechanism of cold nickel acetate sealing is different from hot nickel acetate, which fills the pores and deposits a layer of nickel acetate on top of the AAO film. Therefore, the hot nickel acetate yields the best corrosion performance compared to other sealing methods.

6.6 Conclusions in the context of the project goals

Goal 1: Identify the film deposition parameters that are optimal for NR and XRR measurement.

Using electro-assisted deposition we achieved optimum conversion coatings using a simplified TCP formulation. Films grow linearly with deposition time.

Aluminum anodizing was successfully achieved on an Al-coated silicon wafer suitable for both XRR and NR. XRR was used to identify the optimum conditions for oxide film growth.

Goal 2: Develop a method to correlate measured morphology with electrochemical observations.

An *in situ* split liquid cell was built that is suitable to observe the evolution of both the anode and cathode of an electrochemical couple in an active corrosion environment under potential control. For both Ce inhibition and anodization, the electrochemical properties were correlated with morphological evolution of the films.

Goal 3: Monitor the in situ evolution of TCP films under electrochemical potential control, with and without additional inhibitors

The split cell was successfully used to monitor the evolution of TCP-coated aluminum on Al in 1% NaCl solution. Below the pitting potential the films show no change over a 24 h period. Step-by-step anodic polarization of TCP in the presence of Ce(III) leads to a dramatic decrease of the corrosion current and 50 mV increase of the pitting potential. During the post deposition hardening process Ce deposits in the TCP film.

Goal 4: Identify the mechanism of inhibition using *in situ* neutron reflectivity.

In the presence of Ce(III), both the anodic and cathodic surfaces undergo considerable evolution. Under anodic polarization $Ce(OD)_3$ (or some other Ce rich compound) deposits in the pores of the native TCP film with no change in film thickness. $Ce(OD)_3$ preferentially forms at the film-solution interface. On cathodic surfaces, deposition occurs within the film initially, but eventually the film thickens and forms of a dense layer at the metal-film interface. The deposited inhibitor serves a reservoir that enhances long-term protection. Quantitative analysis of the NR data shows that the amount of Ce in the film is comparable to the amounts of Cr and Zr.

Goal 5: *Investigate the formation and sealing of anodizing films on aluminum*.

We developed a concurrent current and voltage control that can control both the thickness and porosity of the thin oxide films (< 4000 Å). Anodization of Al, using either the new strategy or conventional voltage control, produces two layers of AAO (dense AAO and porous AAO). Both layers have densities lower than that of fully dense crystalline Al_2O_3. The kinetics study shows that anodizing process stabilizes fast in the beginning of anodizing (within 20 s). After the induction stage, the pore size, wall thickness, and inter-pore distance remain constant, and only the pore length grows in the direction normal to the surface.

Hot sealing methods enhance the protective properties of anodizing AAO more than cold methods. Hot nickel acetate, in particular, fills the pores and deposits on the surface. Cold nickel acetate sealing, by contrast, leads to deposition at the bottom of the pores and in the barrier layer. After long exposure to the cold bath, however, the top layer sloughs off on drying. Shorter exposures leave the AAO intact, but deposition in the pores is small, leading to minimal enhancement of corrosion protection. Electrochemical data confirm the superiority of hot sealing methods.

6.7 Implications for follow-on research

Although this project demonstrated the value of reflectivity methods, we only scratched the surface as far as elucidating corrosion mechanisms. For this demonstration project, we confined ourselves to current technology. We elucidated native passive film, anodic films, TCP conversion coatings and Ce inhibited coatings. Although all the information garnered is both unique and important to understanding protection mechanisms, we did not compare effective and ineffective systems to determine the morphological basis of corrosion protection.

Process-structure-performance data are needed to advance corrosion science. The structure leg of this research strategy has been missing since the inception of corrosion research because there was no method to measure structure evolution in a corrosive environment. This project adds this vital new capability to the corrosion-science toolbox. Application of these methods applies to virtually every aspect of corrosion science and technology. Specific problems that can be addressed include:

1. *Nature of effective films:* The methods developed here should be used to determine the difference in structure between effective films and ineffective films. In some cases small changes in the bath composition hace a dramatic effect on protection. If the structural basis of effective protection were known, rational design of benign protection emerges as a credible alternative to the parametric approach to inhibitor development.
2. *Evaluation of other inhibitors:* We have only explored Ce(III) as a soluble inhibitor. Other inhibitor systems should be examined.
3. *Application to other metals*: We explored only Al surfaces. Other important metals such as ferrous alloys should be examined. Ferrous alloys can be deposited using magnetron sputtering. We have achieved excellent 1000-Å iron films.
4. *Stainless steel:* Iron is very resistant to formation of anodic films. Addition of Al or other elements can lead to improved native oxides. We need to understand native and anodic films on iron and stainless alloys with the goal of reducing Cr in stainless steel.
5. *Anodic hardening:* The anodic hardening method should be developed into a technology. Is it possible to achieve anodic hardening without imposition of a potential, such as by long-term immersion, or immersion in a medium with a high mixed potential. Can the mixed potential be raised chemically rather than electrochemically? Are other rare earths more effective than Ce(III)?
6. *Tetravalent cation conversion coatings:* In addition to Cr(III) effective conversion coatings are known based on tetravalent metals such as Zr, Hf, Ti, and Si. The advantage of Zr systems is that they work on cold-rolled steel (CRS) in addition to Zn and Al. The nature of these films is unknown. Since these elements cannot be used as soluble salts, they are used as hexafluoro acids such as H_2ZrF_6.[61] H_2ZrF_6 undergoes the following hydrolysis reactions:

$$H_2ZrF_6 \Leftrightarrow ZrF_4 + HF$$

$$ZrF_4 + 2H_2O \Leftrightarrow ZrO_2 + 4HF$$

These reactions show that H_2ZrF_6 exists only at low pH and will form ZrO_2 when the pH is raised. Thus the composition of the conversion coating presumably is a mixture of ZrO_2 and the hydroxide of the base metal. Unfortunately, the flurozirconate process is not robust; the treatment bath is sensitive to contamination, line stoppage, and requires thorough metal cleaning.[62, 63]

5. *Role or Cr and Zr in TCP coatings.* Noting that Zr is the likely protective element in TCP films, it seems that the role of Cr(III) is to mitigate problems with pure H_2ZrF_6 baths, which motivates the need to elucidate the role of Zr/Cr ratio in TCP films.
6. *Zr on bare metals:* Although Zr-based metal pretreatments are now the most widely used replacements for chromates and phosphates for painted surfaces, they are not effective on bare metals. As a result, Zr-based pretreatments have not penetrated the unpainted metals market such aerospace and the architecture. Reflectivity in should be used to explore the reason for failure on bare metals.
7. *Energy efficient anodizing:* Al anodizing is a very energy inefficient process. The new current controlled-voltage limited anodizing method should be explored as a way to achieve effective films with lower energy input.
8. *New sealing strategies:* Our results reveal the structure of effective sealants for anodic films. This capability should be exploited to develop more effective sealants.
9. *Mg Anodizing:* The new current controlled-voltage limited anodizing method offers new possibilities of achieving effective corrosion protection on Mg. The density of Mg is 40% less than Al. If the corrosion issue can be addressed, dramatic weight reductions are possible.
10. *Ionic liquid media:* We have only explored passivation and inhibition in aqueous media. Ionic liquids offer a much larger stability window to carry out electrodeposition and anodization. Reflectivity is an ideal method to examine the formation and failure of protective films. New contrast enhancement strategies emerge that will facilitate examination of very thin protective films.
11. *Accelerated aging:* Reflectivity under potential control can be developed as an accelerated aging method that not only measures the lifetime of protective films, but the mechanism of failure.
12. *Interface evolution under cathodic conditions:* We have concentrated on anodic inhibition. The nature of cathodic passivation on Cu and intermetallics need to be pursued.

7. Literature Cited

1. J.J. Noel, D.W. Shoesmith and Z. Tun, *Anodic Oxide Growth and Hydrogen Absorption on Zr in Neutral Aqueous Solution: A Comparison to Ti.* Journal of the Electrochemical Society, 2008. **155**(8), p. C444-C454.
2. Z. Tun, J.J. Noel and D.W. Shoesmith, *Anodic oxide growth on Zr in neutral aqueous solution.* Pramana-Journal of Physics, 2008. **71**(4), p. 769-776.
3. Z. Tun, J.J. Noel and D.W. Shoesmith, *Electrochemical Modification of the Passive Oxide Layer on a Ti Film Observed by In Situ Neutron Reflectometry.* Journal of the Electrochemical Society, 1999. **146**(3), p. 988-994.
4. Z. Tun, J.J. Noël and D.W. Shoesmith, *Electrochemical modifications on the surface of a Ti film.* Physica B: Condensed Matter, 1997. **241-243**(0), p. 1107-1109.
5. D.G. Wiesler, M. Toney, C. McMillan and W. Smyrl, *Interfacial Density Profiles of Anodic Oxides of Tantalum And Niobium Measured by X-Ray Reflectivity.* The Application of Surface Analysis Methods to Environmental Materials Interactions, 1991, p. 440.
6. W. Kern, *Handbook of semiconductor wafer cleaning technology science, technology, and applications*. Materials science and process technology series Electronic materials and process technology. 1993, Park Ridge, New Jersey: Noyes Publications.
7. J. Ilavsky and P.R. Jemian, *Irena: tool suite for modeling and analysis of small-angle scattering.* Journal of Applied Crystallography, 2009. **42**, p. 347-353.
8. A. Guinier and G. Fournet, *Small-Angle Scattering of X-rays*. 1955, New York: John Wiley and Sons.
9. P. Debye, R. Anderson and H. Brumberger, *Scattering by an Inhomogeneous Solid. II. The Correlation Function and Its Application.* Journal of Applied Physics, 1957. **28**(6), p. 679.
10. A.M. Fernandez, G.D. Wignall and L.H. Sperling, *Multicomponent Polymer Materials* in *Advances in Chemistry Series* D.R. Paul and L.H. Sperling, Editors. 1986, American Chemical Society: Washington, DC. p. 153-70.
11. J.E. Martin and A.J. Hurd, *Scattering from Fractals.* Journal of Applied Crystallography, 1987. **20**, p. 61-78.
12. D.W. Schaefer, B.C. Bunker and J.P. Wilcoxon, *Fractals and Phase-Separation.* Proceedings of the Royal Society of London Series a-Mathematical Physical and Engineering Sciences, 1989. **423**(1864), p. 35-53.
13. G. Porod, *Die Röntgenkleinwinkelstreuung von dichtgepackten kolloiden Systemen.* Colloid & Polymer Science, 1951. **124**(2), p. 83-114.
14. K.D. Keefer and D.W. Schaefer, *Growth of Fractally Rough Colloids.* Physical Review Letters, 1986. **56**(22), p. 2376-2379.
15. H. Guan and R. Buchheit, *Corrosion protection of aluminum alloy 2024-T3 by vanadate conversion coatings.* Corrosion, 2004. **60**(3), p. 284-296.
16. S. Dalbin, G. Maurin, R.P. Nogueira, J. Persello and N. Pommier, *Silica-based coating for corrosion protection of electrogalvanized steel.* Surface & Coatings Technology, 2005. **194**(2-3), p. 363-371.
17. A.A.O. Magalhaes, I.C.P. Margarit and O.R. Mattos, *Molybdate conversion coatings on zinc surfaces.* Journal of Electroanalytical Chemistry, 2004. **572**(2), p. 433-440.
18. B.R.W. Hinton and L. Wilson, *The Corrosion Inhibition of Zinc with Cerous Chloride.* Corrosion Science, 1989. **29**(8), p. 967-&.

19. B.R.W. Hinton, *Corrosion Inhibition with Rare-Earth-Metal Salts.* Journal of Alloys and Compounds, 1992. **180**, p. 15-25.
20. R.G. Buchheit, S.B. Mamidipally, P. Schmutz and H. Guan, *Active corrosion protection in Ce-modified hydrotalcite conversion coatings.* Corrosion, 2002. **58**(1), p. 3-14.
21. X.C. Dong, S. Argekar, P. Wang and D.W. Schaefer, *In situ Evolution of Trivalent Chromium Process Passive Film on Al in a Corrosive Aqueous Environment.* ACS Applied Materials & Interfaces, 2011. **3**(11), p. 4206-4214.
22. Y. Wang, P. Wang, D. Kohls, W.A. Hamilton and D.W. Schaefer, *Water absorption and transport in bis-silane films.* Physical Chemistry Chemical Physics, 2009. **11**(1), p. 161 - 166.
23. Y. Wang, E. Watkins, J. Ilavsky, T.L. Metroke, P. Wang, B. Lee, and D.W. Schaefer, *Water-Barrier Properties of Mixed Bis-[trimethoxysilypropyl]amine and Vinyl Triacetoxysilane Films* Journal of Physical Chemistry, B, 2007. **111**, p. 7041-7051.
24. W. Zhang, B. Hurley and R. Buchheit, *Characterization of chromate conversion coating formation and breakdown using electrode arrays.* J Electrochem Soc, 2002. **149**(8), p. B357-B365.
25. N.T. Wen, F.J. Chen, M.D. Ger, Y.N. Pan and C.S. Lin, *Microstructure of trivalent chromium conversion coating on electrogalvanized steel plate.* Electrochemical and Solid State Letters, 2008. **11**(8), p. C47-C50.
26. P. Campestrini, E.P.M. van Westing and J.H.W. de Wit, *Influence of surface preparation on performance of chromate conversion coatings on Alclad 2024 aluminium alloy Part I: Nucleation and growth.* Electrochimica Acta, 2001. **46**(16), p. 2553-2571.
27. P. Campestrini, E.P.M. van Westing, A. Hovestad and J.H.W. de Wit, *Investigation of the chromate conversion coating on Alclad 2024 aluminium alloy: effect of the pH of the chromate bath.* Electrochimica Acta, 2002. **47**(7), p. 1097-1113.
28. A.E. Hughes, R.J. Taylor and B.R.W. Hinton, *Chromate conversion coatings on 2024 Al alloy.* Surface and Interface Analysis, 1997. **25**(4), p. 223-234.
29. A. Kolics, A.S. Besing and A. Wieckowski, *Interaction of chromate ions with surface intermetallics on aluminum alloy 2024-T3 in NaCl solutions.* Journal of the Electrochemical Society, 2001. **148**(8), p. B322-B331.
30. W.J. Clark, J.D. Ramsey, R.L. McCreery and G.S. Frankel, *A galvanic corrosion approach to investigating chromate effects on aluminum alloy 2024-T3.* Journal of the Electrochemical Society, 2002. **149**(5), p. B179-B185.
31. M.W. Kendig and R.G. Buchheit, *Corrosion inhibition of aluminum and aluminum alloys by soluble chromates, chromate coatings, and chromate-free coatings.* Corrosion, 2003. **59**(5), p. 379-400.
32. M.J. Vasquez, G.P. Halada, C.R. Clayton and J.P. Longtin, *On the nature of the chromate conversion coating formed on intermetallic constituents of AA2024-T3.* Surface and Interface Analysis, 2002. **33**(7), p. 607-616.
33. L. Xia and R.L. McCreery, *Structure and function of ferricyanide in the formation of chromate conversion coatings on aluminum aircraft alloy.* Journal of the Electrochemical Society, 1999. **146**(10), p. 3696-3701.
34. Y. Liu, A.M. Arenas, S.G. Garcia-Vergara, P. Skeldon, G.E. Thompson, K. Shimizu, and H. Habazaki, *Ageing effects in the growth of chromate conversion coatings on aluminium.* Corrosion Science, 2005. **47**(1), p. 145-150.

35. L. Niu and Y.F. Cheng, *Electrochemical characterization of metastable pitting of 3003 aluminum alloy in ethylene glycol-water solution.* Journal of Materials Science, 2007. **42**(20), p. 8613-8617.
36. S. Hoerle, B. Malki and B. Baroux, *Corrosion current fluctuations at metastable to stable pitting transition of aluminum.* Journal of the Electrochemical Society, 2006. **153**(12), p. B527-B532.
37. O. Lensch, B. Enders, J. Knecht and W. Ensinger, *Examination of the metastable and stable pitting corrosion of aluminum modified with carbon by ion beam techniques.* Nuclear Instruments & Methods in Physics Research Section B-Beam Interactions with Materials and Atoms, 2001. **175**, p. 683-687.
38. B.W. Davis, P.J. Moran and P.M. Natishan, *Metastable pitting behavior of aluminum single crystals.* Corrosion Science, 2000. **42**(12), p. 2187-2192.
39. B.W. Davis, P.J. Moran and P.M. Natishan, *Metastable pitting behavior of single crystal surfaces of pure aluminum.* Proceedings of the Symposium on Critical Factors in Localized Corrosion Iii, 1999. **98**(17), p. 215-222.
40. F. Sato and R.C. Newman, *Mechanism of activation of aluminum by low melting point elements: Part 1 - Effect of zinc on activation of aluminum in metastable pitting.* Corrosion, 1998. **54**(12), p. 955-963.
41. S.T. Pride, J.R. Scully and J.L. Hudson, *Metastable Pitting of Aluminum and Criteria for the Transition to Stable Pit Growth.* Journal of the Electrochemical Society, 1994. **141**(11), p. 3028-3040.
42. J.R. Scully, *Metastable Pitting Corrosion of Aluminum, Al-Cu, and Al-Si Thin-Films in Dilute Hf Solutions and Its Relevancy to the Processing of Integrated-Circuit Interconnections.* Materials Reliability Issues in Microelectronics, 1991. **225**, p. 343-348.
43. X. Dong, P. Wang, S. Argekar and D.W. Schaefer, *Structure and Composition of Trivalent Chromium Process (TCP) Films on Al Alloy.* Langmuir, 2010. **26**(13), p. 10833-10841.
44. K.D. Ralston, S. Chrisanti, T.L. Young and R.G. Buchheit, *Corrosion Inhibition of Aluminum Alloy 2024-T3 by Aqueous Vanadium Species.* Journal of the Electrochemical Society, 2008. **155**(7), p. C350-C359.
45. K.A. Yasakau, M.L. Zheludkevich, S.V. Lamaka and M.G.S. Ferreira, *Mechanism of Corrosion Inhibition of AA2024 by Rare-Earth Compounds.* Journal of Physical Chemistry B, 2006. **110**(11), p. 5515-5528.
46. V. Palanivel, Y. Huang and W.J. Ooij, *Effects of addition of corrosion inhibitors to silane films on the performance of AA2024-T3 in a 0.5M NaCl solution.* Progress in Organic Coatings, 2005. **53**(2), p. 153-168.
47. A.J. Aldykiewicz, H.S. Isaacs and A.J. Davenport, *The Investigation of Cerium as a Cathodic Inhibitor for Aluminum-Copper Alloys.* Journal of the Electrochemical Society, 1995. **142**(10), p. 3342-3350.
48. A.J. Davenport, H.S. Isaacs and M.W. Kendig, *Xanes Investigation of the Role of Cerium Compounds as Corrosion-Inhibitors for Aluminum.* Corrosion Science, 1991. **32**(5-6), p. 653-663.
49. X. Zhang, C. van den Bos, W.G. Sloof, A. Hovestad, H. Terryn, and J.H.W. de Wit, *Comparison of the morphology and corrosion performance of Cr(VI)- and Cr(III)-based conversion coatings on zinc.* Surface & Coatings Technology, 2005. **199**(1), p. 92-104.
50. M. Dabala, L. Armelao, A. Buchberger and I. Calliari, *Cerium-based conversion layers on aluminum alloys.* Applied Surface Science, 2001. **172**(3-4), p. 312-322.

51. A.J. Davenport, H.S. Isaacs and M.W. Kendig, *X-Ray Absorption Study of Cerium in the Passive Film on Aluminum.* Journal of the Electrochemical Society, 1989. **136**(6), p. 1837-1838.
52. M. Kendig and S. Jeanjaquet, *Cr(VI) and Ce(III) inhibition of oxygen reduction on copper.* Journal of the Electrochemical Society, 2002. **149**(2), p. B47-B51.
53. W.G. Fahrenholtz, M.J. O'Keefe, H.F. Zhou and J.T. Grant, *Characterization of cerium-based conversion coatings for corrosion protection of aluminum alloys.* Surface & Coatings Technology, 2002. **155**(2-3), p. 208-213.
54. D. Crouse, Y.H. Lo, A.E. Miller and M. Crouse, *Self-ordered pore structure of anodized aluminum on silicon and pattern transfer.* Applied Physics Letters, 2000. **76**(1), p. 49-51.
55. F.Y. Li, L. Zhang and R.M. Metzger, *On the growth of highly ordered pores in anodized aluminum oxide.* Chemistry of Materials, 1998. **10**(9), p. 2470-2480.
56. G. Beaucage, T.A. Ulibarri, E.P. Black and D.W. Schaefer, *Multiple Size Scale Structures in Silica-Siloxane Composites Studied by Small-Angle Scattering* in *Hybrid Organic-Inorganic Composites*, J.E. Mark, C.Y.-C. Lee, and P.A. Bianconi, Editors. 1995, American Chemical Society: Washington, DC. p. 97-111.
57. N. Hu, N. Borkar, K. Doug; and D.W. Schaefer, *Characterization of Porous Materials Using Combined Small-angle X-ray and Neutron Scattering Techniques.* Journal of Membrane Science, 2011. **379**(1-2), p. 138-145.
58. T.P. Hoar and G.C. Wood, *The sealing of porous anodic oxide films on aluminium.* Electrochimica Acta, 1962. **7**(3), p. 333-353.
59. H. Herrera-Hernandez, J.R. Vargas-Garcia, J.M. Hallen-Lopez and F. Mansfeld, *Evaluation of different sealing methods for anodized aluminum-silicon carbide (Al/SiC) composites using EIS and SEM techniques.* Materials and Corrosion-Werkstoffe Und Korrosion, 2007. **58**(11), p. 825-832.
60. F. Mansfeld and M.W. Kendig, *Evaluation of Anodized Aluminum Surfaces with Electrochemical Impedance Spectroscopy.* Journal of the Electrochemical Society, 1988. **135**(4), p. 828-833.
61. S. Adhikari, K.A. Unocic, Y. Zhai, G.S. Frankel, J. Zimmerman, and W. Fristad, *Hexafluorozirconic acid based surface pretreatments: Characterization and performance assessment.* Electrochim Acta, 2011. **56**(4), p. 1912-1924.
62. T. Kolberg, M. Walter and P. Schubach, *Method for Coating Metallic Surfaces with an Aqueous Multicomponent Composition*, 2008, US Patent Application Application US2008/0127859 A1.
63. R. Moore, *Coating Solution for Metal Surfaces*, 2009, US Patent Application Application US2009/0114118 A1.

Appendices

Appendix 1: Publications

1. X. Dong, S. Argekar, P. Wang and D.W. Schaefer, *In Situ Evolution of Trivalent Chromium Process Passive Film on Al in a Corrosive Aqueous Environment*. ACS Applied Materials and Interfaces, 2011. 3(11), p. 4206–4214.
2. N.P. Hu, N. Borkar, D. Kohls and D.W. Schaefer, *Characterization of porous materials using combined small-angle X-ray and neutron scattering techniques*. Journal of Membrane Science, 2011. 379(1-2), p. 138-145.
3. P. Wang, X. Dong and D.W. Schaefer, *Structure and water-barrier properties of vanadate-based corrosion inhibitor films*. Corrosion Science 2010. 52(3), p. 943-949.
4. X. Dong, P. Wang, S. Argekar and D.W. Schaefer, *Structure and composition of trivalent chromium inhibitor films on Al alloy*. Langmuir, 2010. 26(13), p. 10833–10841.

Appendix 2: Planned Publications

1. Naiping Hu, Xuecheng Dong, Sandip Argekar and Dale W. Schaefer, *Interface Morphology of Anodized Aluminum by X-ray Reflectivity*, ACS Applied Materials and Interfaces, draft.
2. Naiping Hu, Xueying He, Yan Zhang, Jan Ilavsky, Dale W. Schaefer, *Characterization of the structure of anodized aluminum oxide (AAO) by USAXS and SANS*, J. Applied Crystallography, Planned.
3. Naiping Hu, Xuecheng Dong, Dale W Schaefer, *The mechanism of cold nickel acetate sealing on anodized aluminum by XR, in situ NR, and USAXS*, Corrosion Science, Planned.
4. Xuecheng Dong and Dale W. Schaefer, *Anodic hardening*, Corrosion Science, Draft
5. Xuecheng Dong, Sandip Argekar and Dale W. Schaefer, *Evolution of anodically hardened TCP films in a corrosive environment*. Langmuir, Draft.

Appendix 3: Presentations

1. X. Dong, N. Hu and D.W. Schaefer, *Interface Structure of Passive Films on Al by X-ray and Neutron Reflectivity* presented by X. Dong at Partners in Environmental Technology Technical Symposium & Workshop, Washington, DC, Nov. 29 - Dec. 1, 2011, (Poster).
2. X. Dong and D.W. Schaefer, *Recovery of TCP passivity in the presence of inhibitors*, presented by X. Dong at Partners in Environmental Technology Technical Symposium & Workshop, Washington, DC, Nov. 30 - Dec. 2, 2010, (Poster).
3. X. Dong and D.W. Schaefer, *In Situ Evolution of Non-Chromate Inhibitor Films by Simultaneous Neutron Reflectivity and Electrochemical Methods*, presented by X. Dong at The Ohio Innovation Summit OIS 10 Materials and Energy: The Building Blocks for Ohio's Economic Future Columbus, April 20-21, 2010, (Poster).
4. D.W. Schaefer and X. Dong, *Trivalent Chromium Process Conversion Coatings: A New Look at a New Problem*, presented by D.W. Schaefer at Materials Science & Technology 2010 Conference Advanced Coatings and Surface Treatments for Corrosion Protection Symposium, Houston, TX, October 17-21, 2010, (Invited).
5. X. Dong and D.W. Schaefer, *In Situ Evolution of Non-Chromate Inhibitor Films by Simultaneous Neutron Reflectivity and Electrochemical Methods*, presented by X. Dong at 8th Spring Meeting of the International Society of Electrochemistry Columbus, OH, May 2 - 5, 2010, (Contributed).
6. P. Wang, X. Dong and Dale W. Schaefer, *Structure and Composition of Non-Chromate Conversion Coatings*, presented by D.W. Schaefer at Partners in Environmental Technology Symposium, Washington DC, December 1 - 3, 2009, (Poster).
7. D.W. Schaefer and P. Wang, *Structure of chromate-free metal protective films from neutron reflectivity*, presented by D.W. Schaefer at NACE Corrosion 2009, Atlanta, March 22-29, 2009, (Invited).
8. D.W. Schaefer, *Structure of Non-Chromate Metal-Protective Films: Evidence from Neutron and X-ray Reflectivity.*, presented by D.W. Schaefer at Electrical and Computer Engineering department seminar, Cincinnati, May 15, 2009, (Invited).
9. X. Dong and D.W. Schaefer, *Structure of Cr(III) Corrosion-Inhibitor Film on Al 2024 by Neutron Reflectivity*, presented by D.W. Schaefer at Ninth LANSCE User Group Meeting, Santa Fe, Sept. 29-30, 2009, (Poster).
10. P. Wang and D.W. Schaefer, *Can Vanadates Replace Chromates?*, presented by P. Wang at Partners in Environmental Technology Technical Symposium & Workshop, Washington, DC, December 2-4, 2008, (Poster).
11. P. Wang, D. W. Schaefer, X. Dong, J. Carey, D. Hickmott, J. Baldwin, J. Majewski, and J. Browning, *The Nature of Passive Films on Stainless Steel.* American Conference on Neutron Scattering 2012, June 24-28, 2012.